



저작자표시-비영리-변경금지 2.0 대한민국

이용자는 아래의 조건을 따르는 경우에 한하여 자유롭게

- 이 저작물을 복제, 배포, 전송, 전시, 공연 및 방송할 수 있습니다.

다음과 같은 조건을 따라야 합니다:



저작자표시. 귀하는 원저작자를 표시하여야 합니다.



비영리. 귀하는 이 저작물을 영리 목적으로 이용할 수 없습니다.



변경금지. 귀하는 이 저작물을 개작, 변형 또는 가공할 수 없습니다.

- 귀하는, 이 저작물의 재이용이나 배포의 경우, 이 저작물에 적용된 이용허락조건을 명확하게 나타내어야 합니다.
- 저작권자로부터 별도의 허가를 받으면 이러한 조건들은 적용되지 않습니다.

저작권법에 따른 이용자의 권리는 위의 내용에 의하여 영향을 받지 않습니다.

이것은 [이용허락규약\(Legal Code\)](#)을 이해하기 쉽게 요약한 것입니다.

[Disclaimer](#)

공학박사학위논문

Study on the stiffness control method of
DNA origami nanostructures

DNA 오리가미 나노구조물의 강성설계기술 연구

2019년 8월

서울대학교 대학원

기계항공공학부

이 찬 석

Abstract

In this thesis, we describe a rational design method that effectively controls the mechanical stiffness of DNA origami nanostructures. DNA origami has been attracted much attention since it has enabled programmed self-assembly of complex three-dimensional nanostructures by designing the sequence combinations of constituting DNA strands. With the proper shape design rules, DNA origami nanostructures can provide a number of different shapes and structural stiffness variations with nanometer-scale precision, which are difficult to be produced by conventional nanomaterials and nanofabrication techniques. However, high synthesis cost and design complexity, and as well as the absence of efficient design method and robust prediction model to minimize the cost-intensive design process remain as major hurdles of DNA origami-related research and application. In this study, a module-based design method that can control the local mechanical stiffness of the DNA constructs was developed. By utilizing it, we demonstrated a polymorphic shape variation of DNA origami nanostructures with minimized DNA sequence modification. Also, we presented the precise stiffness variation of DNA bundle structures with remarkably high design efficiency by using individually engineered defects. Since the proposed design method is compatible with conventional shape design rules, we expect that our method can be utilized to functional DNA origami nanostructures in which the mechanical stiffness of them should be properly designed.

Keywords: DNA origami, DNA nanostructures, Module-based design, Stiffness control, Localized defect, Finite element analysis

Student Number: 2014-30342

Table of contents

Abstract	1
Table of contents	2
List of tables	3
List of figures	4
Chapter 1. Introduction	8
1.1. Research background	8
1.2. Controlling the stiffness of DNA origami nanostructures	13
1.3. Materials and methods	17
Chapter 2. Stiffness control by mechanical modules.....	19
2.1. Introduction	19
2.2. Design method	21
2.3. Experimental results.....	26
2.4. Computational shape prediction.....	42
2.5. Molecular dynamics simulation	49
2.6. Analysis on the applicable range of hinge stiffness	57
2.7. Conclusion	66
Chapter 3. Stiffness control by engineered defects.....	67
3.1. Introduction.....	67
3.2. Design method	69
3.3. Experimental results.....	74
3.4. Computational model and validation	99
3.5. Molecular dynamics simulation	118
3.6. Conclusion	125
Chapter 4. Concluding remark	126
Acknowledgments.....	127
Bibliography.....	128
국 문 초 록.....	137

List of tables

- Table 1-1.** Comparison of two modular design methods to control the stiffness of DNA origami nanostructures.
- Table 2-1.** Reference staple set.
- Table 2-2.** The number of eliminated and replaced staples compared with the reference structure.
- Table 2-3.** Monomer folding yield of all structures calculated from gel electrophoresis in Fig. 2-7.
- Table 2-4.** Structural folding yield result of all 24 structures shown in Fig. 2-4.
- Table 2-5.** Detailed experimental data of measured included angles shown in Fig. 2-10.
- Table 3-1.** Summary of bending persistence length measurement.
- Table 3-2.** Structural folding yield result.
- Table 3-3.** Parameters used in FE modeling.

List of figures

- Figure 1-1.** Schematic illustration of scaffolded DNA origami and staple connectivity map.
- Figure 2-1.** Schematic illustration of the modular design.
- Figure 2-2.** The effect of hinge stiffness without an adjuster component.
- Figure 2-3.** AFM images showing the effect of the hinge with different length of dsDNA adjuster strands.
- Figure 2-4.** Demonstration of the 24 structural variations from the straight 12-helix honeycomb-latticed reference structure.
- Figure 2-5.** AFM images of the structures #1 to #12 shown in Fig. 2-4.
- Figure 2-6.** AFM images of the structures #13 to #24 shown in Fig. 2-4.
- Figure 2-7.** Agarose gel electrophoresis results showing the folding yield of the structures shown in Fig. 2-4.
- Figure 2-8.** Structural folding yield analysis using AFM images.
- Figure 2-9.** An exemplary method to circumvent local energy minima issue in the double-hinged structure with a long adjuster strand.
- Figure 2-10.** Broad and precise included angle variation of the hinge structure by controlling the length of the dsDNA adjuster strand.
- Figure 2-11.** Representative AFM images of the structures with the included angle variation from 0° to 150° shown in Fig. 2-10.
- Figure 2-12.** Agarose gel electrophoresis result of the designs shown in Fig. 2-10.
- Figure 2-13.** CanDo shape prediction of the structures #1 to #12 in Fig. 2-4.
- Figure 2-14.** CanDo shape prediction of the structures #13 to #24 in Fig. 2-4.
- Figure 2-15.** Examples of structural failure due to the geometrical distortion.
- Figure 2-16.** CanDo shape prediction of the structures shown in Fig. 2-10.
- Figure 2-17.** MD simulation of the ds0hb and ds2hb hinge module.
- Figure 2-18.** MD simulation of the ds3hb and no hinge module.

- Figure 2-19.** RMSD values of all designs throughout the MD simulation.
- Figure 2-20.** Base pairing ratio analysis from MD simulation.
- Figure 2-21.** Principal component analysis (PCA) from MD simulation.
- Figure 2-22.** Analysis of the hinge stiffness.
- Figure 2-23.** Large-area AFM images showing the relationship between hinge stiffness and monomer folding yield in Fig. 2-22.
- Figure 2-24.** Measured average included angles of three different hinge designs.
- Figure 2-25.** Representative CanDo results showing the strain energy concentration at the hinge region.
- Figure 2-26.** Included angle distribution of dsDNA adjuster structures having different adjuster strand length and hinge stiffness.
- Figure 2-27.** Included angle distribution of the ds0hb hinge structures having a different number of adjuster strut staples.
- Figure 3-1.** Schematic illustration of defect-engineering of DNA nanostructures.
- Figure 3-2.** 4HB gap design.
- Figure 3-3.** 6HB gap design.
- Figure 3-4.** Design parameters for defect-engineered DNA origami bundles and a computational model to predict their flexibility.
- Figure 3-5.** Calculation of persistence length from monomer contours.
- Figure 3-6.** Bending persistence length measurement with different unit segment length.
- Figure 3-7.** Parameter analysis on 4HB-Ref design.
- Figure 3-8.** Parameter analysis on 6HB-Ref design.
- Figure 3-9.** Calculation of bending persistence length while varying the range of contour length.
- Figure 3-10.** Calculation of bending persistence length while varying the resolution of the images.
- Figure 3-11.** Measured bending persistence lengths of the 4HB and 6HB structures designed with the systematically varied length and density of gaps.

Figure 3-12. Experimental characterization of 4HB with 1 and 3-nt gap variations.

Figure 3-13. Experimental characterization of 4HB with 5-nt gap variations.

Figure 3-14. Experimental characterization of 6HB with 1 and 2-nt gap variations.

Figure 3-15. Experimental characterization of 6HB with 3 and 4-nt gap variations.

Figure 3-16. Experimental characterization of 6HB with 5-nt gap variations.

Figure 3-17. Experimental characterization of 6HB with 5-nt anisotropically distributed gaps.

Figure 3-18. Gel electrophoresis result of 4HB designs.

Figure 3-19. Gel electrophoresis result of 6HB designs.

Figure 3-20. Structural folding yield analysis.

Figure 3-21. 6HB bundle with 42-nt-interval crossover modification at half of the region.

Figure 3-22. 6HB bundle with staple omission at half of the region.

Figure 3-23. Schematic illustration of the FE model.

Figure 3-24. FE modeling of defect-engineered structures.

Figure 3-25. Sensitivity analysis for the HJ-nick element.

Figure 3-26. Sensitivity analysis for the 5-nt-long ssDNA gap element.

Figure 3-27. Schematic illustration of various cross-section designs with full density of the engineered defects.

Figure 3-28. Application of the defect-engineering design method for stiffness control of bundles with various cross-sections.

Figure 3-29. Gap layout and estimated bending persistence length of (a) 4HB-hex and (b) 8HB-hex design.

Figure 3-30. Gap layout and estimated bending persistence length of (a) 8HB-sq and (b) 10HB-hex design.

Figure 3-31. Gap layout and estimated bending persistence length of (a) 12HB-hex and (b) 12HB-sq design.

- Figure 3-32.** Gap layout and estimated bending persistence length of (a) 13HB-hex and (b) 16HB-sq design.
- Figure 3-33.** Experimental results of 10HB with gap density variations for cross-validation with FE simulation.
- Figure 3-34.** Experimental characterization of 10HB with 5-nt gap variations.
- Figure 3-35.** Demonstration of the enhancement in structural yield for bent DNA bundles through defect-engineering.
- Figure 3-36.** DNA sequence used in MD simulation.
- Figure 3-37.** Schematic illustration of 6HB used in the MD simulation.
- Figure 3-38.** The time-average cross-sectional shape of five representative planes of 6HB structures with and without gaps.
- Figure 3-39.** Geometrical characteristics of cross-sections.
- Figure 3-40.** Comparison of bending stiffness results.

Chapter 1. Introduction

1.1. Research background

Deoxyribonucleic acid (DNA) is composed of four types of nucleotides and sugar phosphate backbone linking them, and is known as a carrier of genetic information of living organisms. Aside from its biological function, the capability of complementary base pairing between DNA sequences (adenine with thymine, and guanine with cytosine) opened the possibility of it to be used as a nanomaterial, when the sequences of two single-stranded DNA (ssDNA) strands were carefully designed. As a single base pair is about 0.34 nm in length and 2 nm in diameter, DNA is one of the most precisely controllable nanomaterials among others, such as inorganic nanotubes and nanowires, crosslinked polymer chains, and lithographically fabricated nanostructures. Also, it has been attracted due to its ability to conjugate with other biomaterials including peptides and proteins, and even other inorganic materials with the aid of functional groups¹.

Since the discovery of basic DNA junctions by Seeman in 1982², a number of researches have been performed for decades to engineer various DNA structural motifs and build DNA assemblies by using them, resulting in the rise of structural DNA nanotechnology field³. However, junction-based tile assembly has the limitation that assembled shapes were usually limited to 2D tiles, whose sizes were less predictable and controllable as well. The necessity of larger and more complex DNA nanostructures with controllable sizes led to the invention of scaffolded DNA origami reported by Rothemund in 2006⁴. It uses a long circular ssDNA derived from bacteriophage as a template (scaffold), and hundreds of synthetic oligonucleotides

(staples) with programmed sequences to fold the scaffold into desired geometries. Since the scaffold DNA origami provides remarkable diversity in shape design with improved folding yield, it has become the most widely employed technique in the fabrication of DNA nanostructures^{5,6}.

Typical DNA origami structures consist of a scaffold around 7249 to 8634 (M13 derived vectors) nucleotide (nt)-long, and up to 200 staple strands in which their lengths are within 20 to 50 nt. Each staple strand has complementary sequences to its binding sites on the scaffold, therefore a unique staple set for each target structure should be constructed. Synthesis of staple strands with custom sequences is commercially available with sufficient yield. In order to secure complete binding of all staple strands to the scaffold, an excessive amount of staples (e.g., ten times higher concentration than that of the scaffold) is typically used. In addition to the DNA strands, a reaction mixture usually contains the pH buffer such as Tris-Acetate-EDTA (TAE), and multivalent cation such as magnesium chloride to neutralize the negatively charged surface of double-stranded DNA (dsDNA)^{7,8}. Without sufficient cation concentration, dsDNA helices could not be closely packed with each other due to their electrostatic repulsion. Molecular self-assembly between DNA strands is initiated by the thermal annealing process. Traditional methods slowly cooled down the temperature of the reaction mixture up to a couple of days, but it was revealed that DNA origami structures could be assembled in more rapid cooling process or even isothermal condition up to few hours⁹. The overall self-assembly process of DNA origami is illustrated in Fig. 1-1.

The assembly of DNA helices into highly ordered 2D and 3D geometries is mediated by designing periodically arrayed inter-helix Holliday junctions (crossovers), whose positions can be determined by the intrinsic helicity of B-form

DNA (about 10.5 base pair/turn)¹⁰. Since each DNA origami structure requires a distinct set of staples with programmed lengths and sequences, a computational design program named as caDNAno was developed by Douglas et al.¹¹, to aid the shape and sequence design process. Recently, more advanced design tools providing algorithm-based automated scaffold routing and subsequent sequence design process have been demonstrated^{12,13}.

Although the synthesis cost of an oligonucleotide with custom sequence has been reduced consistently, preparation of hundreds of staple strands for the laboratory-scale production of DNA origami structures still remains at a high cost¹⁴. Therefore, the demand for a robust design validation tool has been increased since the complexity and diversity of shapes and functions of DNA origami structures have been increased¹⁵. There have been several attempts to use all-atom molecular dynamics (MD) simulation or coarse-grained simulations to capture the geometrical and mechanical characteristics of DNA origami structures¹⁶⁻¹⁹, but their computational cost were too high to be routinely used in DNA origami design. Therefore, a more simplified mechanical model based on finite element analysis (FEA) was developed by Kim et al.^{8,20}, to predict the equilibrated 3D shape and flexibility of DNA nanostructures within a few minutes. This approach is particularly useful when a DNA origami structure contains the regions with large deformations induced by mechanical perturbations, since it takes a very long simulation time in conventional methods and difficult to predict their effect experimentally as well.

After the self-assembly process, the quality assessment of assembled DNA origami nanostructures is usually performed by analyzing the intensity and sharpness of the target structure band from the result of agarose gel electrophoresis. But in order to analyze the structural characteristics of them individually, single-molecule

measurement techniques such as atomic force microscope (AFM), transmission electron microscope (TEM), and other fluorescent-based super-resolution imaging processes are required⁸. It can be noted that depending on the geometry of the structure to be measured, the proper imaging method should be selected since each method has its own advantages and limitations.

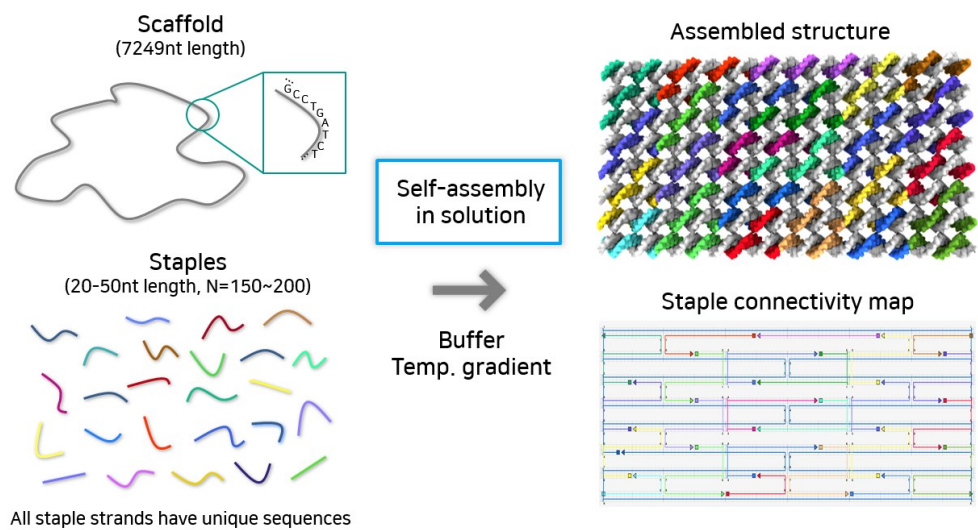


Figure 1-1. Schematic illustration of scaffolded DNA origami and staple connectivity map.

1.2. Controlling the stiffness of DNA origami nanostructures

Designing nanostructures with the desired geometry and controllable physical property is one of the fundamental demands in nanofabrication technology, and DNA origami has proven its potential to achieve that²¹. As described in Chapter 1-1, scaffolded DNA origami can provide the extensive shape design space in which it comes from the availability of drawing a unique scaffold pathway and corresponding sequence design of staple strands to immobilize the scaffold^{4,8,22}. The versatility of DNA origami in shape design to create almost any arbitrary geometry with nanometer-scale precision has been proved by a number of successful methods both with lattice-packed^{4,10} or lattice-free²³ assembly rules, as well as algorithmic inverse design procedures^{12,24} based on them.

In addition to the shape design, spatial controllability of mechanical stiffness of DNA origami opened a way to create dynamic and functional DNA nanostructures²⁵. Unlike other bulk nanomaterials, the availability of designing localized and site-directed flexible regions within a nanostructure is one of the major advantages of the DNA origami technology. By utilizing it, multiple applications were demonstrated such as single-molecule sensors^{26,27}, molecular substrates²⁸ and carriers²⁹, plasmonic structures^{30,31} and nanomechanical devices³²⁻³⁶. However, due to the lack of proper design motifs that effectively control the local mechanical stiffness without altering the geometric features or deteriorating the structural integrity, methods for controlling the mechanical stiffness of DNA nanostructures have rarely been advanced^{37,38}. Such limitation in DNA origami is mainly originated from the poor reusability of staple sequences, which has been considered as inevitable because even for a slight modification of its scaffold route can induce a

significant number of replacements due to the sequence shifting.

Design approaches so far have been used to control the local or global stiffness in DNA origami structures usually adopted changes in the cross-sectional geometry at the desired regions^{25,37,39}. Reducing the number of strands that passing through the desired sections has been frequently used to make flexible hinge-like mechanism^{36,39,40}. Though such modification is intuitive to design and generally works well, it resulted in the limitation of further design optimization such as shifting the locations or removing the existing deformable regions, or finely controlling the working range of them. Another reported method is to change the layout or connectivity of DNA helices^{41,42}. However, a significant amount of replacement in constituting staple set is still required in this method, since the modification of staple connectivity resulted in the change of DNA sequences.

In order to provide an effective stiffness control design method while minimizing the cost of staple replacement, we developed a module-based stiffness design approach in DNA origami⁴³. It should be noted that in order to control the mechanical stiffness of DNA origami structures with high staple reusability, the most important design principle is the conservation of the initially designed scaffold route. In our method, modification of the local structural stiffness is only mediated by revising the sequence of staple strands therein. Also, we utilized the computational prediction platform to validate the result of design modification prior to the experiment, which enables the significant reduction of time and cost during the design process.

In chapter 2, a rational module-based design approach is presented to create distinct bent shapes with controllable geometries and flexibilities from a single, reference set of staples⁴³. Each module consists of 10 to 11 staples and 14 nm long,

separated by scaffold crossovers. By revising the staple connectivity within the desired module, we can control the location, stiffness, and included angle of hinges precisely, enabling the construction of dozens of single- or multiple-hinge structures with the replacement of staple strands up to 12.8% only. Our design approach, combined with computational shape prediction and analysis, can provide a versatile and cost-effective procedure in the design of DNA origami shapes with stiffness-tunable units.

In chapter 3, a modular design method to precisely control the mechanical stiffness of DNA origami nanostructures without incurring any geometrical changes is demonstrated. It is enabled by introducing engineered mechanical defects, which consists of a short ssDNA segment consisting of one to five-nucleotides (nt) whose stiffness is considerably smaller than that of dsDNA. Defects can be created by prescribed lengths and positions individually by revising the length of target staple strands. Systematic insertion of these local mechanical defects with controlled lengths and positions onto the reference design can successfully weaken the stiffness of the entire structure up to 70% without deteriorating overall structural integrity. We further developed a computational analysis platform predicting the bending stiffness of a defect-engineered DNA nanostructure quickly during the design process, to offer a versatile way of designing various DNA constructs with required mechanical stiffness in the desired shape. The comparison of two demonstrated modular design methods for controlling the stiffness of DNA origami structures is summarized in Table 1-1.

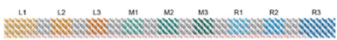

Mechanical module design	Method	Modular defect design
	Scheme	
42-nt region (~14 nm)	Module size	0.3~1.7 nm
7	Number of modules	148~169
10-11 staples per each section	Motif	Nicks at individual staples
Reduce the number of dsDNA	Design method	Make 1~5-nt ssDNA
Yes	Scaffold route conservation	Yes
No (locally collapsed)	Cross-section conservation	Yes
Bent / hinged structures	Usage	Flexible bundle structures

Table 1-1. Comparison of two modular design methods to control the stiffness of DNA origami nanostructures.

1.3. Materials and methods

DNA and reagents. M13mp18 single-stranded DNA (7,249 nt length) was purchased from New England Biolabs (N4040s). All staple DNA oligonucleotides were provided by Bioneer Corporation (www.bioneer.co.kr) with 50 nM of synthesis scale and BioRP purification method. The molecular weight of all staples was verified with the theoretical values by matrix-assisted laser desorption/ionization time-of-flight mass spectrometry (MALDI-TOF) from the provider. DI water, TAE buffer, and MgCl_2 solution with molecular biology grade were purchased from Sigma-Aldrich.

Design and assembly of DNA origami structures. Staple sequences of DNA origami structures were designed using caDNAno software¹¹. The final folding mixture had 10 nM concentration of scaffold DNA, 100 nM of each staple strands, 1×TAE buffer (40 mM Tris-acetate and 1 mM EDTA) and 20 mM of MgCl_2 . For self-assembly process, 50 μL of the mixture was annealed with a temperature gradient from 80°C to 65°C by -0.25°C per minute and 65°C to 25°C by -1°C per hour in a thermocycler (T100, Bio-Rad).

Agarose gel electrophoresis. Annealed DNA origami structures were electrophoresed using 1.5% agarose gels containing 0.5×TBE (45 mM Tris-borate and 1 mM EDTA, Sigma-Aldrich), 12 mM MgCl_2 , and 0.5 $\mu\text{g/mL}$ of ethidium bromide (EtBr, Noble Bioscience Inc.). Samples loaded in an agarose gel were allowed to migrate for 1.5 hours at 75 V bias voltage ($\sim 3.7 \text{ V/cm}$) in an ice-water cooled chamber (i-Myrun, Cosmo Bio CO. LTD.). Gel imaging was performed using GelDoc XR+ device and Image Lab v5.1 program (Bio-Rad).

AFM imaging. To avoid the possibility of unintended deformation or change of

mechanical properties of the DNA origami structures induced by EtBr intercalation and mechanical damaging during gel electrophoresis, only unpurified samples were used in AFM measurement. Annealed DNA origami samples were diluted with the folding buffer (1×TAE, 20 mM MgCl₂) up to 0.05× of the initial sample concentration, whose values were chosen to have optimal sample density on the substrate. 20 µL of diluted samples were deposited on a freshly cleaved mica substrate (highest grade V1 AFM Mica, Ted-Pella Inc.). After incubation for 3 to 5 min in ambient condition (~ 25 °C), the substrate was washed with DI water and gently dried by N₂ gun (< 0.1 Kg/cm²). If droplets are remaining on the substrate, they were removed by Kimtech Science Wiper. AFM images were taken by NX10 (Park Systems) using non-contact mode in SmartScan software. A PPP-NCHR probe having a spring constant of 42 N/m was used in the measurements (Nanosensors). Non-contact mode, having natural frequency about 290 to 300 kHz was used to measure typically 5 µm × 5 µm of sample area in 1024 × 1024 pixel resolution by using SmartScan software. All measured images were flattened with linear and quadratic order using XEI 4.1.0 program (Park Systems) prior to further analysis.

Chapter 2. Stiffness control by mechanical modules

2.1. Introduction

By utilizing the extensive design space of scaffolded DNA origami, a number of different structures were created including 2D planar sheets^{4,44}, 3D bundle structures with various shapes and curved forms^{10,45,46}, polyhedra^{47,48}, and wireframe-based assemblies with complex geometry^{12,24}. Also, there has been many attempts to construct dynamic structures whose direction and range of motion can be programmed³⁹, in order to be used as kinematic components^{39,40}, high-resolution positioners^{33,49}, mechanical testing units³²⁻³⁶, and reconfigurable structures operated by fuel strands or external stimuli^{27,30,31,50-52}.

To make them, the scaffold pathway, determined by the cross-section shape of DNA bundles and the layout of scaffold crossovers, is a primary design parameter. For structures with curved or flexible regions used as vertices or rotational joints, the modification of scaffold pathway at those regions has been adopted so far to change the helicity of DNA bundles⁴⁵ or reduce the number of DNA helices at the cross-section^{27,32,33,39,40,47-49}. A disadvantage of this approach is that a designer has to replace a large number of staple strands when the design is in need of revision even slightly, because the modification of the pre-determined scaffold pathway induces the sequence alteration of related staples even though they remained at the same position in the structure. It has been considered as an innate and inevitable limitation of using a long scaffold with predetermined sequence. Therefore, modular design

Figures and texts in this chapter were reprinted from Lee, C. *et al.*, Polymorphic design of DNA origami structures through mechanical control of modular components. *Nat. Commun.* **8**, 2067 (2017).

approaches, successfully employed in small-sized tiles or brick-based origami^{53,54}, have not been widely introduced yet in scaffolded DNA origami despite its usefulness for programming a wide range of variations in the bent shape and mechanical stiffness of the structure. A modular design method using two-dimensional repeating scaffold pathway to create two- and three-dimensional structures was only recently reported⁵⁵, though it excludes conventional lattice packing designs¹⁰ and has limited ability to control mechanical stiffness of the module. Such limitation puts a significant burden in terms of cost and time in the laboratory-scale synthesis, design modification and optimization of various DNA origami structures, acting as a major obstacle to their widespread use in many related research fields. While some other approaches to reducing the fabrication cost were reported^{14,56}, they require a custom scaffold for each structure.

Here we demonstrate polymorphic variation of the reference, 12-helix bundle design, by selective replacement of constituting staples in desired modules only. We find the controllable range of bending stiffness and included angle of the structure, as well as the folding characteristics depending on the structural complexity and rigidity. Since our design method is based on the conventional lattice-packing rule¹⁰ and compatible with commonly used design program¹¹, it is expected to be adopted in DNA nanostructure field easily and yield diverse structural variations with a broad range of application.

2.2. Design method

Our modular design method starts from partitioning the structure by drawing a periodic scaffold path filling the cross-section. A unit module region is sandwiched between two cross-sections consisting of aligned scaffold crossovers, named as seam regions (Fig. 2-1a). These scaffold seam regions play a central role in blocking the propagation of sequence alteration as well as in increasing the structural stability. Basically, a structure module is constructed by filling the helices in the module region with staples using hexagonal lattice-packing¹⁰, and remains in rigid state. To make a flexible hinge module having rotational degree of freedom, we can simply eliminate the existing staples constituting the structure module while maintaining scaffold strands at the cross-section (Fig. 2-1b), instead of reducing the number of DNA helices as in the previous studies^{27,39,40,47,49}. The bending stiffness of the hinge module can be tuned by controlling the number of dsDNA and staple crossovers inside the hinge module. We also incorporate a long scaffold helix passing through the body into our design as an adjuster strand^{27,57}, whose length can easily be varied by the adjuster module (Fig. 2-1c). As it shortens, the included angle of the structure is decreased, and the remaining part of the adjuster strand is stored in a reservoir at the end of the structure. The adjuster strand is basically formed as dsDNA by the aid of strut staples.

We found that both hinge module and adjuster strand were necessary to create a uniformly bent monomer structure as intended. Structures having a hinge module at the center of the body without an adjuster strand did not bend properly into the target shape. More than half of the monomer structures remained straight even though the most flexible hinge module was used (Fig. 2-2). When the structure

had an adjuster strand solely without any hinge module in the body, most structures formed aggregates rather than remained as a monomer (Fig. 2-3). We could observe kinks developed at arbitrary positions even if they were folded into monomeric structures.

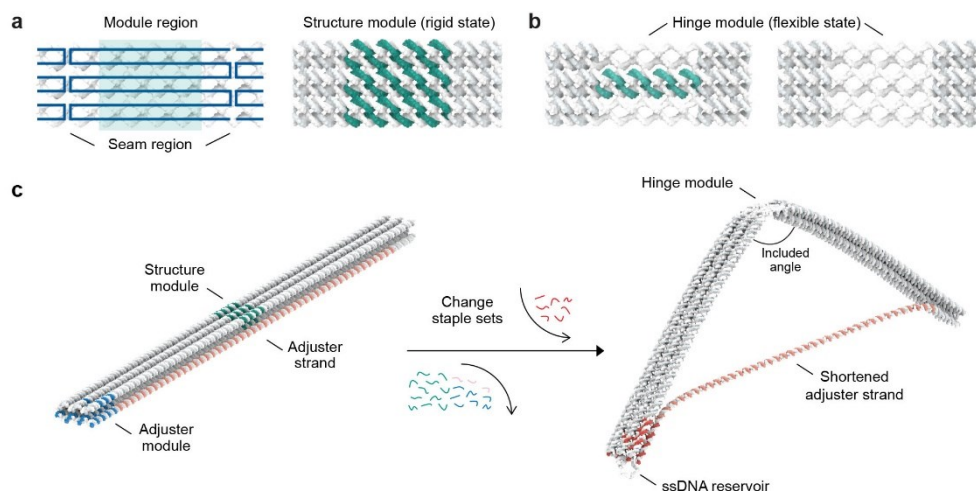


Figure 2-1. Schematic illustration of the modular design. (a) Scaffold strand is represented as blue lines (simplified to show its pathway clearly). Scaffold crossovers are aligned at the cross-section, and these sections are located at regular intervals. A module region, shown as green-shaded area, is located in between the scaffold crossover seams. Basically, all the helices of the structure module are double-stranded and all possible staple crossover positions are connected. (b) The hinge module can be made by removing the staples in the structure module, while unbound scaffold ssDNAs at the module remained at the cross-section. By controlling the number of dsDNA and staple crossovers, bending stiffness of the hinge module can be adjusted. Seam region maintained with full connection throughout the modification in order to ensure structural stability. (c) A 12-helix honeycomb-latticed bundle design to illustrate the method of controlling the shape of the structure. To make a bent structure from the straight one, staples of the structure module were removed and the adjuster module component was changed in order to make a shorter adjuster strand. Excessive strut staples were eliminated.

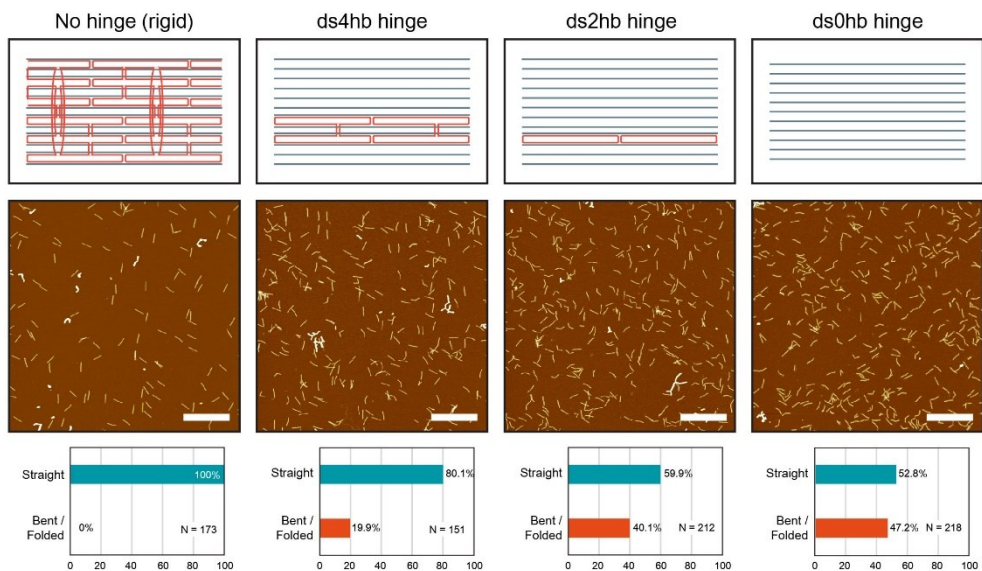


Figure 2-2. The effect of hinge stiffness without an adjuster component. The percentages of straight structures and bent or folded structures are presented below. Results show that the portion of bent and folded structures increased as the hinge became more flexible, but at least more than half of the structures remained in straight configurations. Average included angle of ds0hb hinge design was approximately 155° including straight structures. Scale bars: $1\ \mu\text{m}$.

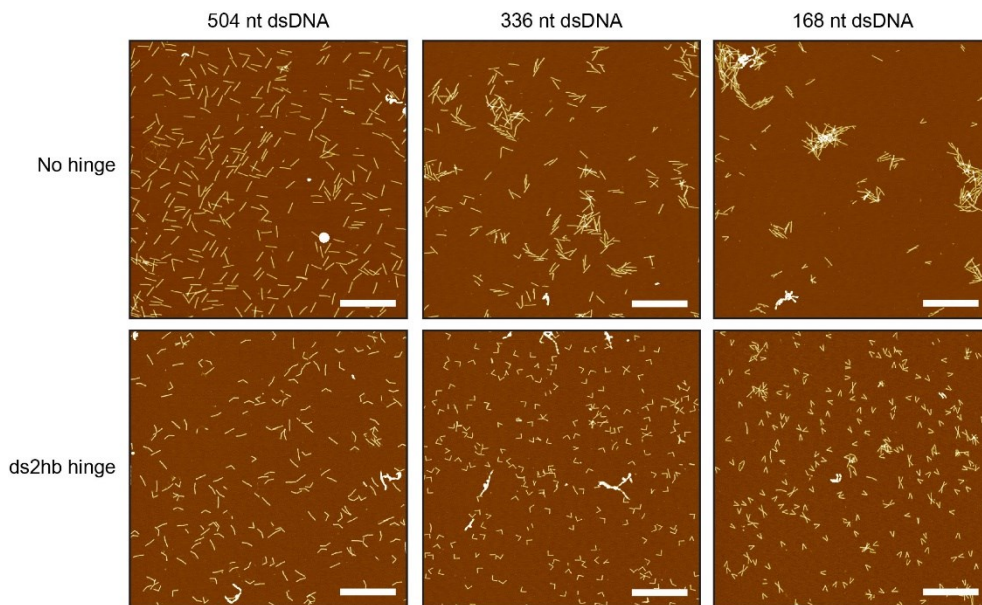


Figure 2-3. AFM images showing the effect of the hinge with different length of dsDNA adjuster strands. Here, no hinge structure with the 504-nt-long dsDNA adjuster strand is same as the reference structure in the main text, and it mostly showed straight conformation with high monomer yield. No hinge structures with shorter dsDNA adjuster strand showed decreased monomer folding yield same as the ssDNA adjuster cases. Scale bars: 1 μm .

2.3. Experimental results

To demonstrate the efficiency and versatility of our module-based design method, we designed a reference structure consisting of 12 helices on the honeycomb lattice¹⁰ that can provide polymorphic structures with minimal staple changes (Figs. 2-4 to 2-6). The reference structure, consisting of 180 unique staple strands, was folded into a straight bundle as it did not have any hinge and a 504 nucleotide (nt)-long dsDNA adjuster. Seam regions divide it into nine module regions (L1, L2, L3, M1, M2, M3, R1, R2, and R3). Seven of them from L2 to R2 serve as potential locations for hinge modules and R3 region is used as the adjuster module (Table 2-1).

To illustrate, we built 24 representative polymorphous constructs by revising the module designs while sharing most of the staples (Fig. 2). Here, all structures were designed to have planar shapes in order to be measured their geometrical features clearly by atomic force microscope (AFM). The number of replaced staples, whose sequences are different from those of the staples in the reference pool, is 7 (3.9% of the reference staples) for single-hinged structures with various hinge module locations and included angles (cases 1 to 8), 7 to 11 (3.9~6.1%) for double- or triple-hinged structures with a single adjuster strand (cases 9 to 16), and 10 to 23 (5.6~12.8%) for more complex structures that are closed-form or with double/asymmetric adjuster strand(s) (cases 17 to 24) (Table 2-2). Note that the number of staple replacement above is provided for each structure in comparison with the reference structure. In fact, when all the cases are considered, the actual number of staple replacement is much smaller since many replaced staples are shared in multiple structural variants.

All constructs were folded successfully at high monomer folding yields

ranging from 73.5% to 89.6% (Fig. 2-7 and Table 2-3). Structural yield obtained by counting the portion of correctly assembled structures among monomers from AFM images, on the other hand, ranged from 32.6% (case 16) to 93.4% (case 5) (Fig. 2-8 and Table 2-4). In general, single-hinged structures showed relatively high structural folding yield (77.5~93.4%) compared with those of double- and triple-hinged structures (32.6~84.1%), which might originate from the existence of multiple stable configurations. Structures with multiple hinges modulated by a single adjuster might have several local energy minimum states and be trapped there during annealing process with complex assembly kinetics, leading to the lack of shape homogeneity. We could circumvent this issue by assigning an adjuster for each hinge separately, which nevertheless required an increased number of modified staples (Fig. 2-9).

In addition to the diverse shape variation, we can also control the included angle of an individual hinge module more precisely. To illustrate, we introduced a flexible hinge containing two dsDNA strands at the center (M2) module region and changed the length of the adjuster by 21 nt basis. Structures with the included angle ranging from 0° (folded in half) to 150° at an interval of 15° were successfully fabricated at a high monomer folding yield and with structural integrity for the entire range (Fig. 2-10 to 2-12, and Table 2-5). Even finer control of the included angle may be achieved by adopting a shorter basis in adjuster strand or placing the adjuster closer to the hinge while it narrows the controllable range of the included angle^{40,49}. A noteworthy advantage of our design method is that only 7 to 10 new staples (3.9~5.6% of the number of reference staples) are required to control a wide range of included angles from the straight structure (Table 2-2). This portion of substituted staples is significantly smaller than that reported in previous studies (~16%⁴⁰ and ~30%⁴⁵), demonstrating the excellent efficiency of the proposed method.

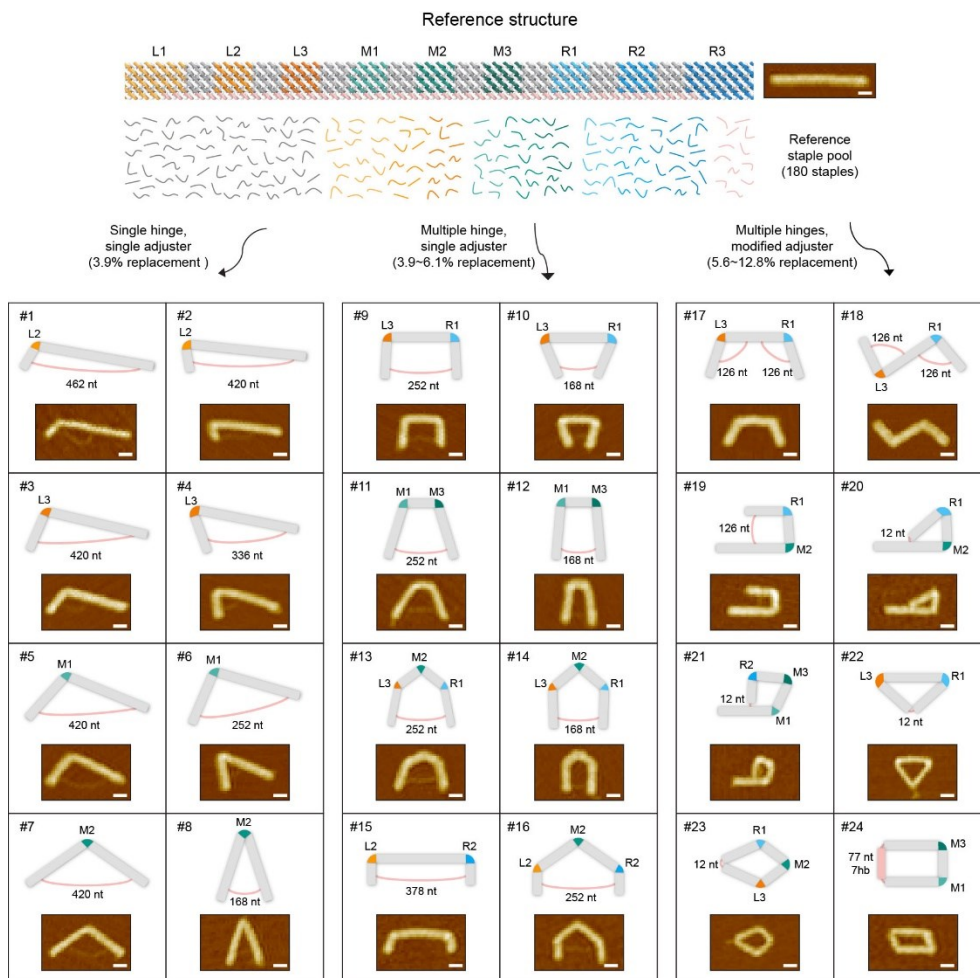


Figure 2-4. Demonstration of the 24 structural variations from the straight 12-helix honeycomb-lattice reference structure. The length of each seam region is about 28 nt (~9.5 nm), structural module L1 and R3 are 63 nt (21.4 nm), and rest of the structural modules are 35 ~ 42 nt (12 ~ 14.3 nm) long. In total, 180 staples constitute the reference structure consisting of 108 body staples, 60 seam staples, and 12 strut staples. See Figs. 2-5 and 2-6 for large-area AFM images of each design variation. Scale bars: 30 nm.

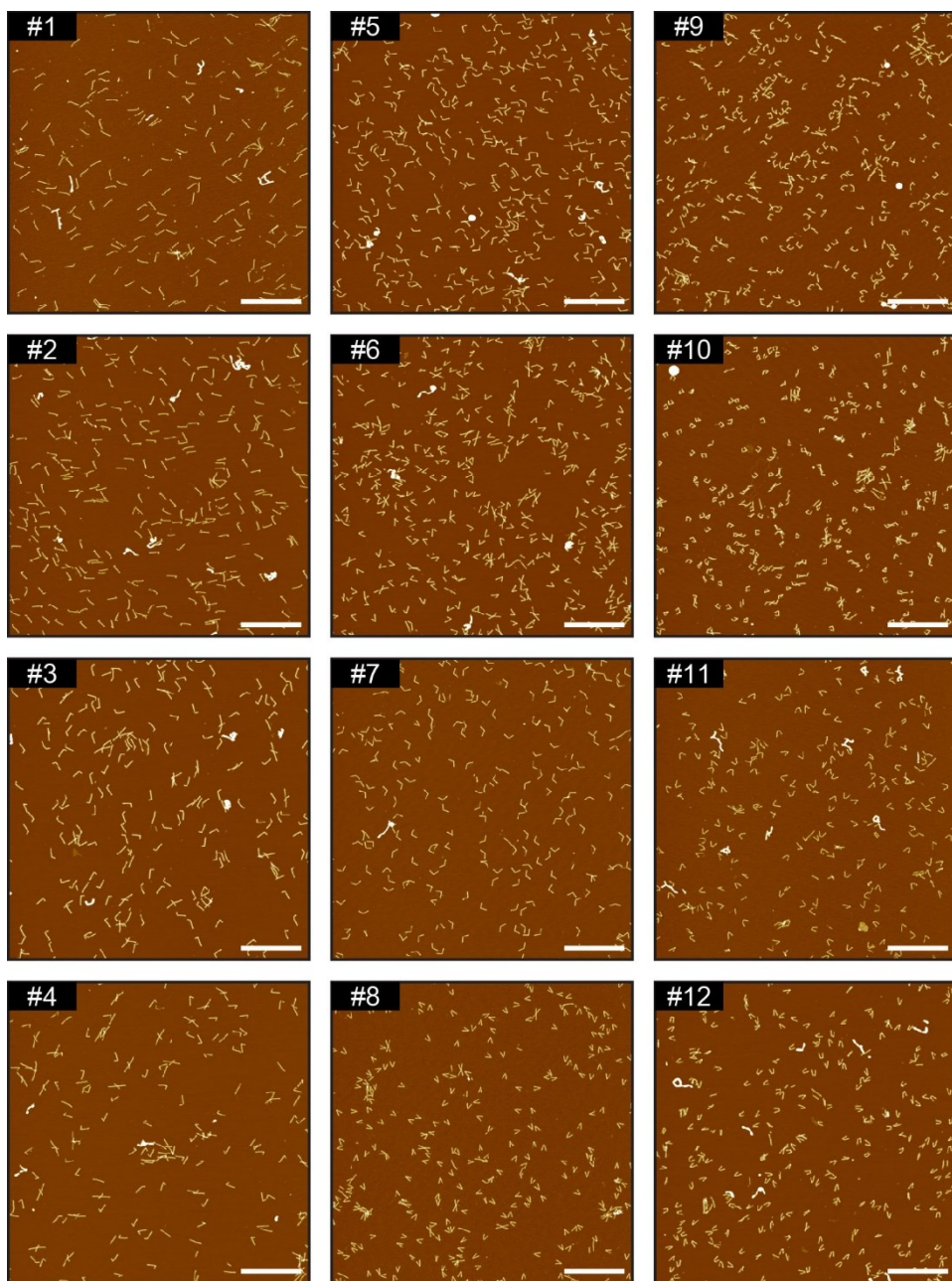


Figure 2-5. AFM images of the structures #1 to #12 shown in Fig. 2-4. Scale bars:

1 μm .

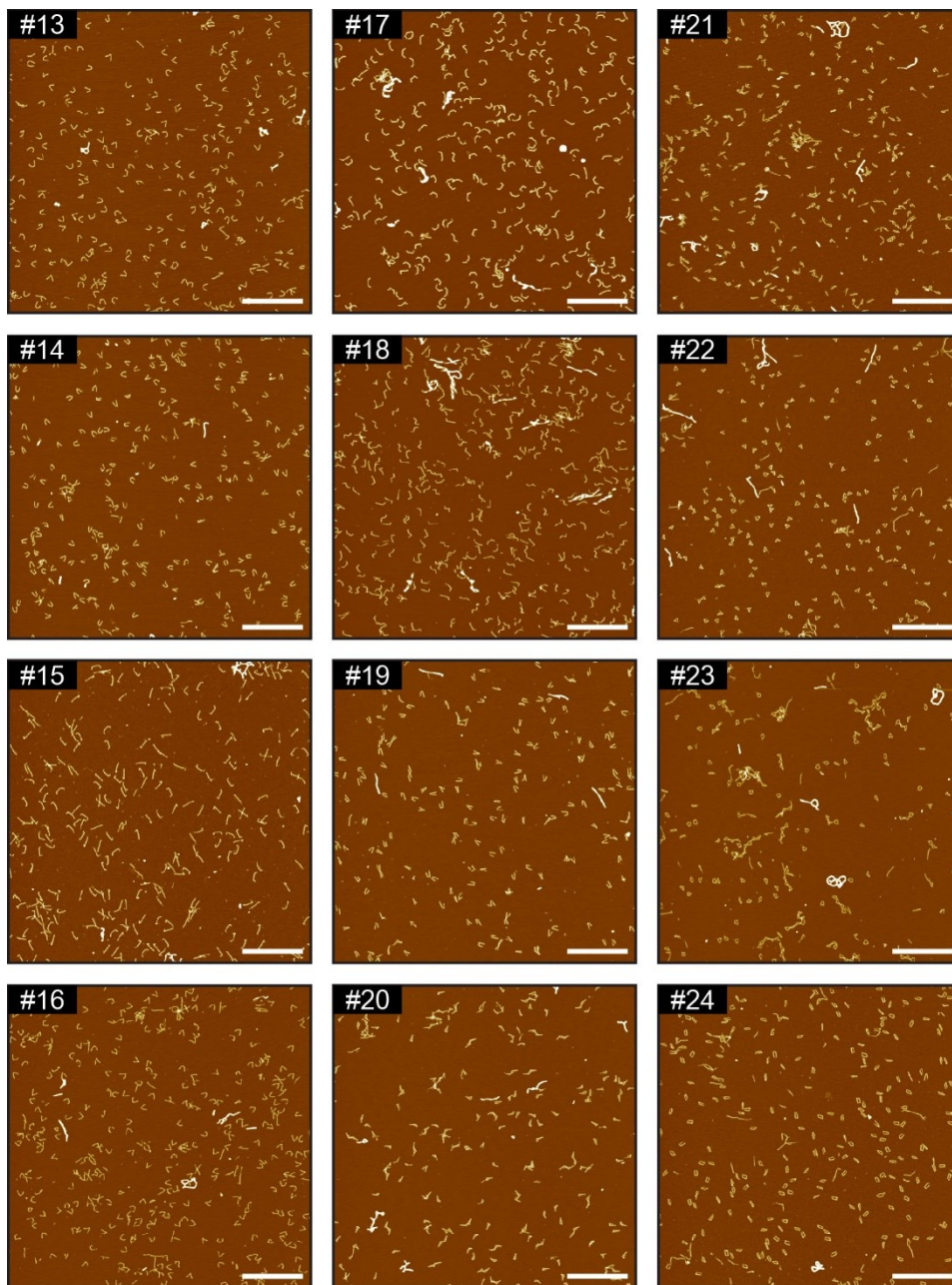


Figure 2-6. AFM images of the structures #13 to #24 shown in Fig. 2-4. Scale bars: 1 μm .

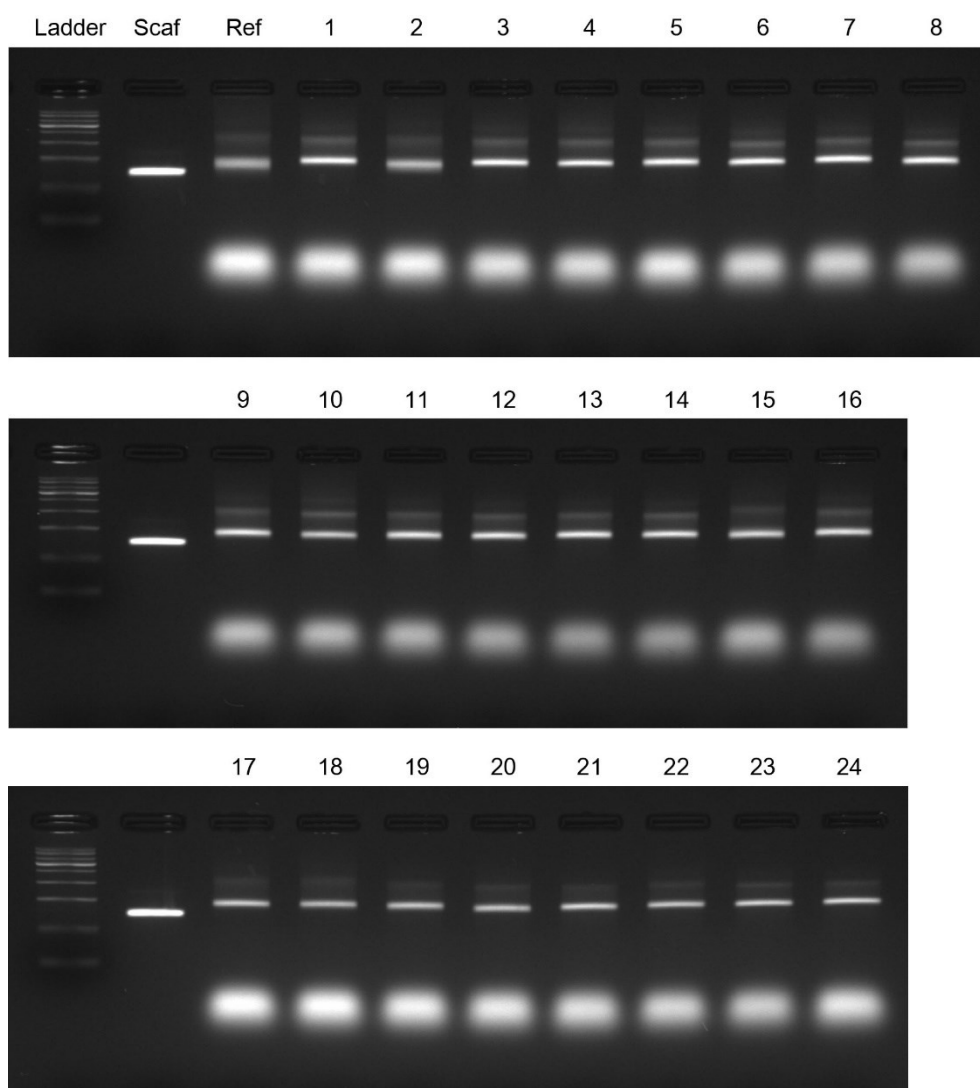


Figure 2-7. Agarose gel electrophoresis results showing the folding yield of the structures shown in Fig. 2-4.

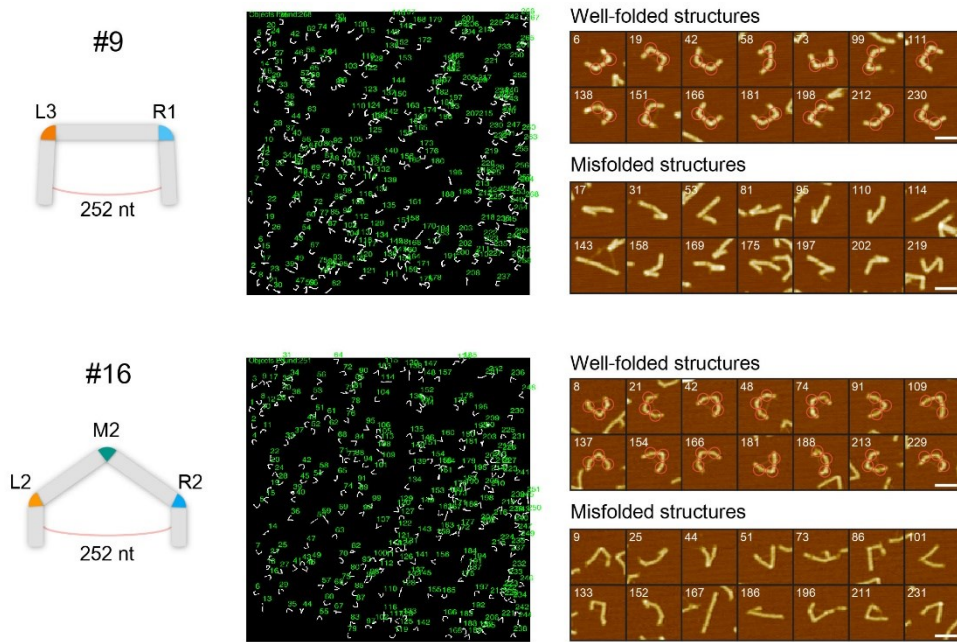
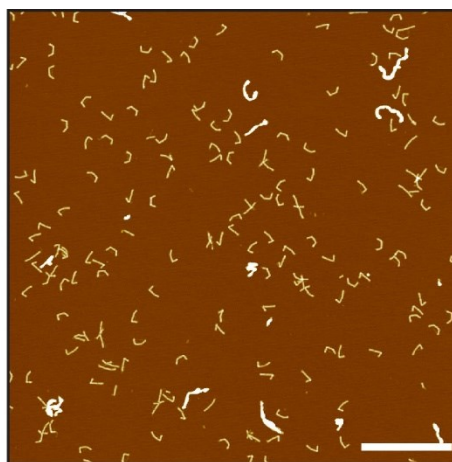
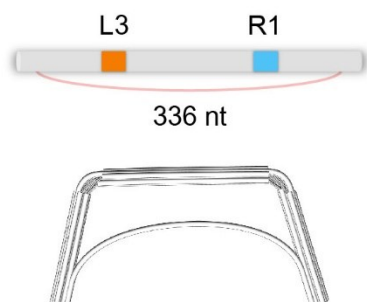


Figure 2-8. Structural folding yield analysis using AFM images. Analysis was performed to all 24 variants in Fig. 2-4, and two representative double- and triple-hinged structures are shown. After filtering aggregated structures and sediment particles by their sizes, well-folded monomer structures were manually chosen. Well-folded structure should have all hinges bent towards proper direction and amount (shown as orange circles), in accordance with the schematic design. Misfolded structures have either less number of bent region or have hinge(s) bent to opposite direction. Scale bars: 100 nm.

Single adjuster
(structural yield = 43.5%, N = 253)



Double adjuster
(structural yield = 80.3%, N = 471)

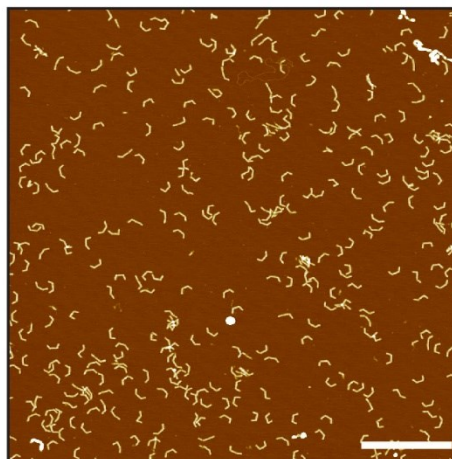
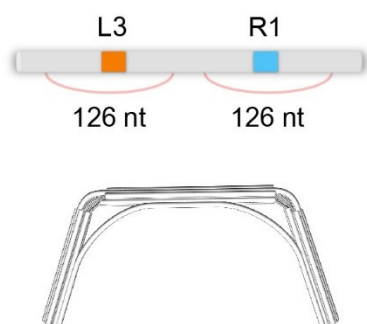


Figure 2-9. An exemplary method to circumvent local energy minima issue in the double-hinged structure with a long adjuster strand. Single adjuster design showed less portion of correctly folded structures in the experimental result. On the other hand, structural folding yield was significantly enhanced by the separation of the adjuster strand. Scale bars: 1 μm .

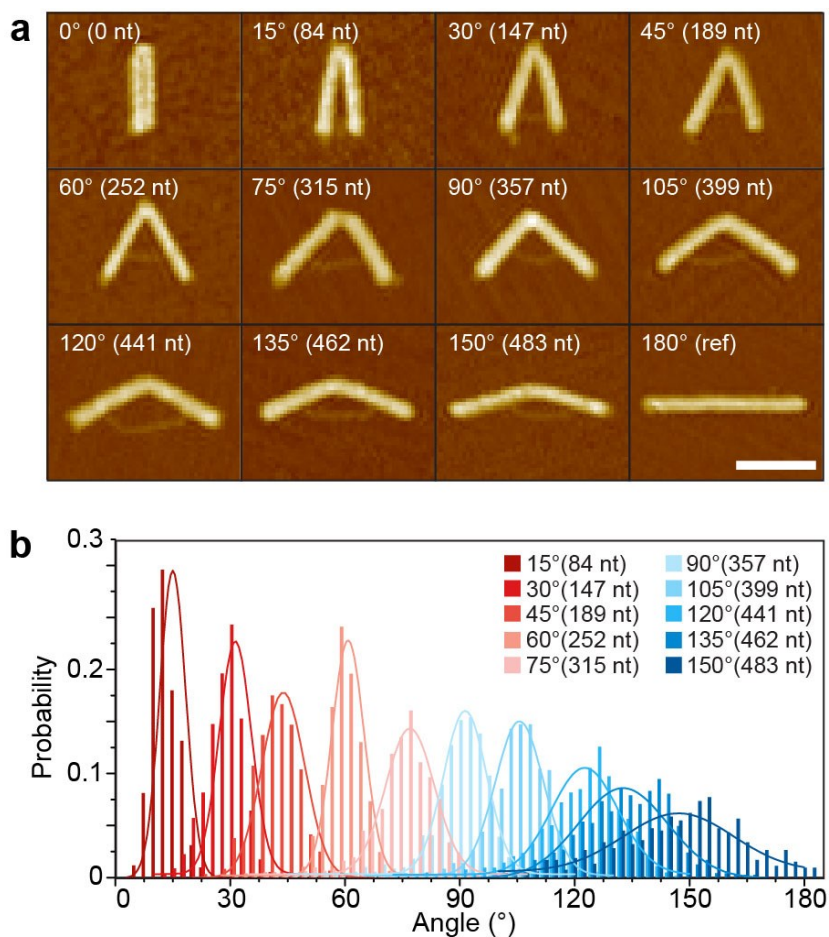


Figure 2-10. Broad and precise included angle variation of the hinge structure by controlling the length of the dsDNA adjuster strand. (a) Representative AFM images of each structure. Large-area AFM images of each structure were shown in Fig. 2-9. Scale bar: 100 nm. **(b)** Histograms of included angle distribution of each structure. Solid lines indicate the Gaussian distribution.

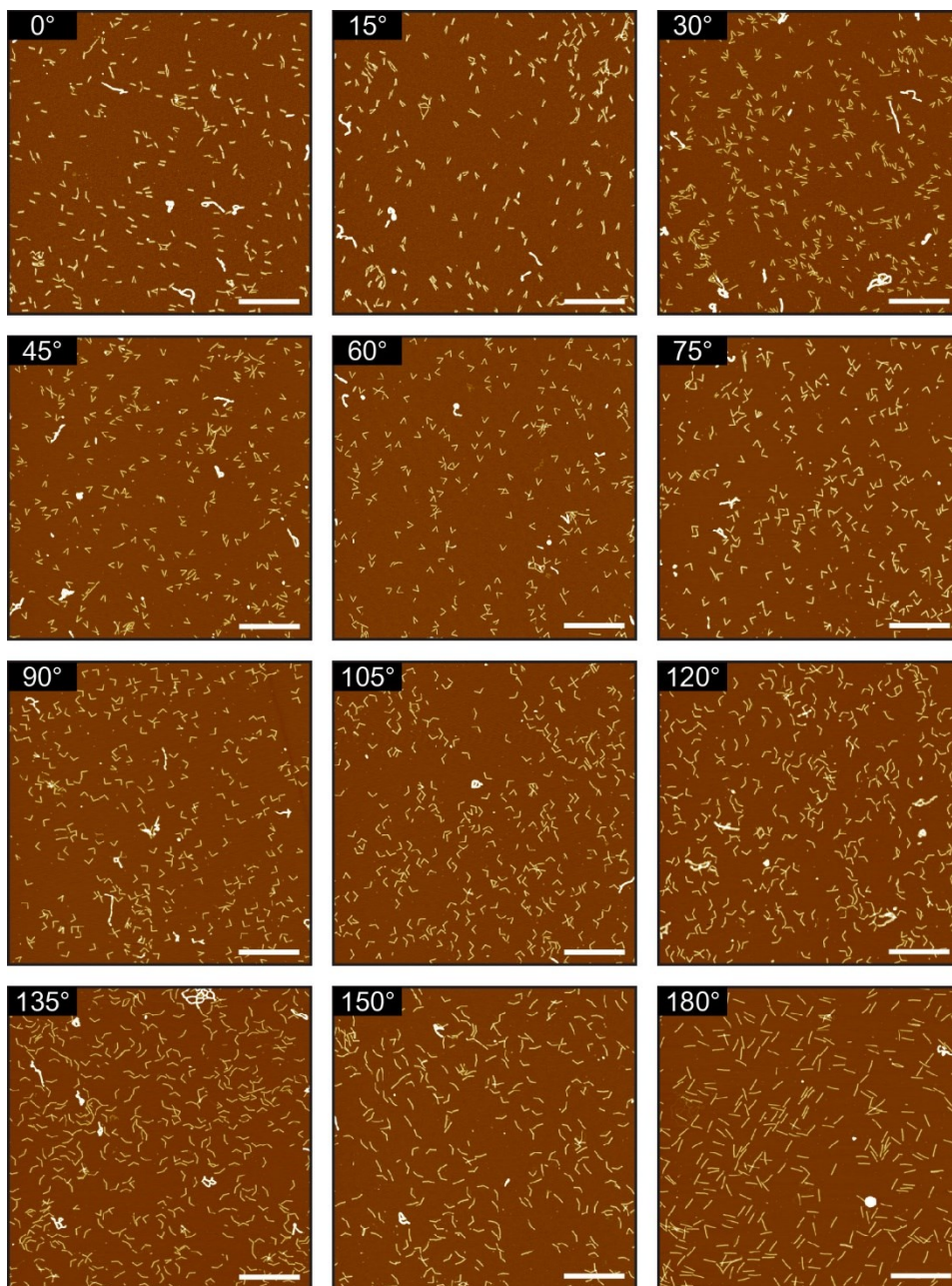


Figure 2-11. Representative AFM images of the structures with the included angle variation from 0° to 150° shown in Fig. 2-10. Scale bars: 1 μm.

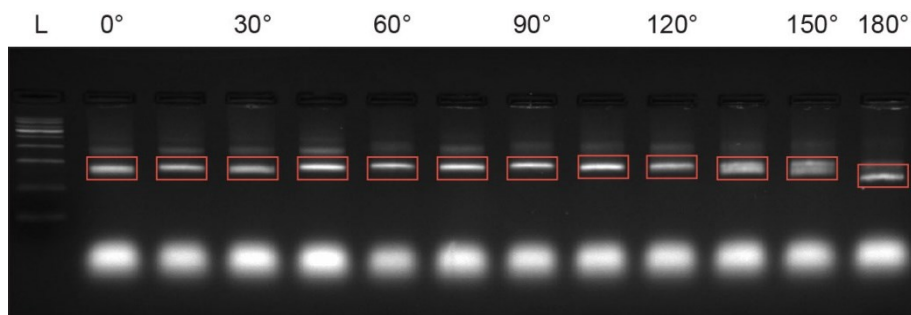


Figure 2-12. Agarose gel electrophoresis result of the designs shown in Fig. 2-10.

Orange boxes are monomer structure bands, and the bottom bands are excessive staples. L: 1 kb DNA ladder.

Left section pool												
L1 (17)	L1_01	L1_02	L1_03	L1_04	L1_05	L1_06	L1_07	L1_08	L1_09	L1_10	L1_11	L1_12
	L1_ds1	L1_ds2	L1_ds3	L1_ss4	L1_ss5							
L2 (10)	L2_01	L2_02	L2_03	L2_04	L2_05	L2_06	L2_07	L2_ss1	L2_ss2	L2_ss3		
L3 (11)	L3_01	L3_02	L3_03	L3_04	L3_05	L3_06	L3_07	L3_08	L3_ss1	L3_ss2	L3_ss3	
Middle section pool												
M1 (10)	M1_01	M1_02	M1_03	M1_04	M1_05	M1_06	M1_07	M1_ss1	M1_ss2	M1_ss3		
M2 (11)	M2_01	M2_02	M2_03	M2_04	M2_05	M2_06	M2_07	M2_08	M2_ss1	M2_ss2	M2_ss3	
M3 (10)	M3_01	M3_02	M3_03	M3_04	M3_05	M3_06	M3_07	M3_ss1	M3_ss2	M3_ss3		
Right section pool												
R1 (11)	R1_01	R1_02	R1_03	R1_04	R1_05	R1_06	R1_07	R1_08	R1_ss1	R1_ss2	R1_ss3	
R2 (10)	R2_01	R2_02	R2_03	R2_04	R2_05	R2_06	R2_07	R2_ss1	R2_ss2	R2_ss3		
R3 504 (18)	R3_01	R3_02	R3_03	R3_04	R3_05	R3_06	R3_07	R3_08	R3_09	R3_10	R3_11	
	R3_504_1	R3_504_2	R3_504_3	R3_504_4	R3_504_5	R3_504_6	R3_504_7					
Seam section pool												
A1 (7)	A1_01	A1_02	A1_03	A1_04	A1_ss1	A1_ss2	A1_ss3					
A2 (8)	A2_01	A2_02	A2_03	A2_04	A2_05	A2_ss1	A2_ss2	A2_ss3				
A3 (7)	A3_01	A3_02	A3_03	A3_04	A3_ss1	A3_ss2	A3_ss3					
A4 (8)	A4_01	A4_02	A4_03	A4_04	A4_05	A4_ss1	A4_ss2	A4_ss3				
A5 (7)	A5_01	A5_02	A5_03	A5_04	A5_ss1	A5_ss2	A5_ss3					
A6 (8)	A6_01	A6_02	A6_03	A6_04	A6_05	A6_ss1	A6_ss2	A6_ss3				
A7 (7)	A7_01	A7_02	A7_03	A7_04	A7_ss1	A7_ss2	A7_ss3					
A8 (8)	A8_01	A8_02	A8_03	A8_04	A8_05	A8_ss1	A8_ss2	A8_ss3				
dsDNA adjuster strut staples												
ADJ (12)	ADJ_01	ADJ_02	ADJ_03	ADJ_04	ADJ_05	ADJ_06	ADJ_07	ADJ_08	ADJ_09	ADJ_10	ADJ_11	ADJ_12

Table 2-1. Reference staple set. Based on the reference staples here, we can easily constitute the staple sets for structural variations.

Structures shown in Fig. 2-4												
	#1	#2	#3	#4	#5	#6	#7	#8	#9	#10	#11	#12
Eliminated staples	18	19	20	22	19	23	20	26	35	37	33	35
New staples	7	7	7	7	7	7	7	7	7	7	7	7
Total staples	169	168	167	165	168	164	167	161	152	150	154	152
Staple change	3.9%	3.9%	3.9%	3.9%	3.9%	3.9%	3.9%	3.9%	3.9%	3.9%	3.9%	3.9%
	#13	#14	#15	#16	#17	#18	#19	#20	#21	#22	#23	#24
Eliminated staples	46	48	30	44	44	44	50	53	61	44	55	40
New staples	9	9	7	11	20	23	19	19	19	10	14	23
Total staples	143	141	157	147	156	159	149	146	138	146	139	163
Staple change	5.0%	5.0%	3.9%	6.1%	11.1%	12.8%	10.6%	10.6%	10.6%	5.6%	7.8%	12.8%
Structures shown in Fig. 2-8												
	0°	15°	30°	45°	60°	75°	90°	105°	120°	135°	150°	180° (ref)
Eliminated staples	30	28	27	26	24	23	22	21	20	19	19	0
New staples	7	9	10	10	9	10	10	10	10	9	10	0
Total staples	157	161	163	164	165	167	168	169	170	170	171	180
Staple change	3.9%	5.0%	5.6%	5.6%	5.0%	5.6%	5.6%	5.6%	5.6%	5.0%	5.6%	0%

Table 2-2. The number of eliminated and replaced staples compared with the reference structure. The amount of staple change is defined as the ratio of the staples having different sequences from those of the reference staple set (the number of new staples divided by the number of reference staples).

Structure	Ref	#1	#2	#3	#4	#5	#6	#7	#8
Monomer folding yield	82.7%	77.2%	80.2%	78.0%	76.2%	77.0%	75.4%	78.2%	77.4%
Structure	#9	#10	#11	#12	#13	#14	#15	#16	
Monomer folding yield	79.7%	73.5%	82.8%	81.7%	82.2%	78.8%	82.1%	78.5%	
Structure	#17	#18	#19	#20	#21	#22	#23	#24	
Monomer folding yield	81.6%	80.7%	85.0%	84.4%	86.3%	89.3%	87.3%	89.6%	

Table 2-3. Monomer folding yield of all structures calculated from gel electrophoresis in Fig. 2-7. The monomer folding yield of each structure was calculated as the intensity ratio between the leading monomer band and all bands.

Structure	Ref	#1	#2	#3	#4	#5	#6	#7	#8
Num of sample	281	305	408	302	338	258	467	364	410
Num of well-folded structures	273	263	342	279	262	241	410	336	380
Structural folding yield	97.2%	86.2%	83.8%	92.4%	77.5%	93.4%	87.8%	92.3%	92.7%
Structure	#9	#10	#11	#12	#13	#14	#15	#16	
Num of sample	497	327	382	432	443	397	370	485	
Num of well-folded structures	313	233	208	245	190	184	155	158	
Structural folding yield	63.0%	71.3%	54.5%	56.7%	42.9%	46.3%	41.9%	32.6%	
Structure	#17	#18	#19	#20	#21	#22	#23	#24	
Num of sample	471	257	270	262	325	352	274	433	
Num of well-folded structures	378	120	131	186	173	296	110	254	
Structural folding yield	80.3%	46.7%	48.5%	71.0%	53.2%	84.1%	40.1%	58.7%	

Table 2-4. Structural folding yield result of all 24 structures shown in Fig. 2-4.

Structural folding yield is defined as the number of well-folded structures divided by the number of samples.

Target	15°	30°	45°	60°	75°	90°	105°	120°	135°	150°
Num of samples	517	576	606	776	623	715	727	637	708	530
Average	14.0°	29.3°	42.4°	59.0°	74.5°	88.4°	103.0°	119.1°	130.2°	143.8°
Stdev	3.3°	4.7°	5.6°	5.3°	8.5°	8.6°	7.7°	10.9°	11.5°	16.3°
R ² (Gaussian)	0.951	0.967	0.985	0.993	0.972	0.985	0.975	0.955	0.921	0.833

Table 2-5. Detailed experimental data of measured included angles shown in Fig. 2-10.

2.4. Computational shape prediction

We used a FEA-based computational tool named CanDo (computer-aided engineering for DNA origami), as previously developed by Kim D.-N. et al^{8,20}. In CanDo, dsDNA is modeled as two-node beam elements in which each node represents a basepair. The beam has proper geometry (diameter of 2.25 nm and axial rise of 0.34 nm per each base, and helicity of 10.5 basepair (bp) per turn) and mechanical properties (axial rigidity of 1,100 pN, bending rigidity of 230 pN nm², and torsional rigidity of 460 pN nm²), which correspond to experimentally validated values of dsDNA. Also, a Holliday junction (crossover) is modeled as two rigid beams.

We made some modification in the modeling of DNA origami structures compared with original CanDo. At first, DNA single-strand breaks, known as nicks, are modeled having the same bending and torsional stiffness as dsDNA, since the effect of nick stiffness is negligible in terms of predicting an equilibrium included angle of the structures designed here. Also, we adopted wormlike-chain (WLC) model to describe a ssDNA strand as an entropic spring, instead of modified freely jointed chain (mJFC) model used in previous CanDo. It is mainly due to enhancing the accuracy of predicting tensional force of the short ssDNA at the hinge module. WLC force of ssDNA can be expressed as⁵⁸

$$F_{\text{WLC}} = \frac{k_{\text{B}}T}{L_{\text{p}}} \left[\frac{x}{L_{\text{c}}} + \frac{1}{4(1-x/L_{\text{c}})^2} - \frac{1}{4} \right] \quad (1)$$

where k_{B} denotes the Boltzmann constant, T is the temperature, L_{p} is the persistence length of ssDNA, x is the extension (end-to-end distance), L_{c} is the contour length, respectively. We set parameters as $k_{\text{B}} = 4.1124 \text{ pN nm}$, $T = 298 \text{ K}$,

$L_p = 2 \text{ nm}$, and $L_c = 0.65 \times \text{number of base}$.

For finite element analysis, equation (1) is converted to axial stress-strain relationship implemented as

$$\sigma_{\text{WLC}} = \frac{k_B T}{L_p} \left[\frac{R_0(1+\epsilon)}{L_c} + \frac{1}{4(1-R_0(1+\epsilon)/L_c)^2} - \frac{1}{4} \right] \quad (2)$$

where R_0 is the initial length and ϵ is the axial strain, respectively. Lastly, in case of modeling a hinge module consisting of only ssDNA strands, a certain amount of bases were modeled as dsDNA beams in order to give proper elastic stiffness. A more detailed and quantitative model of the hinge containing ssDNA helices may be required to increase the accuracy of CanDo shape prediction.

We applied CanDo modeling framework to our polymorphic shape variations and it provided the equilibrium folding shapes remarkably consistent with experimental observation (Figs. 2-13 and 2-14). Also, it predicted the failure of the structure formation induced by the improper arrangement of hinge position and adjuster length. When the hinge existed at a largely asymmetric position and the dsDNA adjuster was too short, the structure tended to be severely distorted and failed to be folded into a proper shape (Fig. 2-15).

In experimental observation, bending angle distribution became relatively wider for the target included angle greater than 120° (Fig. 2-10), which might originate from high variability of the hinge stiffness due to unbound scaffold ssDNA portions at the hinge module. The average end-to-end length of hinge ssDNA portions increased with the included angle, which elevated their entropic tensional force as predicted by wormlike chain (WLC) model^{58,59} and the possibility of non-specific interactions among them, making the hinge stiffness more variable and less predictable. CanDo predictions supported our inference to some extent because

experimentally measured value of included angles lay between the value predicted by modeling ssDNA portions as non-interacting entropic springs and the value calculated by excluding them entirely from the model (Fig. 2-16). Hence, it is suggested that multiple ssDNA portions at the hinge module do not fully provide tensional forces expected from an ideal model due probably to some interactions between adjacent strands.

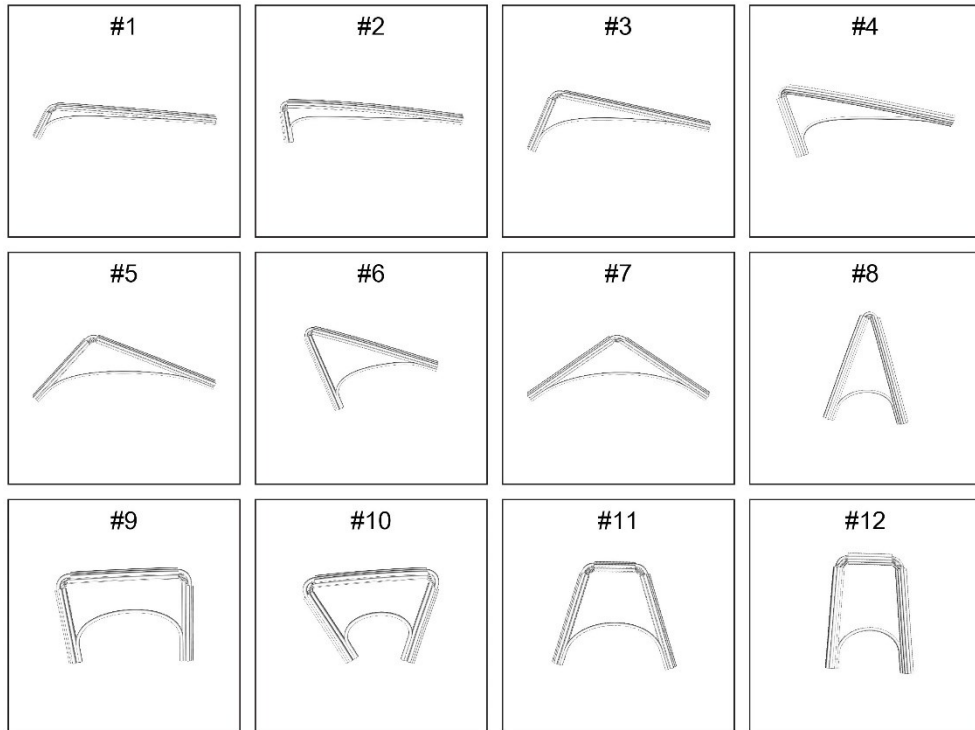


Figure 2-13. CanDo shape prediction of the structures #1 to #12 in Fig. 2-4.

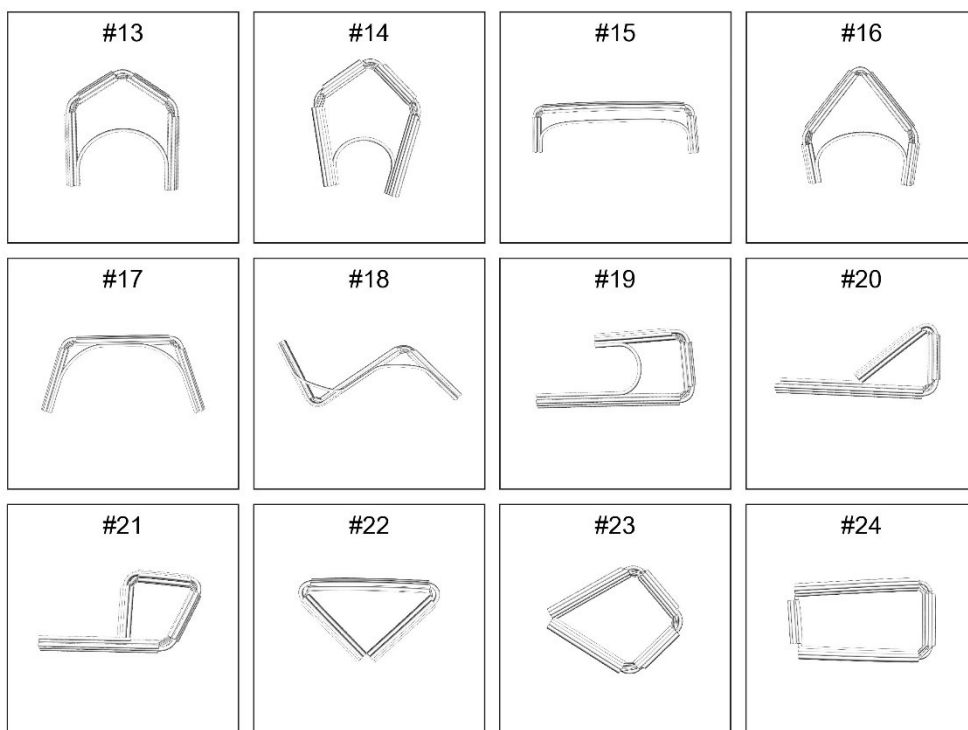


Figure 2-14. CanDo shape prediction of the structures #13 to #24 in Fig. 2-4.

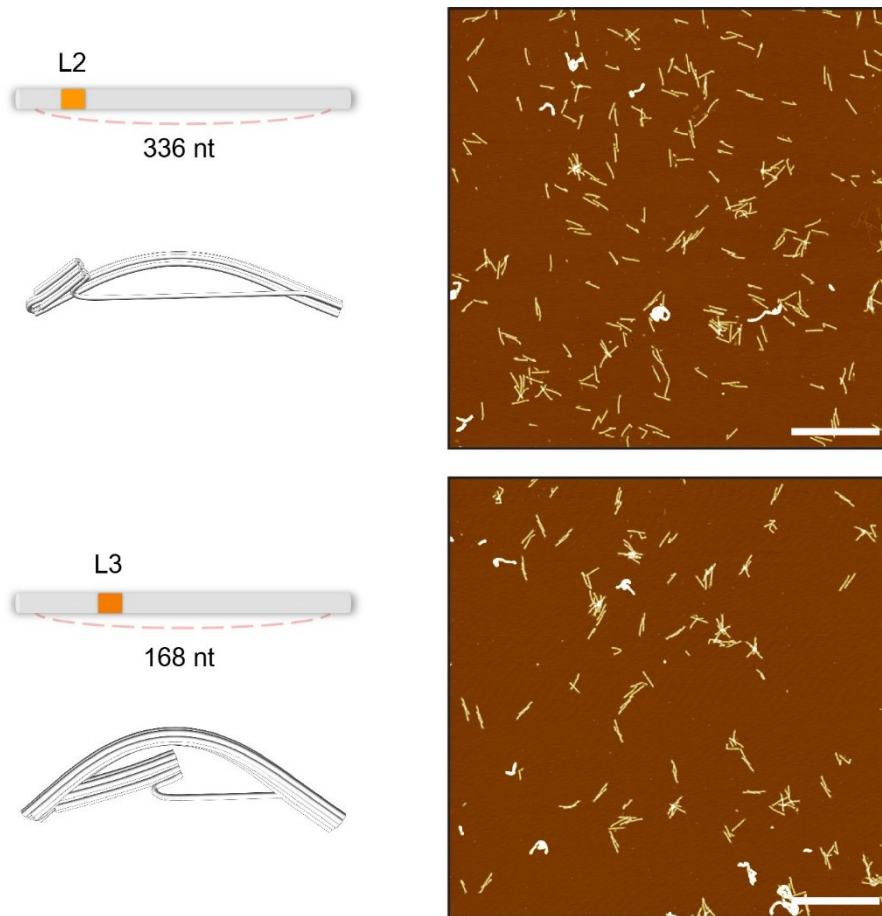


Figure 2-15. Examples of structural failure due to the geometrical distortion.

CanDo estimation predicted the collapse of the structure, and the experimental result showed low structural folding yield as well. Scale bars: 1 μm .

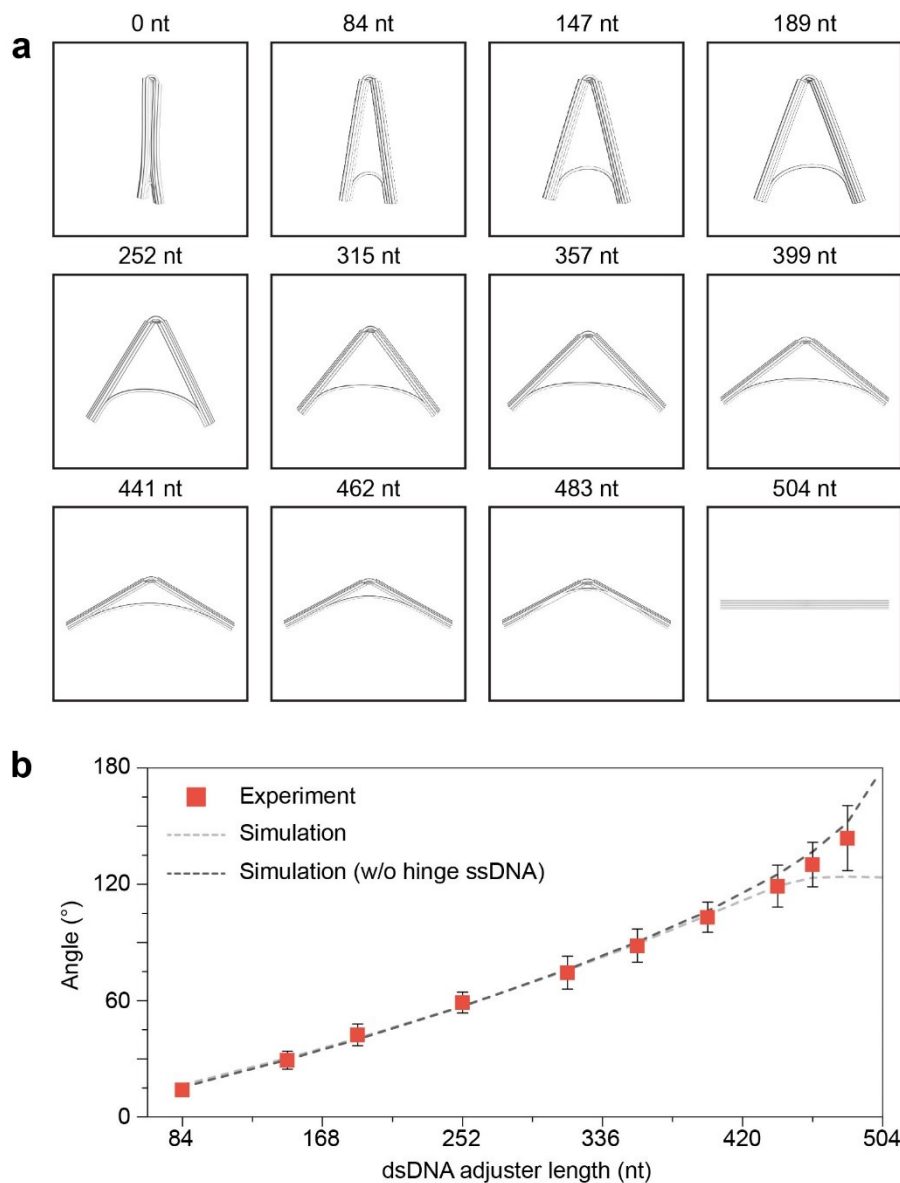


Figure 2-16. CanDo shape prediction of the structures shown in Fig. 2-10. (a) Short ssDNAs at the hinge module were included in the analysis. **(b)** Measured average included angle and CanDo analysis result. Error bars indicate standard deviation of experimental data.

2.5. Molecular dynamics simulation

In order to investigate the existence and frequency of non-specific interactions among single strands, we performed the MD simulation for structures with and without a hinge (Figs. 2-17 and 2-18). The starting atomic structures of 12-helices DNA bundles were generated using caDNAno¹¹ and CanDo²⁰. Each hinge structure was solvated in a rectangular box of the TIP3P water model⁶⁰ with approximately $160 \text{ \AA} \times 470 \text{ \AA} \times 110 \text{ \AA}$ and neutralized to reach an ion concentration of 20 mM MgCl_2 . MD simulation was performed using the package, NAMD⁶¹ with the CHARMM36 force field⁶², periodic boundary conditions, and the integration time step of 2 fs. The van der Waals and short-range electrostatic potentials were calculated using a 12 \AA cut-off. The long-range electrostatic interactions were computed using the Particle Mesh Ewald scheme⁶³ with the grid size of 1 \AA . The potential energy of each system was minimized using the conjugate gradient method. For principal component analysis (PCA), the equilibrium trajectories of each 20 ns was calculated under the NPT ensemble with constant temperature, and pressure of 298 K and 1 bar using a Langevin thermostat⁶¹ and the Nosé–Hoover Langevin piston pressure scheme⁶⁴.

The hinged structure has twelve 42-nt-long scaffold ssDNA portions at the center region (termed ds0hb hinge), whose cross-sectional shape is the same as those of the M2 module in the reference design. Since we simulated a part of the structure only near the hinge without the adjuster, MD simulation results might reflect the real condition better as the included angle becomes closer to the straight conformation. After we validated that all structures in MD simulation were within equilibrium conformation by the calculation of root-mean square deviation (RMSF) values, we

could confirm from MD trajectories that the hinged structure had higher fluctuation than the non-hinged one, and multiple non-specific interactions among ssDNA helices existed at the hinge module (Fig. 2-20). On average, 8.1% of base pairing between bases in either same or different strands was observed in the ds0hb hinge during equilibrium states from 90 to 110 ns.

Principal component analysis (PCA) was performed to characterize the mechanical rigidities from the MD simulation using configurations of phosphorus atoms of each structure in equilibrium (5,000 snapshots for 20 ns). Let $\mathbf{x}(t)$ be the atomic coordinates from MD simulation at equilibrium with a dimension of $1 \times 3N$ where N is a total number of phosphorus atoms at a saved frame. The covariance matrix is determined as⁶⁵

$$\sigma = \langle (\mathbf{x}(t) - \langle \mathbf{x}(t) \rangle) \otimes (\mathbf{x}(t) - \langle \mathbf{x}(t) \rangle) \rangle \quad (3)$$

where a symbol, \otimes indicates the tensor product, and an angle bracket is the vector of average. Then square-root-mass-weight matrix, Σ is obtained as

$$\Sigma = \sqrt{\mathbf{M}} \sigma \sqrt{\mathbf{M}} \quad (4)$$

where a mass matrix, \mathbf{M} is a diagonal matrix with elements of the atomic weight of phosphorus atom. Then we can obtain the eigenvalues, λ_n from the diagonalization of the square-root-mass-weight matrix. The quasi-harmonic frequencies, ω_n of the n^{th} mode, can be calculated as

$$\omega_n = \sqrt{\frac{k_B T}{\lambda_n}} \quad (5)$$

Elastic bending and stretching rigidities of DNA structures are approximately calculated using the quasi-harmonic frequencies based on the dynamic Euler-Bernoulli beam model as⁶⁶

$$EI_n = \frac{M\omega_n^2 L^3}{(\beta_n L)^4} \quad EA_n = \frac{M\omega_n^2 L}{n^2 \pi^2} \quad (6)$$

where EI_n and EA_n are respectively bending and stretching rigidities of the n^{th} mode for the boundary conditions of free-free ends, M and L are the total mass and the axial length of a DNA structure, and $\beta_n L$ is a known constant determined from boundary conditions, respectively ($\beta_1 L = 4.733$).

As a result, PCA of MD trajectories obtained for these hinge modules showed a stiffening of the hinge with the increase of double-stranded portions (Fig. 2-21). Strong binding of staple strands to the scaffold strand at the hinge was also observed throughout the simulation, demonstrating the stability of our hinge designs with controllable stiffness.

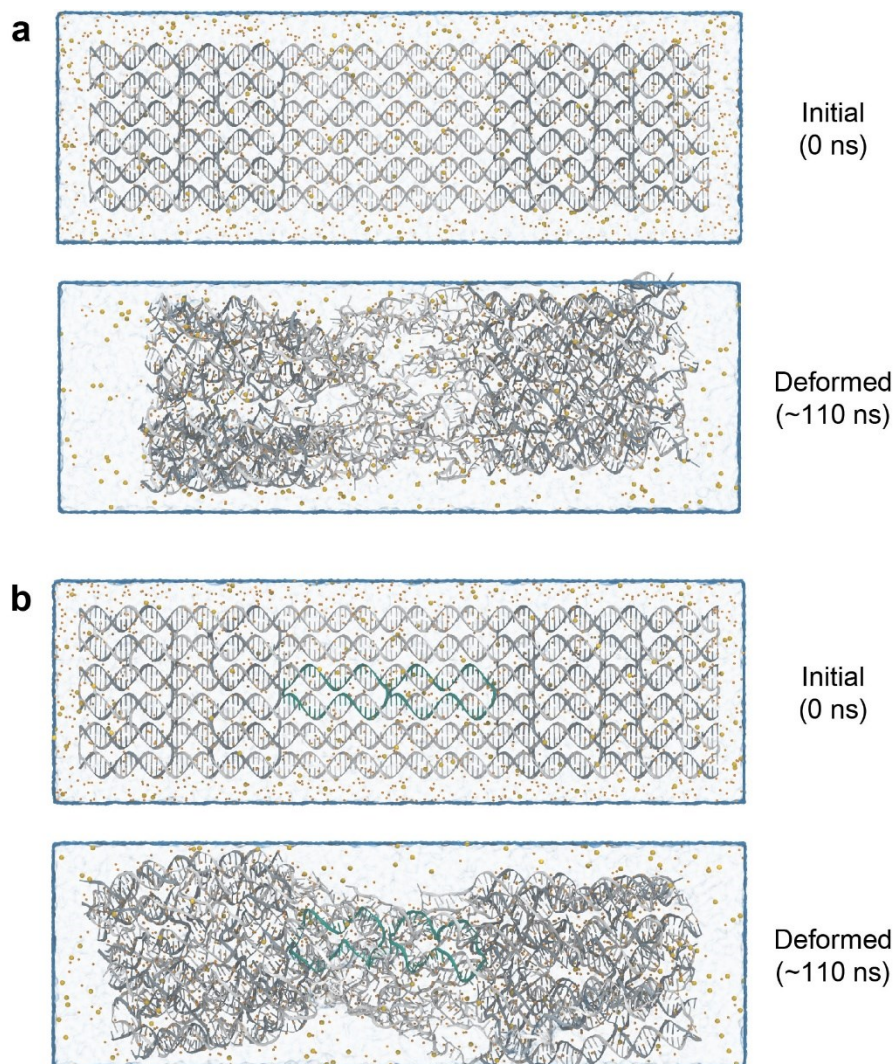


Figure 2-17. MD simulation of the ds0hb and ds2hb hinge module. Initial and final (after ~110 ns of simulation time) configurations of the **(a)** ds0hb and **(b)** ds2hb hinge structures.

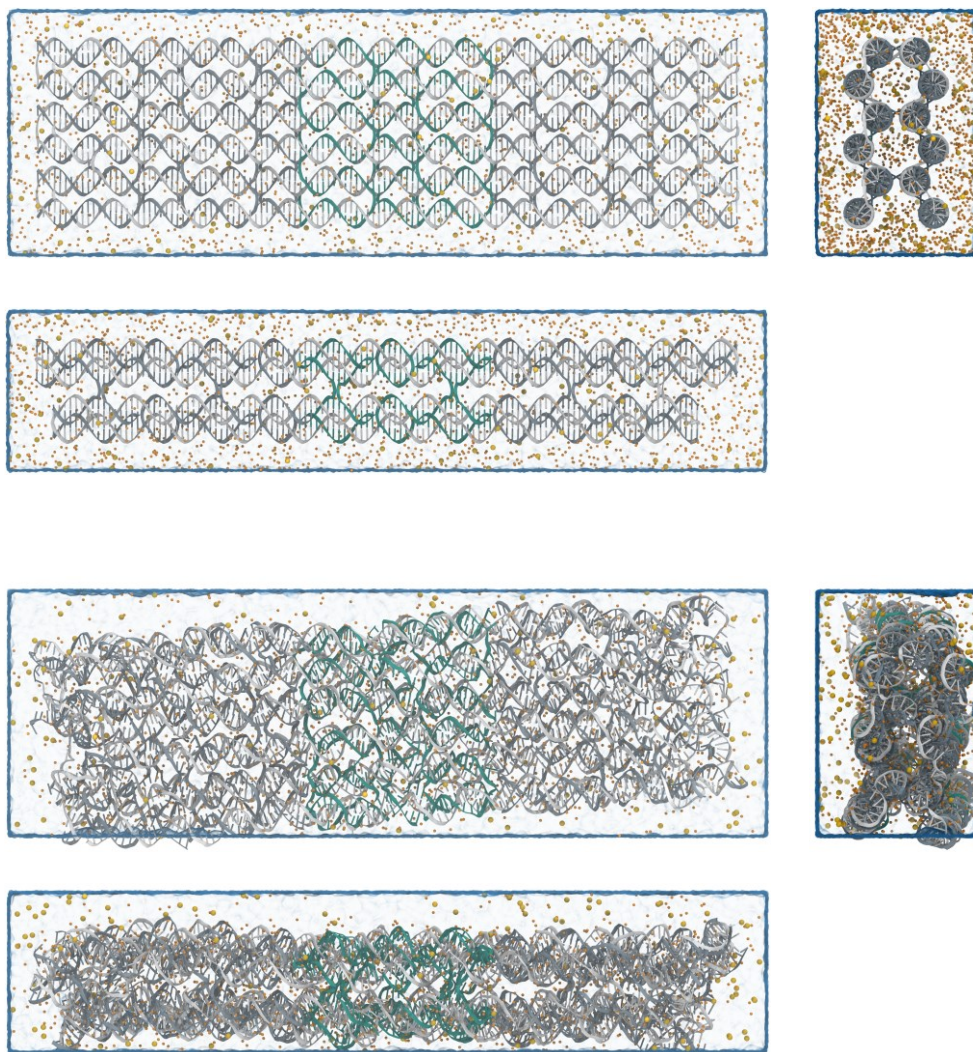


Figure 2-18. MD simulation of the ds3hb and no hinge module. Initial and final (after ~110 ns of simulation time) configurations of the **(a)** ds3hb and **(b)** no hinge structures.

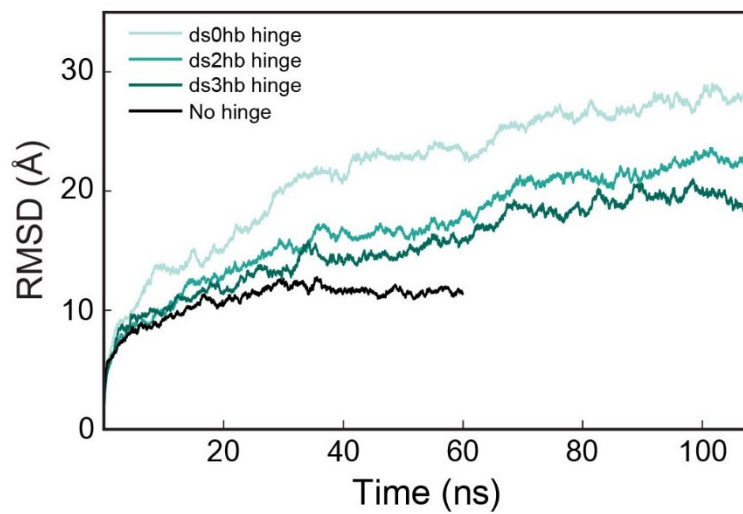


Figure 2-19. RMSD values of all designs throughout the MD simulation.

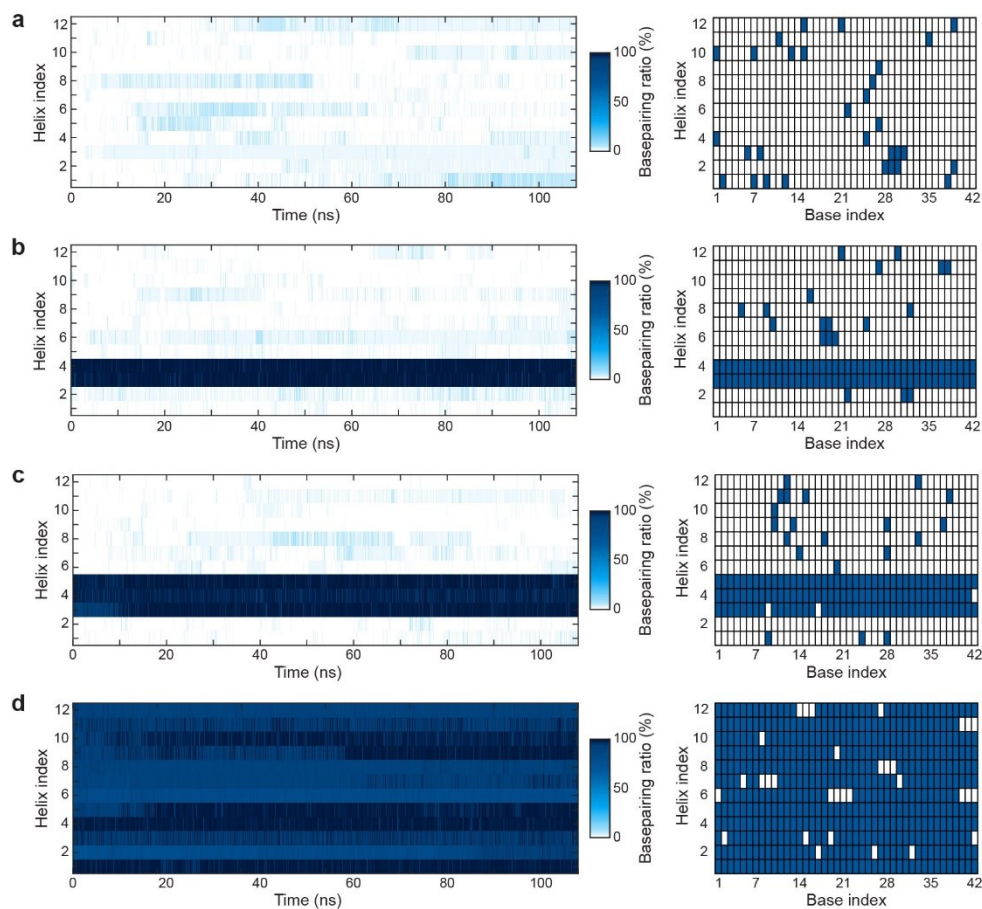


Figure 2-20. Base pairing ratio analysis from MD simulation. Base pairing ratio of each helix throughout the MD simulation and positions of the individual base pairing at the final time step of **(a)** ds0hb, **(b)** ds2hb, **(c)** ds3hb, and **(d)** no gap hinge design. Base pairing can occur by the interaction of ssDNA bases between either same or neighboring helix.

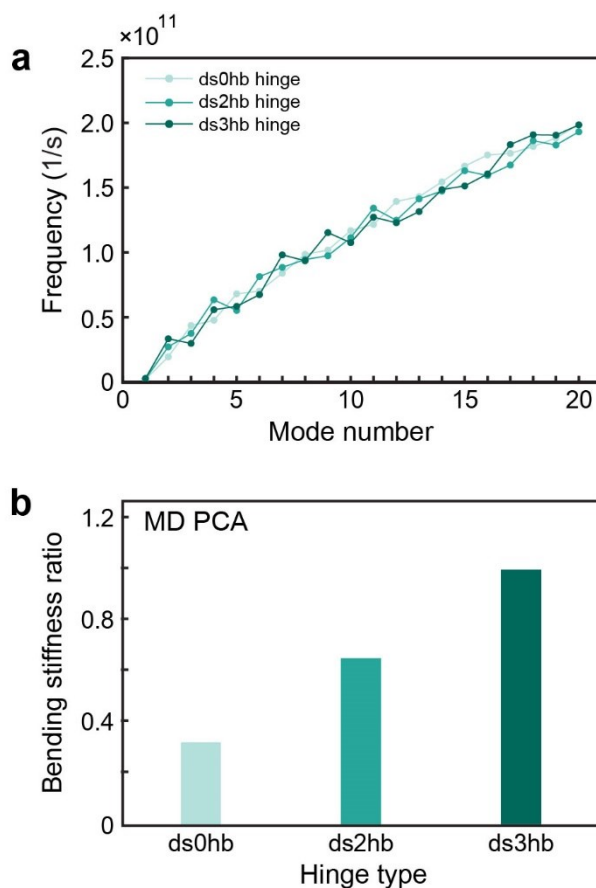


Figure 2-21. Principal component analysis (PCA) from MD simulation. (a) The natural frequencies of all hinged structures. For all cases, the first mode (having smallest natural frequency) was axial stretching and the second mode was first bending mode. **(b)** Relative bending stiffness ratios calculated from MD trajectories using PCA. Bending stiffness of the ds3hb hinge was set to 1 as a reference.

2.6. Analysis on the applicable range of hinge stiffness

To further explore the applicable range and value of the hinge stiffness, we developed five different hinge designs by varying the number of dsDNA portions and Holliday junctions at the M2 module (Fig. 2-22a). The most flexible case was a ds0hb hinge where all 11 structural staples were removed from the M2 module so that only unbound scaffold single strands remained. Stiffer hinges were then devised by adding 2 to 6 hinge staples to it leading to ds2hb, ds3hb, ds4hb, and ds6hb hinge structures where each number indicates the number of dsDNA helices at the cross-section. Results from agarose gel electrophoresis and AFM imaging indicated that stiffening the hinge deteriorated the monomer folding yield and increased the number of aggregated structures (Figs. 2-22 and 2-23). Intensity ratios of the monomer band to all bands were 85.8%, 79.1%, 69.0%, 31.1%, and 7.0% for ds0hb, ds2hb, ds3hb, ds4hb, and ds6hb hinge, respectively. A drastic drop in the number of monomeric structures was observed for structures with ds4hb hinge and stiffer ones, recommending the use of a hinge softer than ds4hb hinge in practice.

We quantified the stiffness of ds0hb, ds2hb, and ds3hb hinges by adopting a ssDNA adjuster whose tensional force was modulated through a systematic variation of their length^{35,57} and measuring the included angles (Fig. 2-24). We used a simple toy model to estimate the effective bending stiffness of the flexible hinge. The hinge module is modeled as a linear torsional spring whose spring constant is κ and equilibrium position is straight. The ssDNA adjuster strand is modeled as a nonlinear axial spring whose force-displacement relationship is followed by WLC model as described in the equation (1). By adopting assumptions that all parts of the structure except for the hinge and the adjuster strand are rigid and DNA origami

structures measured in the experiment were in the force-equilibrium state, we can use the average included angle to calculate the effective bending stiffness of the hinge, κ . It can be modeled as

$$\kappa(\pi - 2\theta) = RF_{\text{WLC}} \cos \theta \quad (7)$$

where θ denotes the half of the average included angle, R is the moment arm length defined as the length between the connecting point of the adjuster strand and the center of the hinge module (assumed as 85.7 nm), and F_{WLC} is the tensional force induced from the ssDNA adjuster, calculated from the equation (1).

From the effective bending stiffness, the total strain energy of the structure can be estimated by assuming that it is the summation of the strain energy of the hinge and ssDNA adjuster, respectively.

$$E_{\text{tot}} = E_{\text{h}} + E_{\text{s}} = \frac{1}{2}\kappa(\pi - 2\theta)^2 + \int_0^l \frac{k_{\text{BT}}}{L_{\text{p}}} \left[\frac{x}{L_{\text{c}}} + \frac{1}{4(1-x/L_{\text{c}})^2} - \frac{1}{4} \right] dx \quad (8)$$

where l is the end-to-end distance of the adjuster.

As a result, the estimated values of bending stiffness on average were 25.3, 33.8, and 49.6 pN nm rad⁻¹ for ds0hb, ds2hb, and ds3hb hinge, respectively (Fig. 24b). Using the estimated hinge stiffness, we calculated the total strain energy of each hinge design as a function of included angle by summing the strain energies in the hinge module and the ssDNA adjuster assuming negligible deformation in other modules (Fig. 24c). The mean included angle determined experimentally coincided with the value where the total strain energy became minimum⁶⁷. As a hinge got stiffer, the minimum strain energy increased naturally, and the strain energy became more concentrated in the hinge module (Fig. 2-25), which partly explained the deterioration of the folding yield of monomeric structures with stiff hinges. Hinge staples, when the designed hinge stiffness was too high, might tend to be bound to

other neighboring structures to form less-bent multimeric structures, which would be energetically more favorable than the formation of monomeric hinge structures as observed in AFM images. For structures with the dsDNA adjuster, the mean included angle was almost independent of the hinge stiffness whereas it was still dependent on the length of the adjuster. (Fig. 2-26). Also, their included angles were much less deviated from the mean value compared to the structures adjusted by ssDNA. The mean and deviation of the included angle could be more finely tuned by simply adding a few strut staples binding to the adjuster and controlling the portion of dsDNA (Fig. 2-27). Therefore, it offers a versatile way of programming the target mean angle and flexibility of hinge structures statically and also dynamically through addition or removal of required staples^{31,50}.

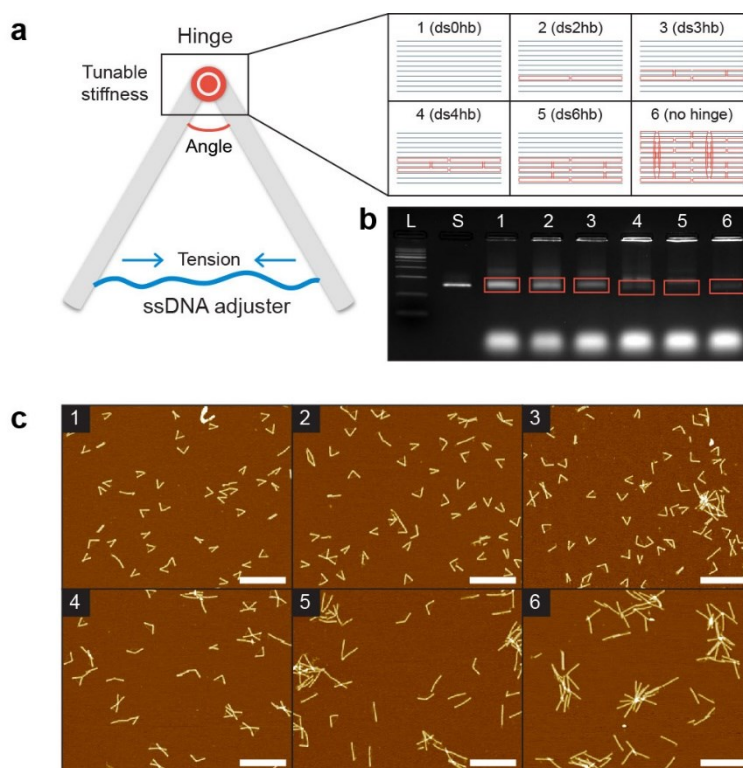


Figure 2-22. Analysis of the hinge stiffness. **(a)** Schematic illustration of the test design. Here, a ssDNA adjuster strand was used to make it as a tensional component. The stiffness of the hinge can be controlled by changing the number of dsDNA and staple crossovers at the hinge section. **(b)** Agarose gel electrophoresis result. Orange boxes are monomer structure bands, and the bottom bands are excessive staples. L: 1 kb DNA ladder. S: M13mp18 scaffold. 1–6: folded structures with each hinge stiffness. **(c)** AFM images of each hinge design. See Fig. 2-23 for large-area images. Scale bars: 500 nm.

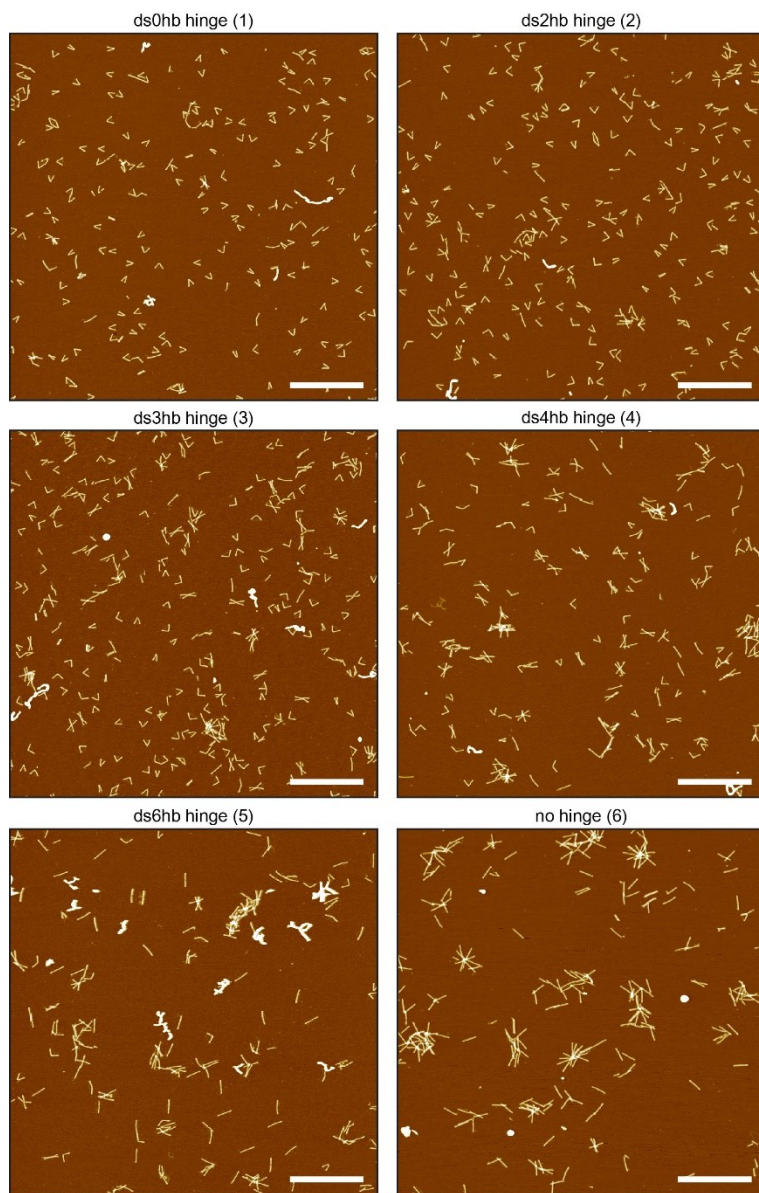


Figure 2-23. Large-area AFM images showing the relationship between hinge stiffness and monomer folding yield in Fig. 2-22. Scale bars: 1 μm .

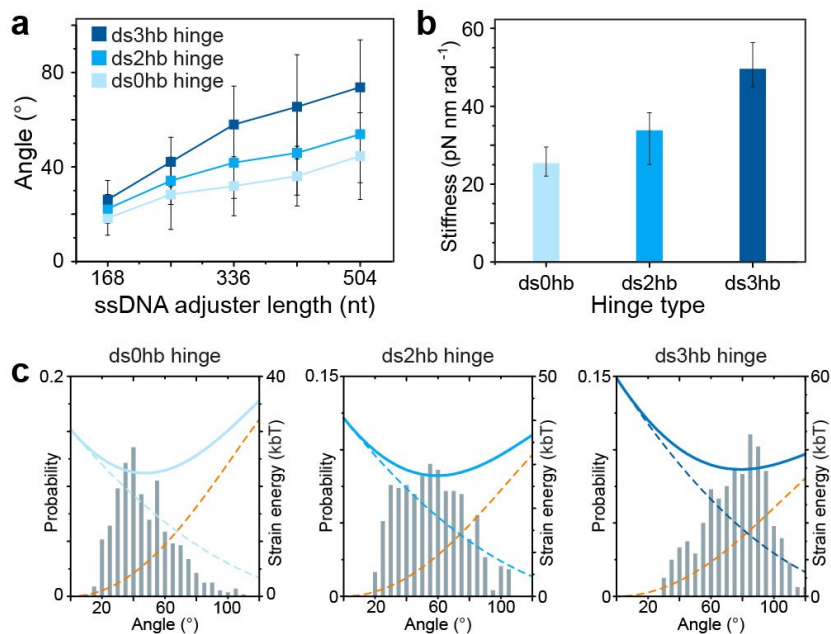


Figure 2-24. Measured average included angles of three different hinge designs.

(a) Measured average included angles of three different hinge designs while varying the length of ssDNA adjuster. Error bars indicate standard deviation. **(b)** Calculated bending stiffness of each hinge design. Error bars indicate maximum and minimum stiffness values. **(c)** Strain energy analysis of the structures with different hinge designs with a 504-nt-long ssDNA adjuster. Gray bars represent experimental included angle distribution, blue-dashed lines are the strain energy stored in the hinge, orange-dashed lines are the entropic energy of ssDNA adjuster, and the blue-solid lines indicate the summation of the two energies, respectively.

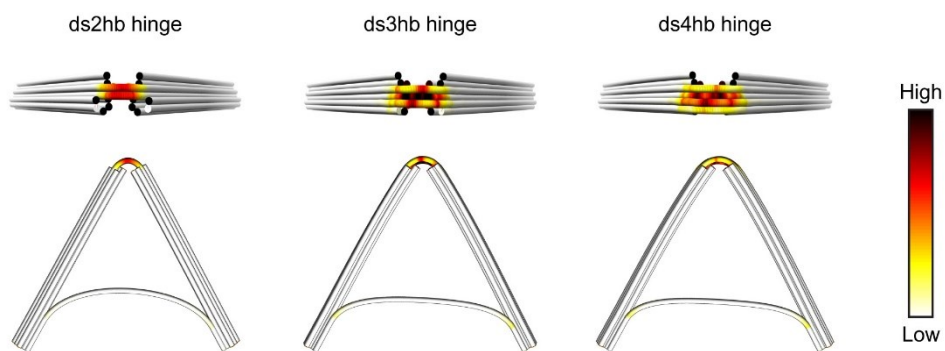


Figure 2-25. Representative CanDo results showing the strain energy concentration at the hinge region. All structures have a 252-nt-long dsDNA adjuster.

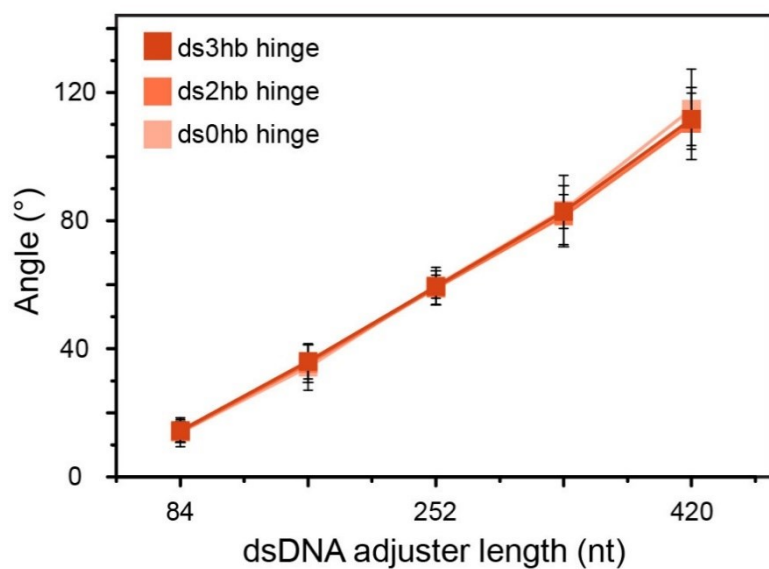


Figure 2-26. Included angle distribution of dsDNA adjuster structures having different adjuster strand length and hinge stiffness. Error bars indicate standard deviation.

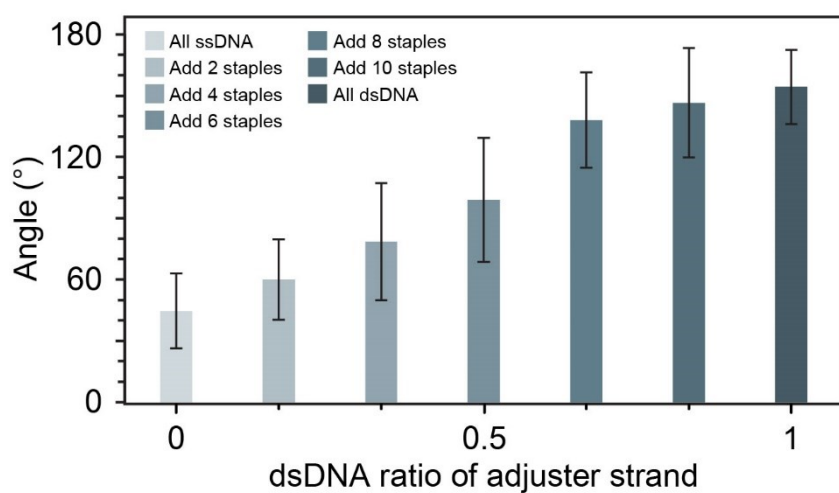


Figure 2-27. Included angle distribution of the ds0hb hinge structures having a different number of adjuster strut staples.

2.7. Conclusion

In summary, our module-based design method provides an efficient way to control the local stiffness of the DNA origami structures, thereby to expand the design space even with a highly limited range of replaced staple sequences. While we demonstrate our design approach here for a honeycomb-latticed bundle structure, the same design principle can be easily applied to other types of structures including planar sheets^{4,50} and bundles with various cross-section shapes and packing rules⁶⁸. By adopting our method, one can test a wide range of geometrical variations in a highly cost-effective manner, to utilize it as a design platform by placing various functional nanoparticles in desired position and orientation. In addition, by changing the adjuster from a scaffold strand to the fuel or functionally modified strand, our design can be directly utilized to the dynamic mechanical component driven by external stimuli while the range of motion can be controlled by the stiffness of the hinge.

Also, CanDo analysis can be used as pre-screening and validation of the shape and feasibility of the structure before fabrication, which leads to significant enhancement of the design efficiency in the scaffolded DNA origami. A deeper understanding of the effect of scaffold route design and corresponding folding pathway of the structure during annealing process in the scaffolded DNA origami⁶⁹ may be useful to enhance the design efficiency and structural quality further.

Chapter 3. Stiffness control by engineered defects

3.1. Introduction

The mechanical stiffness of a DNA nanostructure is generally known to be coupled with its geometric parameters, such as the total number and the cross-sectional shape of crosslinked DNA helices^{25,41}. As a result, it remains challenging to control the stiffness of the structure while preserving its geometry. Nevertheless, its significance has increased recently as the utility of DNA nanostructures have been expanded to kinematic components^{39,70} and substrates for nanomaterials^{28,71}, in which their performance can be modulated by the structural rigidity. While some two-step approaches have been introduced to reinforce self-assembled DNA nanostructures^{72,73}, the demand for a simple and site-specific design method that provides an easy and predictable way of controlling a broad range of structural stiffnesses remains unfulfilled.

Here we propose a rational design method to widely and precisely control the mechanical flexibility of scaffolded DNA origami nanostructures by engineering localized defects that are short ssDNA gaps consisting of up to 5 nucleotides (nt), while maintaining their overall structural integrity and geometric characteristics. The feasibility of our design method was demonstrated by building DNA origami constructs with different cross-sectional shapes where modular and individually tunable defects could reduce their bending stiffness by up to 70% using their length

Figures and texts in this chapter were reprinted with permission from Lee, C. *et al.*, Tailoring the Mechanical Stiffness of DNA Nanostructures Using Engineered Defects. *ACS Nano*. Copyright 2019 American Chemical Society. DOI: 10.1021/acsnano.9b03770.

and density as the design parameters. We further developed a computational analysis platform predicting the bending stiffness of a defect-engineered DNA nanostructure quickly during the design process. Since the proposed defect-engineering framework is highly scalable and readily applicable for conventional shape design methods in scaffolded DNA origami, it offers a versatile way of designing various DNA constructs with required mechanical stiffness in a desired shape for a targeted function.

3.2. Design method

In a typical M13mp18-based scaffolded DNA origami⁴, around 150 to 250 DNA single-stranded breaks (nicks) naturally exist over the structure where two ends of the neighboring oligonucleotides (staples) meet (Fig. 3-1a). We have paid attention to them as a mechanically weak design motif to control the stiffness of DNA origami nanostructures without altering the geometrical features. However, their softening effect has shown to be not significantly high except for torsion⁷⁴, which seems not sufficient for a broad range of mechanical control.

Hence, we develop the concept of engineered defects defined as short ssDNA gaps each of which consists of one to five bases (approximately 0.3 to 1.7 nm long). They can be easily formed by replacing staples at nick sites in the reference design with shorter ones before self-assembly (Fig. 3-1b). As ssDNA is known to be much more flexible than dsDNA⁷⁵, the rigidity of defect-inserted sections and thereby the overall structural stiffness of DNA constructs can be noticeably reduced. Note that creating an engineered defect of various lengths at a nick site does not affect the sequence of the adjacent staples. Therefore, completely modular and localized control of the mechanical stiffness of DNA nanostructures is possible with base-pair-level precision. While short ssDNAs have been partly used to relax some distortions at the vertices of the polyhedral constructs²⁴, they have not been utilized yet as mechanical design components to modulate the stiffness of DNA nanostructures.

We used two design parameters, the gap length (the number of ssDNA bases) and the gap density (the ratio of the number of inserted gaps to the total number of nicks), to control the mechanical stiffness of DNA nanostructures systematically.

Two cross-section designs, one with four and another with six DNA helices (denoted as 4HB and 6HB, respectively), were selected as they had sufficiently long contour lengths (580 nm in 4HB and 390 nm in 6HB) for analysis of their bending stiffness in monomer scale as well as the stiffness values of these designs have been experimentally verified^{57,76,77} (Figs. 3-2 and 3-3).

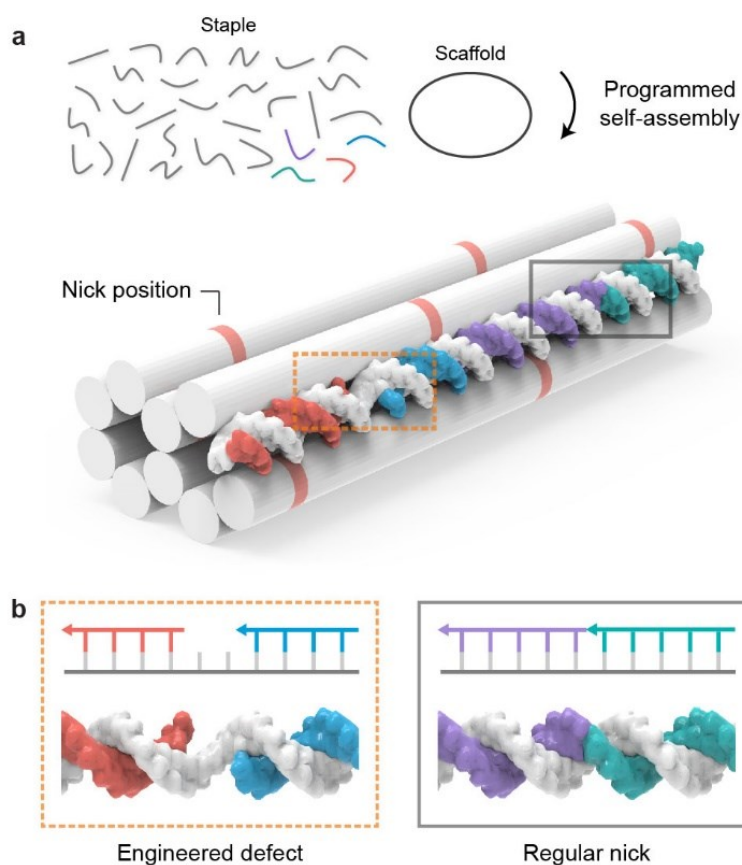


Figure 3-1. Schematic illustration of defect-engineering of DNA nanostructures.

(a) A typical DNA origami structure consisting of a long circular scaffold and hundreds of staple strands with unique sequences complementary to those in their target binding locations. In DNA origami structures, multiple nicks exist where two ends of the neighboring staples meet (highlighted in red in cylindrical representation).

(b) Close-up views of an engineered defect and a regular nick. An engineered defect can be created at any nick location by using a staple shorter than the regular one in the self-assembly process. The arrowheads indicate the 3' ends of the staples.

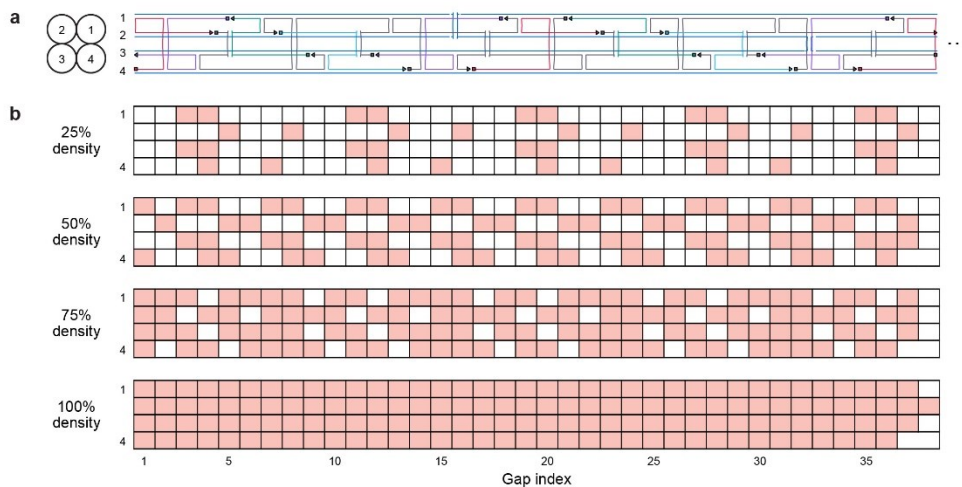


Figure 3-2. 4HB gap design. (a) Repetitive scaffold and staple route constituting 4HB with square-lattice packing. Triangles and rectangles indicate the 5' and 3' end of staple DNAs, respectively. **(b)** Schematics that colored boxes show the positions where nicks located at the corresponding indices were changed to ssDNA gaps with programmed length.

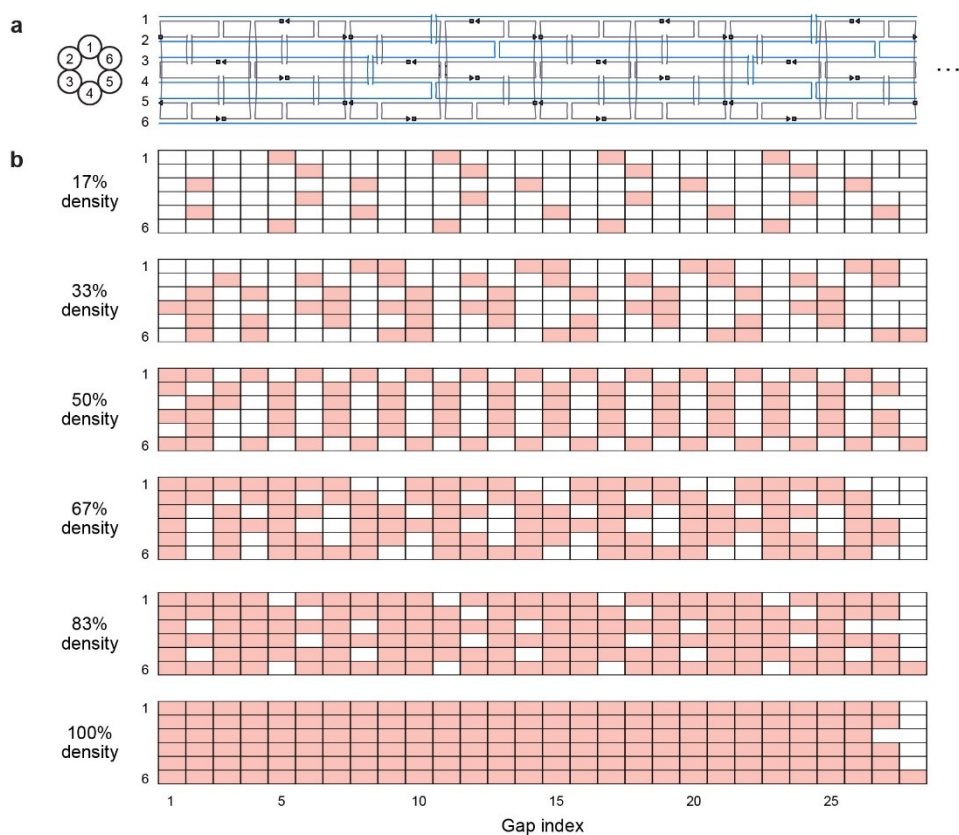


Figure 3-3. 6HB gap design. (a) Repetitive scaffold and staple route constituting 6HB with honeycomb-lattice packing. Triangles and rectangles indicate the 5' and 3' end of staple DNAs, respectively. **(b)** Schematics that colored boxes show the positions where nicks located at the corresponding indices were changed to ssDNA gaps with programmed length. Seven nicks located at the both ends of the bundle were omitted in the diagram since they were not changed to ssDNA gaps throughout the gap density variations.

3.3. Experimental results

First of all, the effect of two gap design parameters was demonstrated using the 4HB and 6HB design. In 4HB design, the gap length was varied while maintaining the maximum gap density, while the density of 5-nt-long gaps was varied in 6HB design. (Fig. 3-4). In both cases, higher fluctuations of the monomer contours were clearly visible for longer gap lengths and higher gap densities.

We analyzed the bending stiffness of DNA bundles quantitatively by calculating the persistence length of individual monomers from their thermodynamically equilibrated contours in 2D, measured by AFM^{37,78}. In brief, the individual well-folded monomer structures were converted into binary images to be thinned and skeletonized to obtain their contours. After that, parametric spline was used to fit the contour of each individual structure. The persistence length was measured with characteristic points of the fitting spline from every well-folded structures using a modified version of open-source software tool Easyworm⁷⁹ (Fig. 3-5b). Using WLC model, the mean-square end-to-end distance ($\langle R^2 \rangle$) in two dimensions as a function of the distance along the contour (l_c) can be expressed as

$$\langle R^2 \rangle = 4L_p l_c \left[1 - 2L_p / l_c \left(1 - \exp(-l_c / 2L_p) \right) \right] \quad (9)$$

where L_p is the persistence length. Typically, the correlation coefficient of the data fitting is above 0.99 for each case. Standard deviation of the persistence length was calculated by a bootstrap method with a subset of 500 randomly chosen contours with replacement and 10,000 times of repeating process.

The calculated bending persistence lengths of the non-modified 4HB (4HB-Ref) and 6HB (6HB-Ref) designs were 1,000 and 2,030 nm, respectively, which are generally within the range reported in the previous studies^{25,57,76,77} (Fig. 3-5). It was found that the length of individual spline segments (defined as the number of pixels per segment) should be determined carefully to avoid any inaccuracy in the fitting of the mean-square end-to-end distance curves (Fig. 3-6). Therefore, the kurtosis analysis was conducted in order to obtain the smallest value for each cross-section designs which satisfies theoretical kurtosis value of 3 when the contours were within the 2D equilibrium states⁸⁰ (Figs. 3-7 and 3-8). It was also evaluated whether the monomer length and the imaging resolution were suitable for the calculation of the bending persistence length (Figs. 3-9 and 3-10). It can be noted that the estimated values of the bending persistence length can vary depending on the measurement method even for the same geometry, because each method possesses a different sample preparation procedure and the resolution limit^{38,70}. To avoid incomplete staple binding during the self-assembly process⁸¹, all nicks (150 in 4HB and 169 in 6HB) in our design were located at least six bases away from the adjacent Holliday junctions (crossovers), and at least three base pairs were maintained between the gap and the crossover when a nick was changed to an ssDNA gap.

To further quantify the range of stiffness control, a comprehensive set of these two design parameters was tested for both 4HB and 6HB designs (Figs. 3-11 to 3-16 and Table 3-1). As a result, a wide range of control for the bending stiffness could be achieved with the proposed design method using engineered defects. The maximum softening effect in bending turned out to be 70% in 4HB and 67.5% in 6HB when 5-nt-long gaps with full density were used. Note that the number of gaps per helix and the interval between gaps were maintained appropriately in order to

prevent the stiffness anisotropy in both radial and longitudinal directions of the bundles (Figs. 3-2 and 3-3). When gaps were distributed anisotropically along the longitudinal direction in the 6HB design, the bending stiffness decreased more irregularly with the gap density (Fig. 3-17).

In terms of the folding yield, defect-engineered variations tended to maintain a clear monomer band in gel electrophoresis, but their band intensities were diminished when a high density ($> 75\%$) of 5-nt long gaps was used (Figs. 3-18 and 3-19). The structural folding yield, defined as the ratio of the number of well-folded monomers to the total number of monomers, was ranging from 75.7% to 94.5% for all 4HB and 6HB designs with engineered defects (Fig. 3-20 and Table 3-2).

Reducing the density of crossovers connecting adjacent dsDNA helices might be another approach to lowering the stiffness of DNA nanostructures. However, a former report²⁰ claimed that increasing the interval between inter-helix crossovers would result in higher thermal fluctuation of the structure, rendering the structure less stable in terms of retaining its cross-sectional shape. We tested this phenomenon by designing a 6HB in which half of the region was filled with 42-nt-interval crossovers (two times longer than the typical crossover connection) and discovered that there was a notable collapse of cross-sections. Further, the bending stiffness of this design was calculated as 2090 nm, which was slightly higher than that of the 6HB-Ref design (Fig. 3-21). This implies that changing the crossover density is in fact not as effective as creating the engineered defects for the flexibility control of DNA bundles. Intentional staple omission can be an alternative technique to soften DNA nanostructures, which was shown to be effective in case where a local region of the structure was to be adjusted^{43,82}. However, this method turned out to be problematic when used to reduce the overall stiffness of the entire structure. Our

6HB structures where 8.2% and 16.4% of constituting staples were eliminated could not be constructed properly (Fig. 3-22) even though it was reported that structures with thicker cross-sections could endure this effect relatively well⁸³.

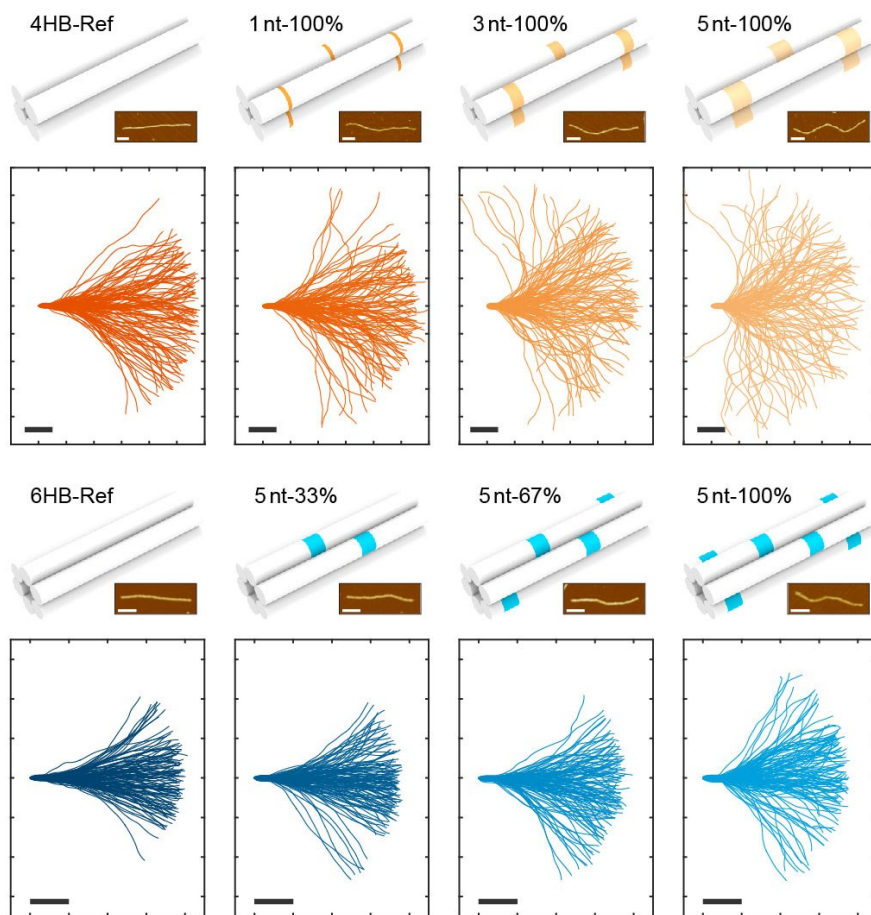


Figure 3-4. Design parameters for defect-engineered DNA origami bundles and a computational model to predict their flexibility. Schematic illustration of two design parameters for engineered gaps, AFM images of a sample monomer, and the contours of 120 representative monomers for each design case. Initial tangents of the contours are aligned horizontally (scale bars and ticks: 100 nm).

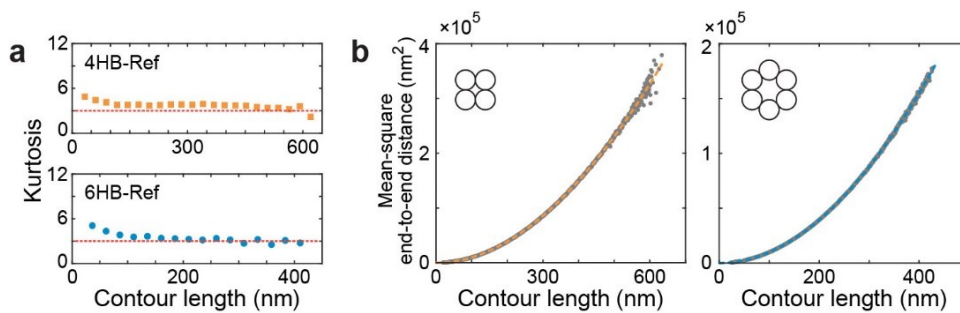


Figure 3-5. Calculation of persistence length from monomer contours. (a) Kurtosis of 4HB-Ref and the 6HB-Ref contours. It converged in both structures to 3 which is the value corresponding to the theoretical 2D equilibrium state. **(b)** Mean-square end-to-end distance of representative 4HB-Ref and 6HB-Ref contours.

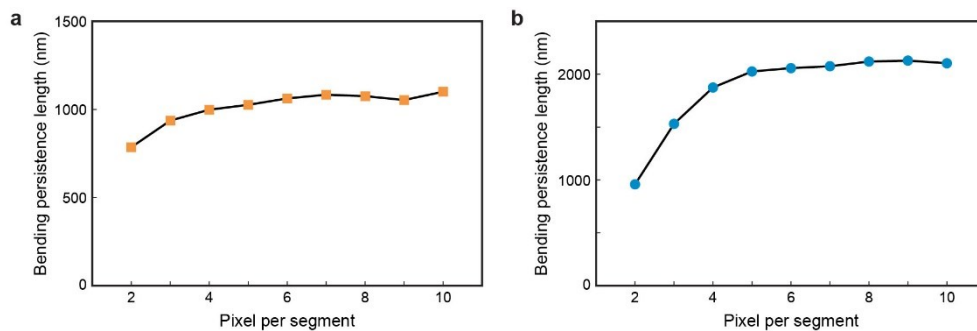


Figure 3-6. Bending persistence length measurement with different unit segment length. Bending persistence length of (a) 4HB-Ref and (b) 6HB-Ref design. Note that length of a unit segment is proportional to the value of pixel per segment. Resolution of a pixel is approximately 4.9 nm/px.

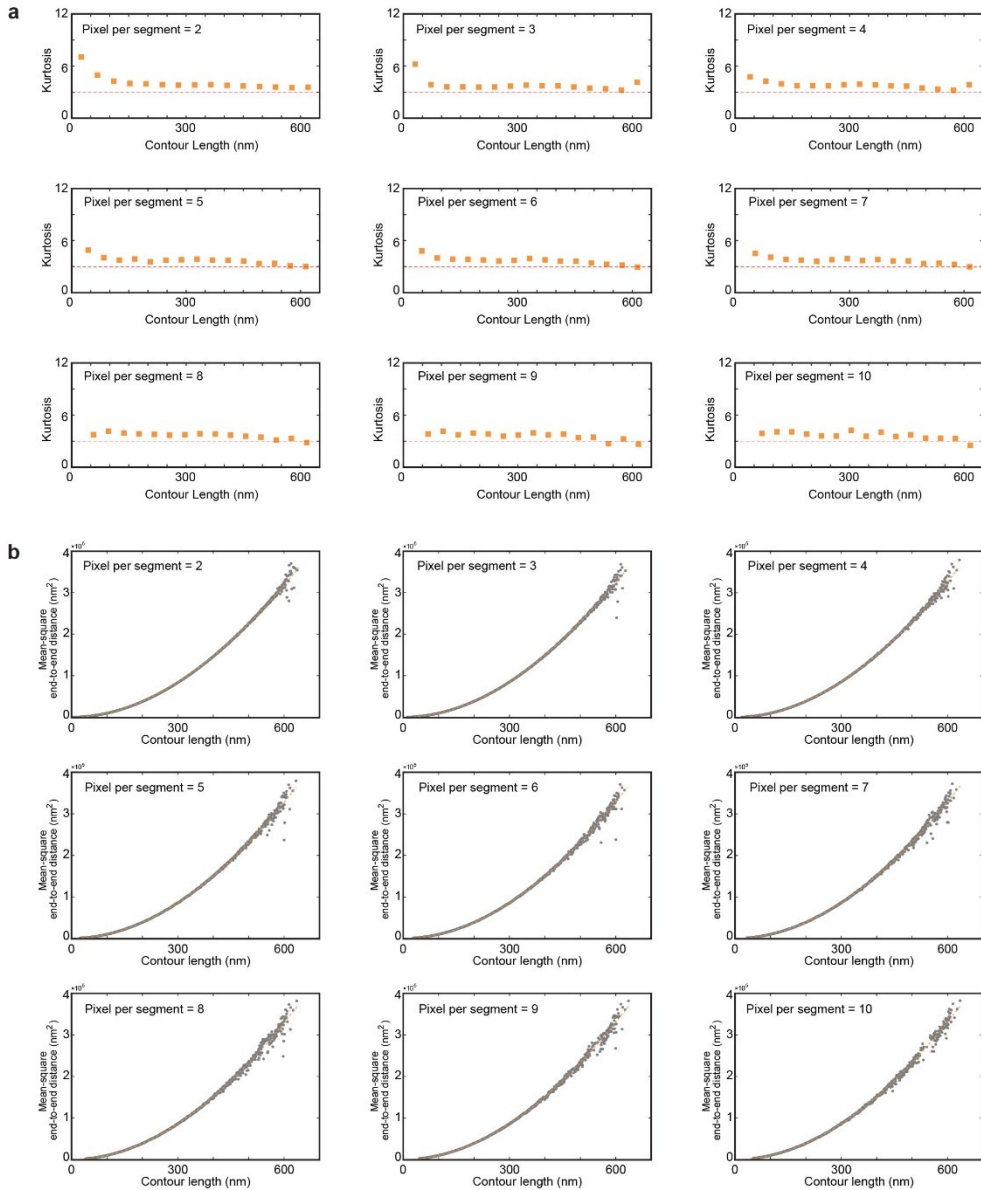


Figure 3-7. Parameter analysis on 4HB-Ref design. (a) Kurtosis analysis and (b) end-to-end distance fitting curves. Calculated bending persistence length in each case was shown in Fig. 3-6a. Pixel per segment value was chosen as 4 in the manuscript.

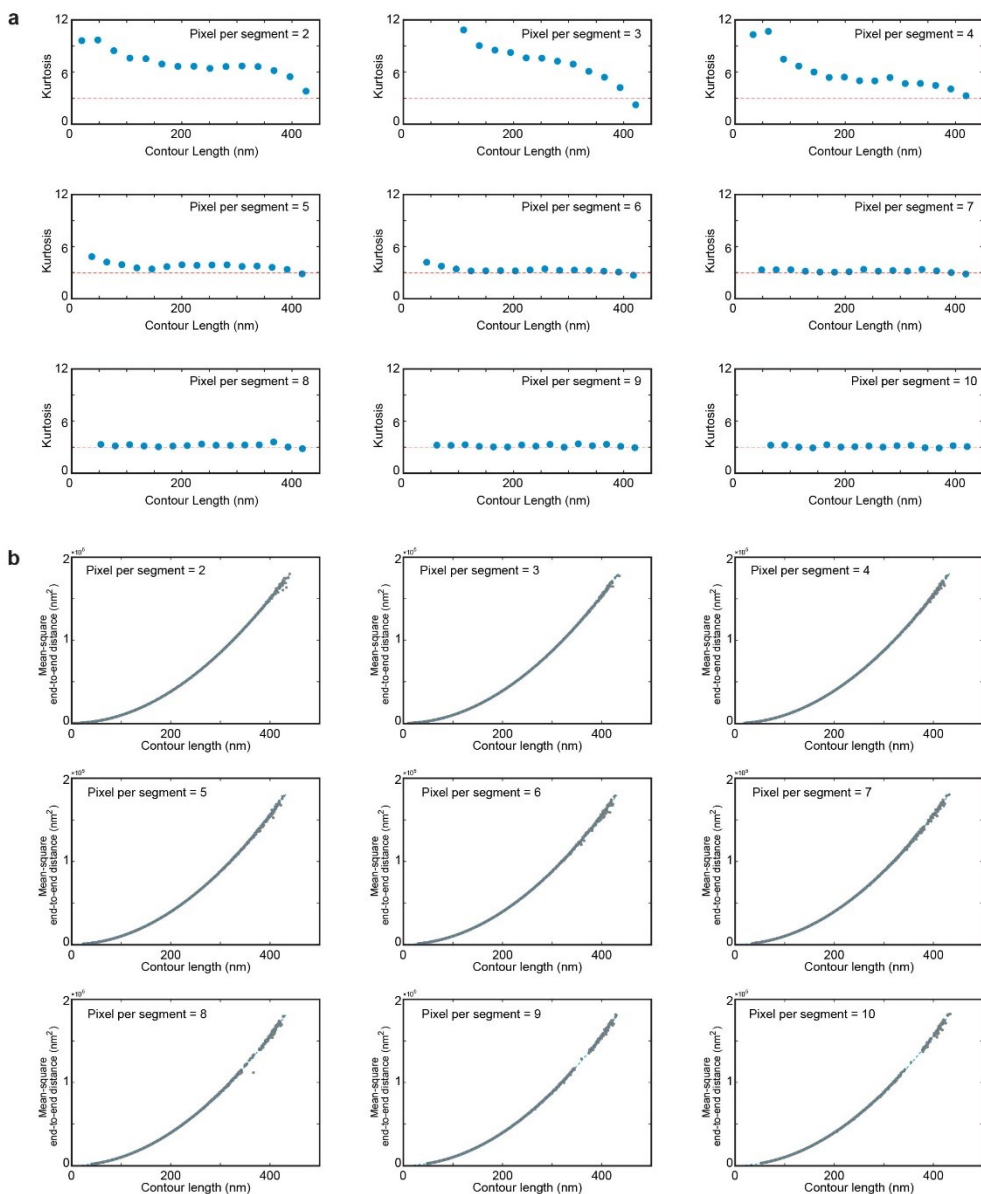


Figure 3-8. Parameter analysis on 6HB-Ref design. (a) Kurtosis analysis and (b) end-to-end distance fitting curves. Calculated bending persistence length in each case was shown in Fig. 3-6b. Pixel per segment value was chosen as 5 in the manuscript.

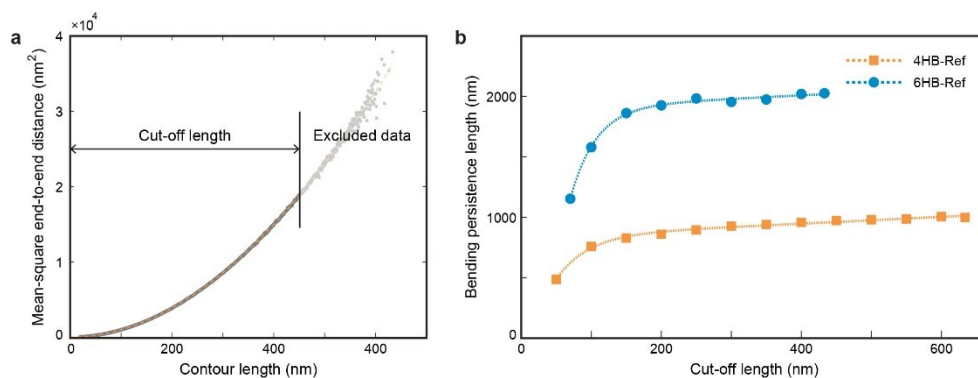


Figure 3-9. Calculation of bending persistence length while varying the range of contour length. (a) Definition of the cut-off length. Data within cut-off contour length was used to calculate the bending persistence length. **(b)** A graph showing that calculated values of bending persistence length were converged within monomer length range both in 4HB-Ref and 6HB-Ref design.

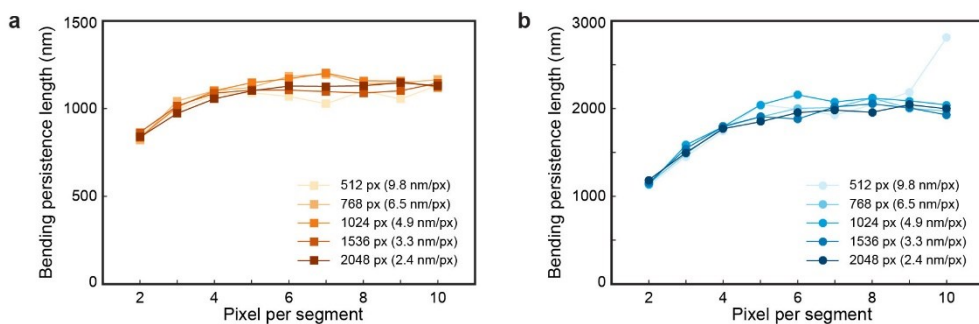


Figure 3-10. Calculation of bending persistence length while varying the resolution of the images. (a) Results of 4HB-Ref design using 100 monomers and **(b)** 6HB-Ref design using 140 monomers. From the analysis, 1024 px resolution was used in all of the cases.

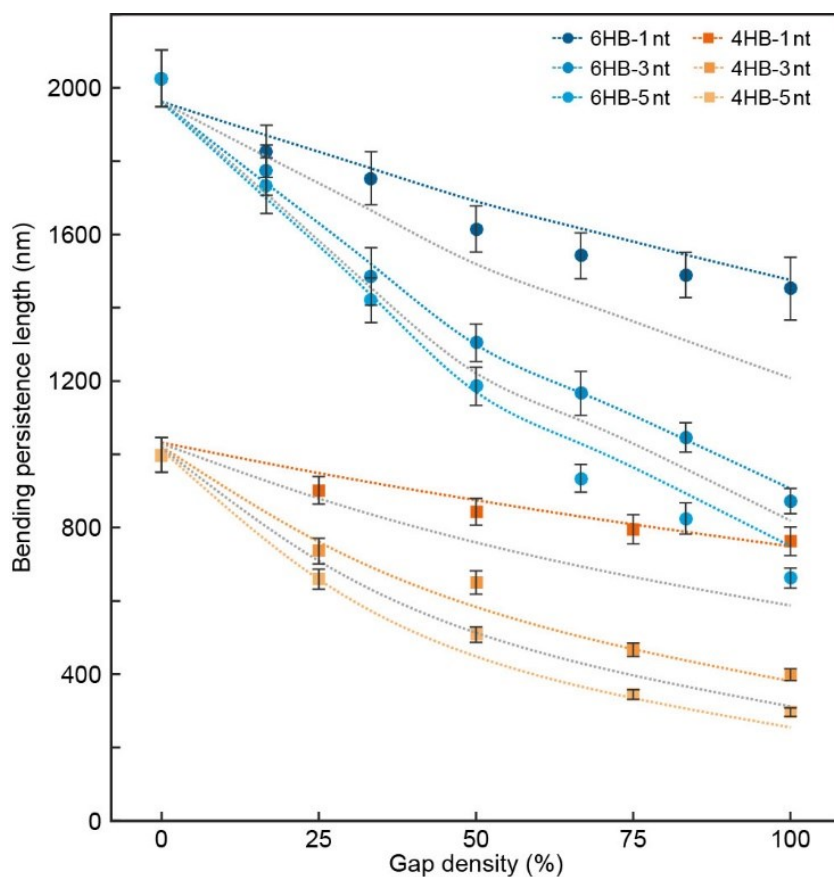


Figure 3-11. Measured bending persistence lengths of the 4HB and 6HB structures designed with the systematically varied length and density of gaps. Refer to Figs. 3-12 to 3-16 for the AFM images and the contour distribution of all cases. The dotted lines indicate the spline-fitted curves of computationally estimated values. The grey lines correspond to 2-nt and 4-nt long gap designs. Error bars indicate the standard deviation of experimental results.

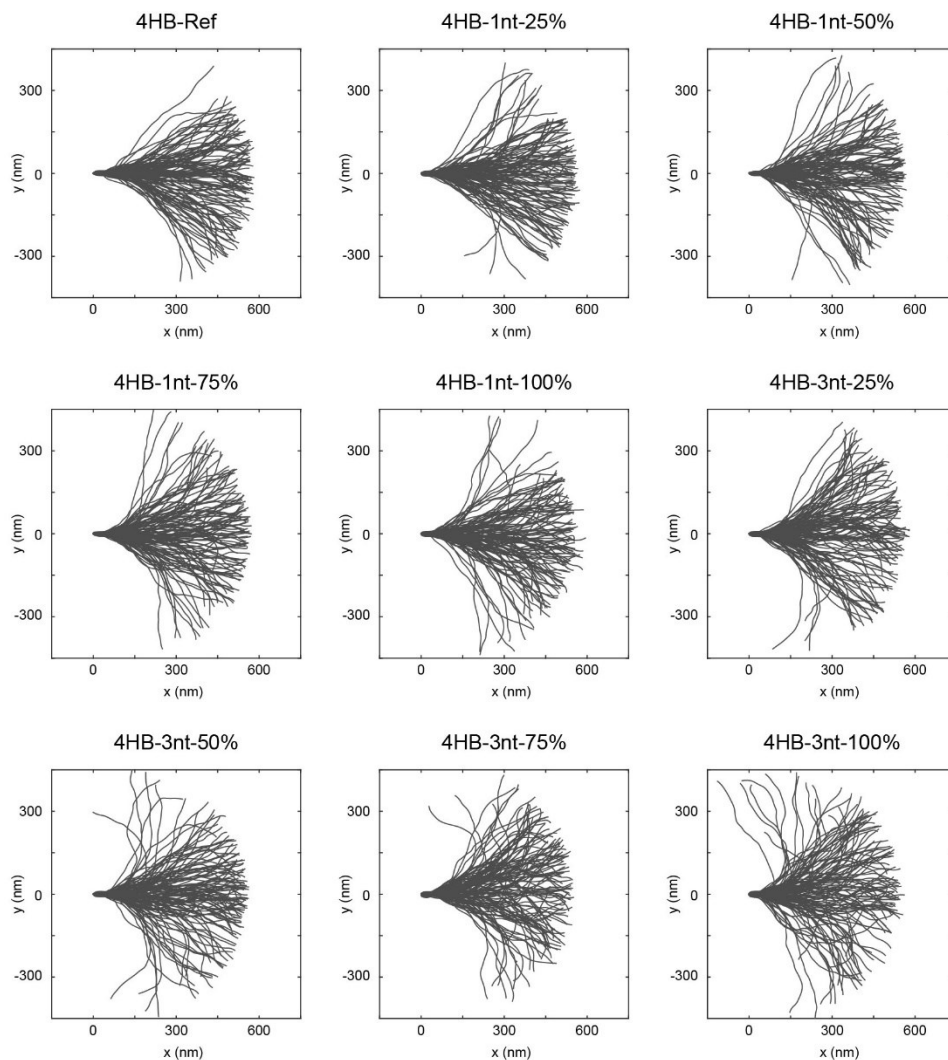


Figure 3-12. Experimental characterization of 4HB with 1 and 3-nt gap variations. Aligned contour distribution of 120 representative monomers measured from AFM.

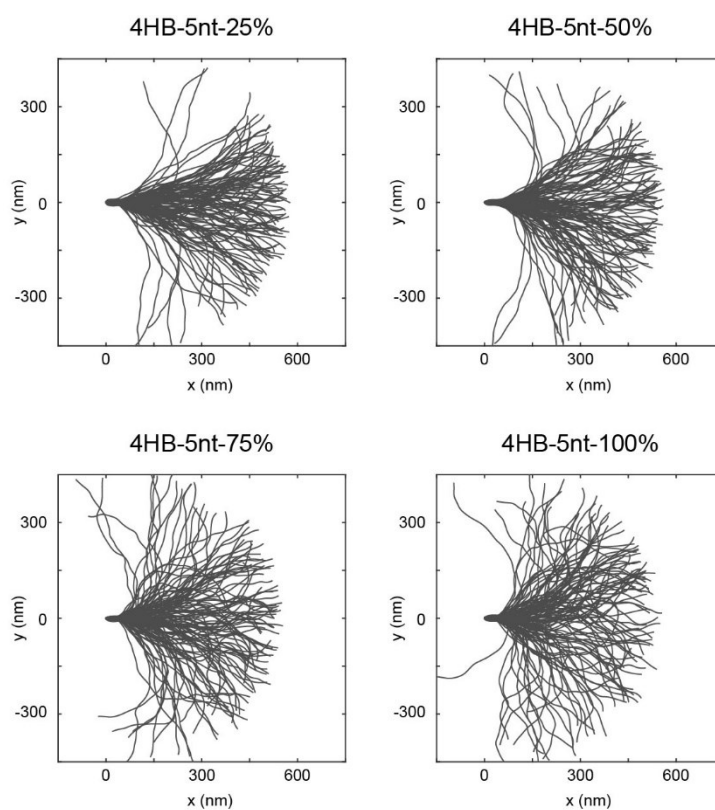


Figure 3-13. Experimental characterization of 4HB with 5-nt gap variations.

Aligned contour distribution of 120 representative monomers measured from AFM.

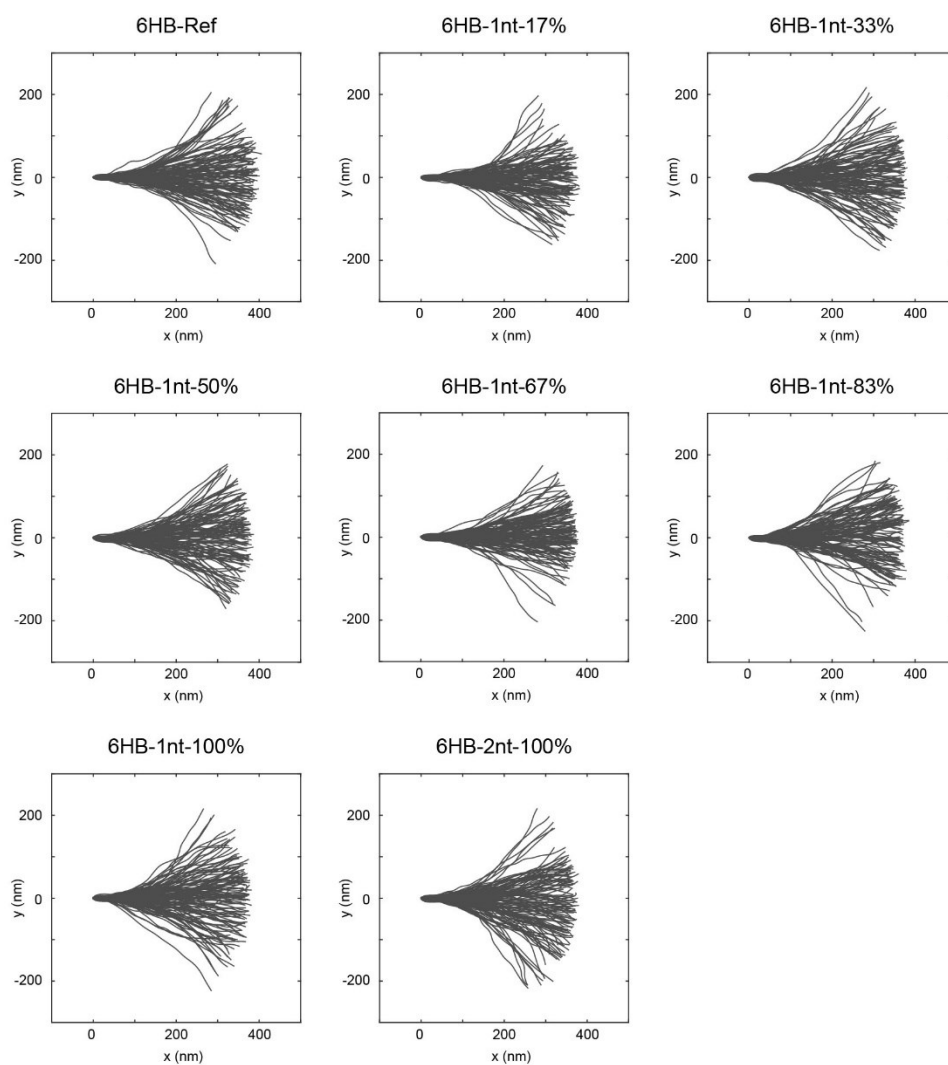


Figure 3-14. Experimental characterization of 6HB with 1 and 2-nt gap variations. Aligned contour distribution of 120 representative monomers measured from AFM.

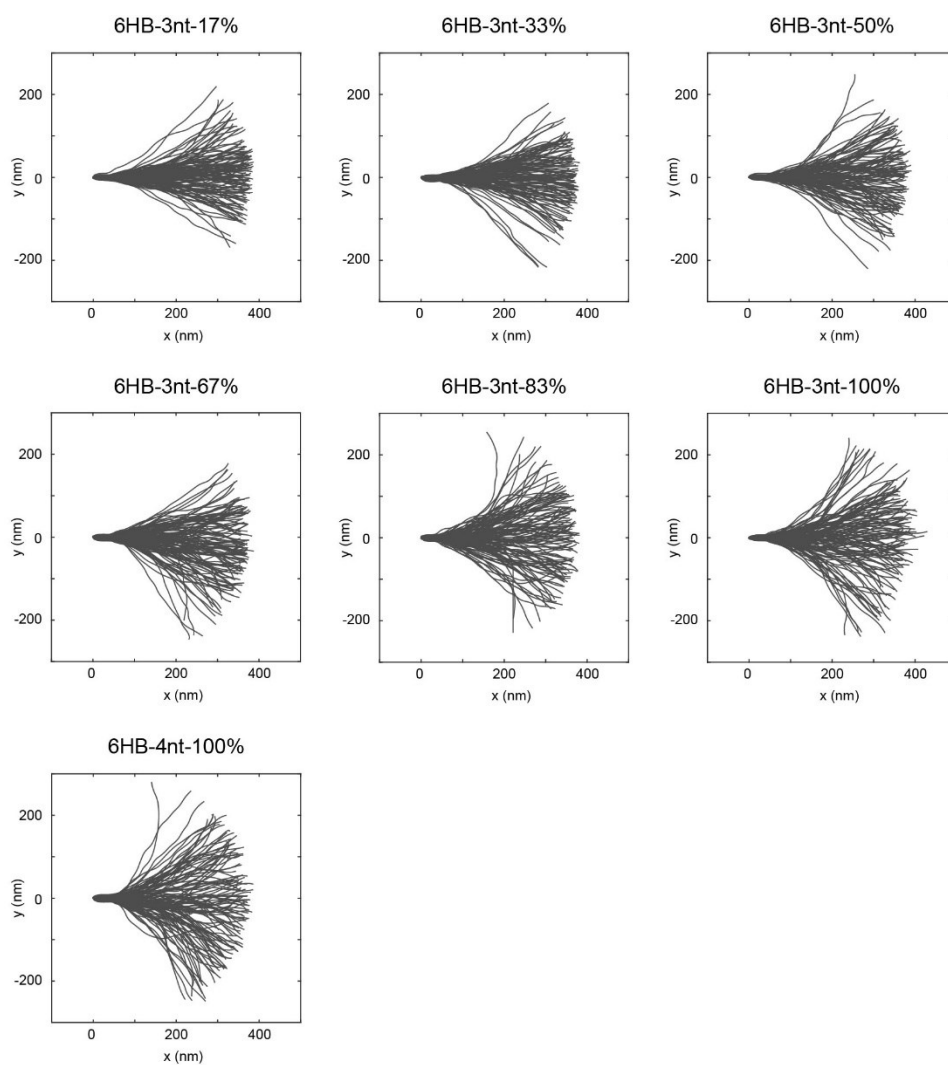


Figure 3-15. Experimental characterization of 6HB with 3 and 4-nt gap variations. Aligned contour distribution of 120 representative monomers measured from AFM.

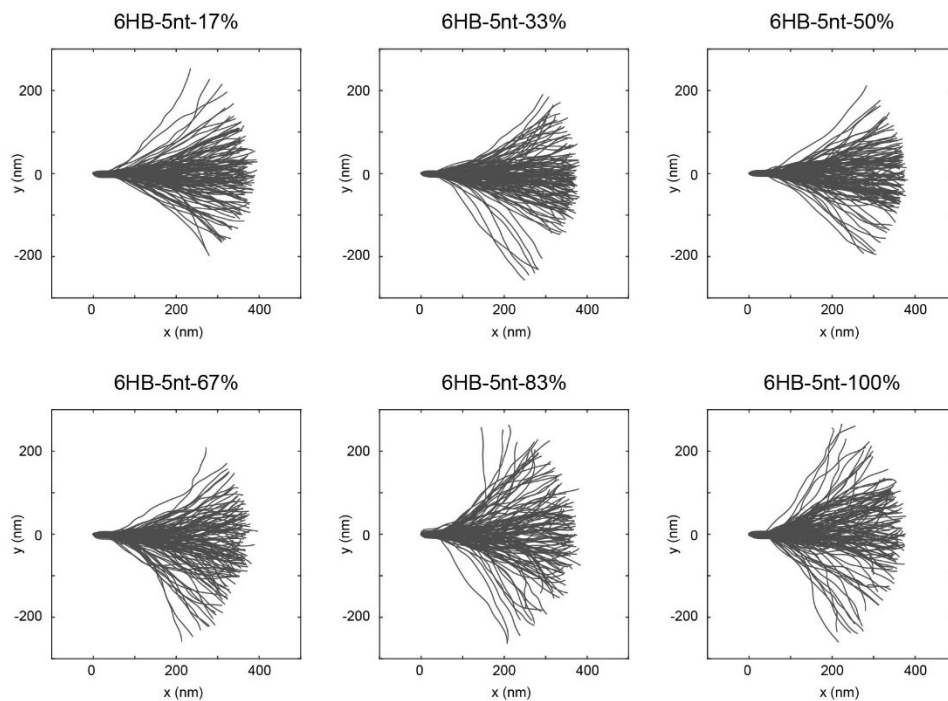


Figure 3-16. Experimental characterization of 6HB with 5-nt gap variations.

Aligned contour distribution of 120 representative monomers measured from AFM.

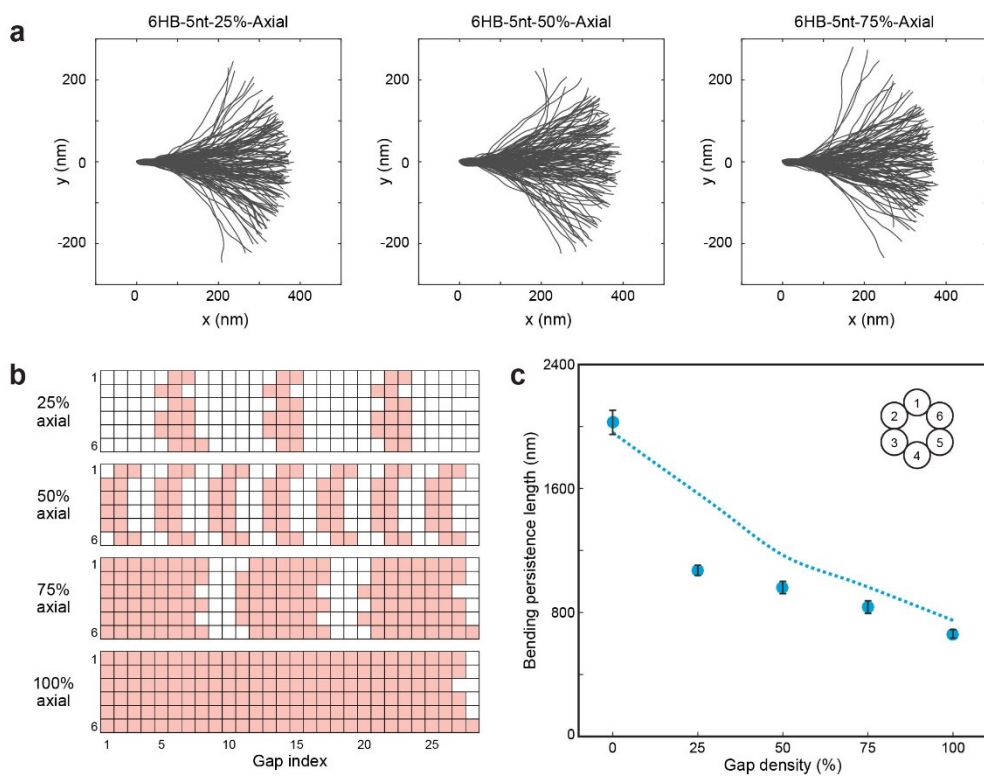


Figure 3-17. Experimental characterization of 6HB with 5-nt anisotropically distributed gaps. (a) Aligned contour distribution of 120 representative monomers measured from AFM. (b) Schematic illustration of anisotropic gap distributions in a longitudinal direction. (c) Experimentally measured values of bending persistence length. Blue dotted line indicates the spline-fitted FE simulation result. Error bars indicate the standard deviation of experimental results.

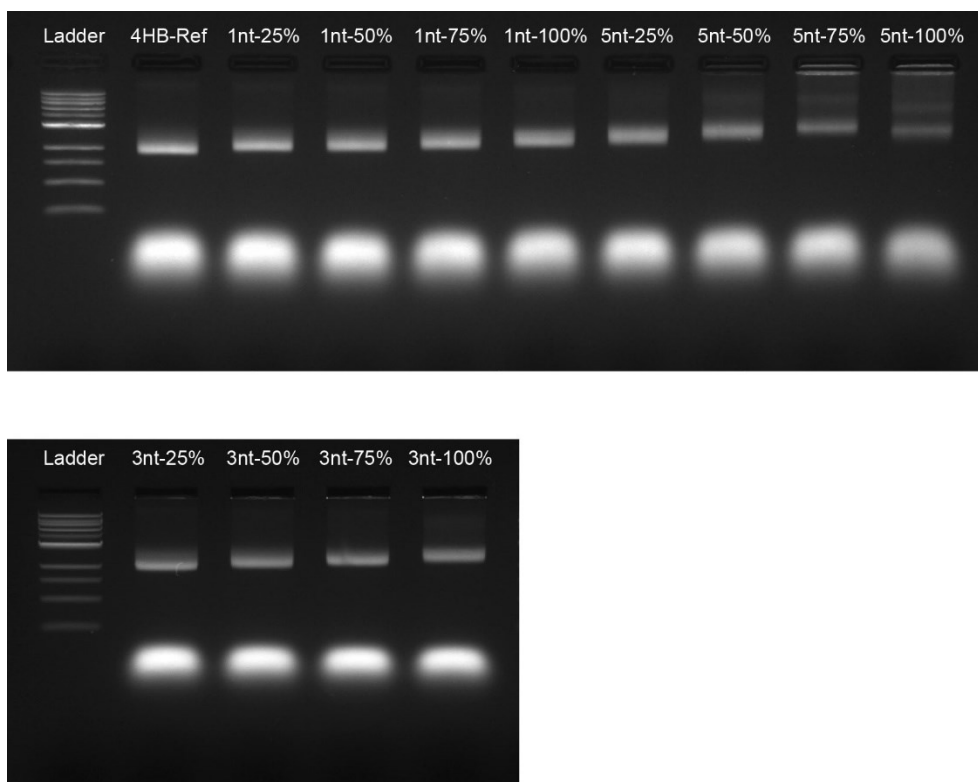


Figure 3-18. Gel electrophoresis result of 4HB designs.

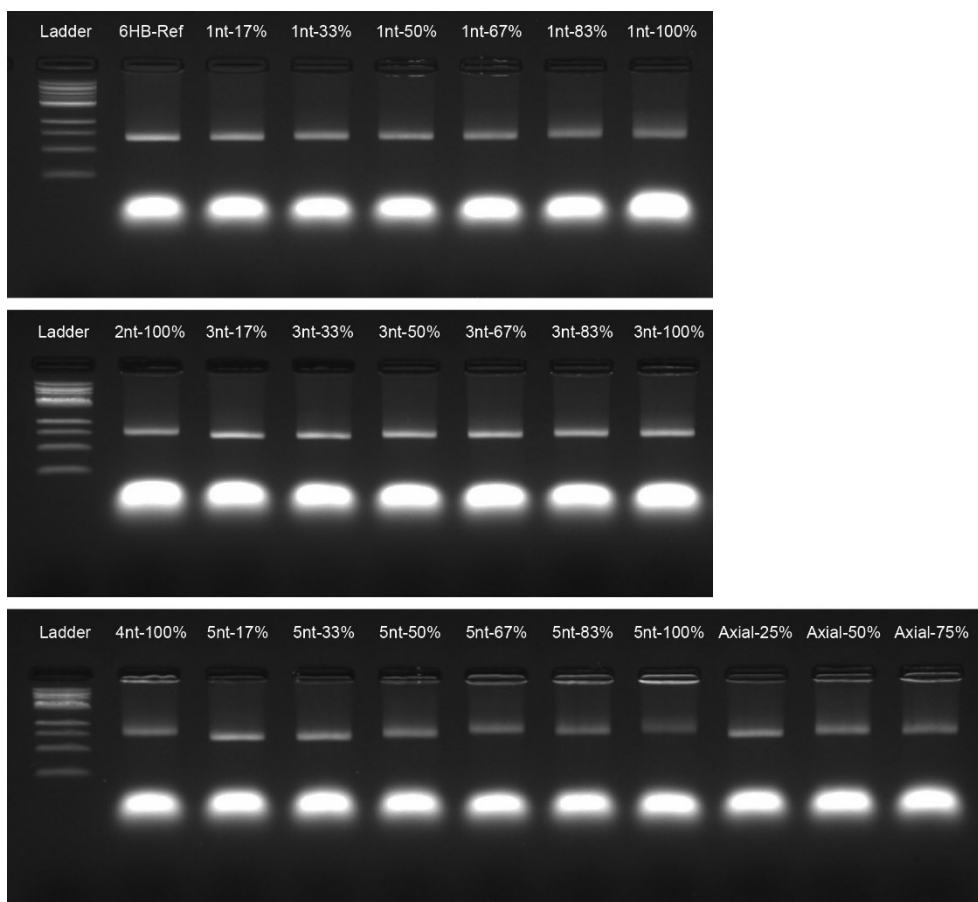


Figure 3-19. Gel electrophoresis result of 6HB designs.

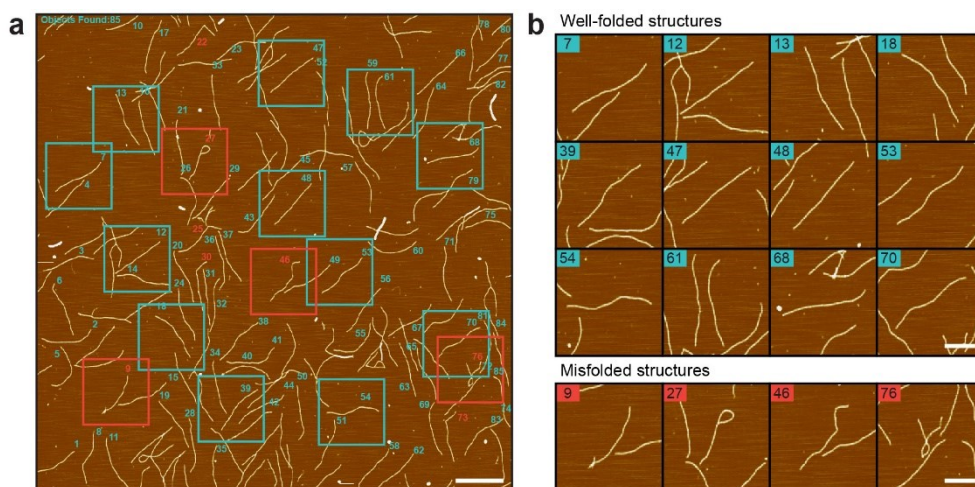


Figure 3-20. Structural folding yield analysis. (a) AFM image of the 4HB-Ref design showing the process of structural folding yield calculation. After the automated monomer-selection process, well-folded and misfolded monomer structures were classified manually. Result of all design variations were summarized in Table 3-2. Scale bar: 500 nm **(b)** Representative monomer images of well-folded and misfolded monomer structures. Scale bars: 200 nm.

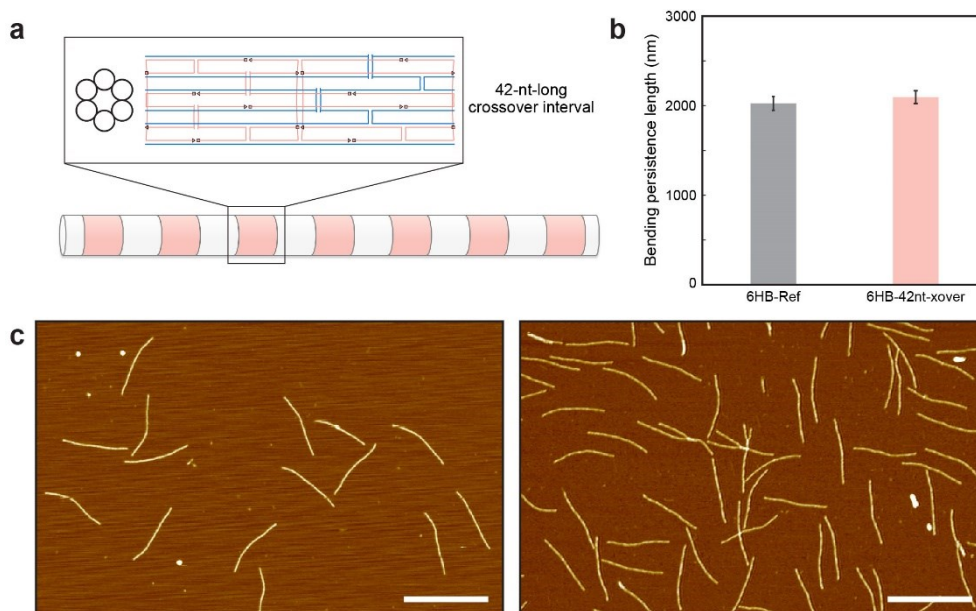


Figure 3-21. 6HB bundle with 42-nt-interval crossover modification at half of the region. (a) Schematic illustration showing the modified regions and staple design therein. **(b)** Bending persistence length of the modified case was similar to the reference design. **(c)** Representative AFM images of the reference and 42-nt-long crossover design, respectively. Scale bars: 300 nm.

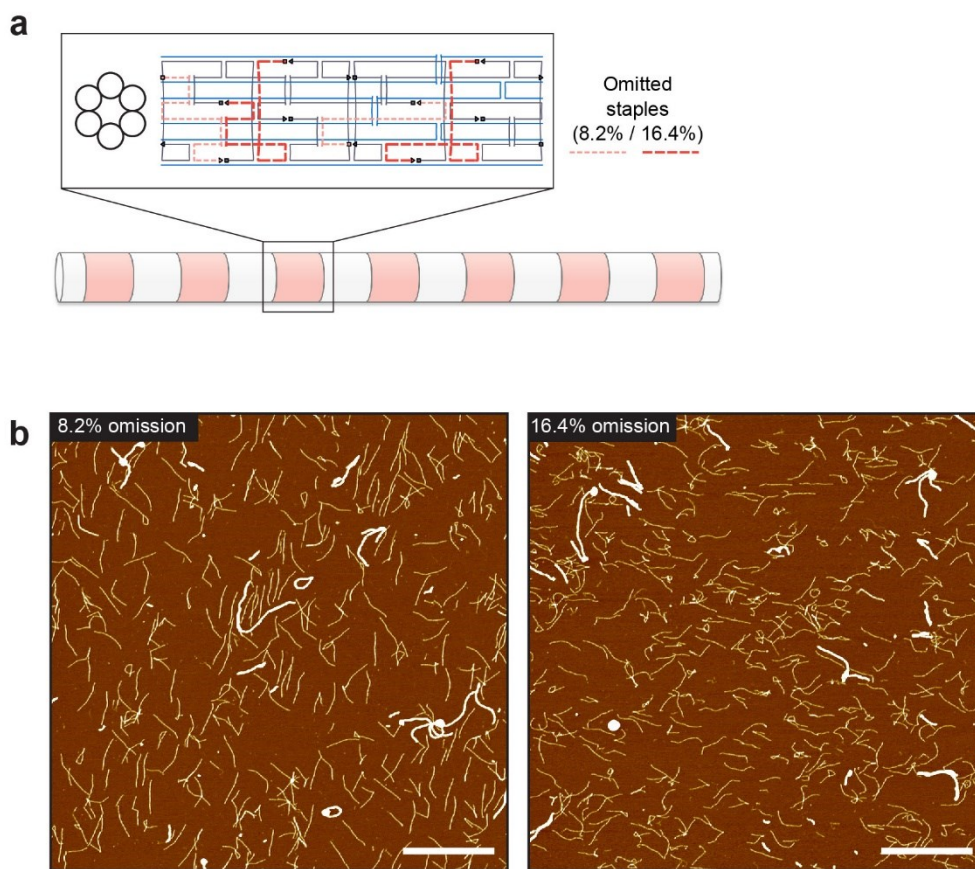


Figure. 3-22. 6HB bundle with staple omission at half of the region. (a)

Schematic illustration showing the modified regions and representative positions of omitted staples therein. Note that positions of omitted staples were changed along the regions to distribute the defect locations. Two light red-colored staples were removed in 8.2% omission design, and another two darker red staples were additionally removed in 16.4% omission design. **(b)** AFM image of the two cases.

Scale bars: 1 μm .

Design	Average bending persistence length (nm)	Std. deviation of bending persistence length (nm)	Number of samples (N)
4HB-Ref	1000	50	634
4HB-1nt-25%	900	40	396
4HB-1nt-50%	840	40	453
4HB-1nt-75%	800	40	619
4HB-1nt-100%	760	40	399
4HB-3nt-25%	740	40	506
4HB-3nt-50%	650	30	563
4HB-3nt-75%	470	20	589
4HB-3nt-100%	400	20	365
4HB-5nt-25%	660	30	231
4HB-5nt-50%	510	20	338
4HB-5nt-75%	340	10	375
4HB-5nt-100%	300	10	660
6HB-Ref	2030	80	682
6HB-1nt-17%	1830	70	702
6HB-1nt-33%	1750	70	504
6HB-1nt-50%	1610	60	384
6HB-1nt-67%	1540	60	647
6HB-1nt-83%	1490	60	643
6HB-1nt-100%	1450	90	672
6HB-2nt-100%	1040	40	627
6HB-3nt-17%	1780	70	442
6HB-3nt-33%	1490	80	473
6HB-3nt-50%	1300	50	502
6HB-3nt-67%	1170	60	553
6HB-3nt-83%	1050	40	401
6HB-3nt-100%	870	30	438
6HB-4nt-100%	750	30	418
6HB-5nt-17%	1730	80	750
6HB-5nt-33%	1420	60	394
6HB-5nt-50%	1190	50	665
6HB-5nt-67%	930	40	806
6HB-5nt-83%	820	40	1073
6HB-5nt-100%	660	30	779
6HB-5nt-25%-Axial	1190	40	233
6HB-5nt-50%-Axial	1020	50	574
6HB-5nt-75%-Axial	900	40	600
10HB-Ref	5430	280	929
10HB-5nt-20%	4660	220	904
10HB-5nt-40%	3720	170	712
10HB-5nt-60%	3280	150	520
10HB-5nt-80%	2470	130	872
10HB-5nt-100%	2080	110	988

Table. 3-1. Summary of bending persistence length measurement.

Design	Number of total monomers	Number of well-folded structures	Structural folding yield (%)
4HB-Ref	698	760	91.8
4HB-1nt-25%	420	397	94.5
4HB-1nt-50%	514	470	91.4
4HB-1nt-75%	730	668	91.5
4HB-1nt-100%	494	444	89.9
4HB-3nt-25%	607	541	89.1
4HB-3nt-50%	695	594	85.5
4HB-3nt-75%	694	616	88.8
4HB-3nt-100%	415	379	91.3
4HB-5nt-25%	333	304	91.3
4HB-5nt-50%	418	362	86.6
4HB-5nt-75%	449	398	88.6
4HB-5nt-100%	798	720	90.2
6HB-Ref	718	627	87.3
6HB-1nt-17%	531	474	89.3
6HB-1nt-33%	510	454	89.0
6HB-1nt-50%	525	452	86.1
6HB-1nt-67%	611	531	86.9
6HB-1nt-83%	543	490	90.2
6HB-1nt-100%	565	520	92.0
6HB-1nt-200%	483	428	88.6
6HB-3nt-17%	459	392	85.4
6HB-3nt-33%	566	486	85.9
6HB-3nt-50%	601	536	89.2
6HB-3nt-67%	616	522	84.7
6HB-3nt-83%	731	633	86.6
6HB-3nt-100%	647	531	82.1
6HB-4nt-100%	570	485	85.1
6HB-5nt-17%	541	496	91.7
6HB-5nt-33%	584	508	87.0
6HB-5nt-50%	609	538	88.3
6HB-5nt-67%	489	370	75.7
6HB-5nt-83%	600	515	85.8
6HB-5nt-100%	494	406	82.2
6HB-5nt-25%-Axial	606	491	81.0
6HB-5nt-50%-Axial	645	542	84.0
6HB-5nt-75%-Axial	592	504	85.1
10HB-Ref	999	939	94.0
10HB-5nt-20%	1109	976	88.0
10HB-5nt-40%	873	748	85.7
10HB-5nt-60%	708	577	81.5
10HB-5nt-80%	1101	883	80.2
10HB-5nt-100%	852	617	72.4

Table 3-2. Structural folding yield result. At least five AFM images were used to analyze the structural folding yield of each case.

3.4. Computational model and validation

As the stiffness control via engineered defects were proven to be highly effective in our 4HB and 6HB designs, we developed a computational model to predict the bending stiffness of defect-engineered DNA nanostructures based on CanDo²⁰ (Fig. 3-23). The bending persistence length was calculated by performing normal mode analysis (NMA) to find the frequency of the first bending mode and adopting the Euler-Bernoulli beam theory.

Normal mode analysis (NMA) was performed at the straight configuration to compute the lowest 20 normal modes of DNA nanostructures. Intrinsic global twist of square-lattice packed structures⁶⁸ was not considered. Given the FE model for a DNA nanostructure under free boundary condition, a generalized eigenvalue problem,

$$Ku = \lambda Mu \quad (10)$$

where K is the stiffness matrix, M is the mass matrix and the eigenvalue $\lambda = \omega^2$ was defined. The Subspace iteration procedure^{84,85} was used to solve the eigenvalue problem using $2N_m$ iteration vectors, where N_m denotes the number of eigenmodes to be calculated. Among the eigenvalues obtained, only the two eigenvalues for the first bending modes were selected to calculate bending stiffness (EI) of DNA nanostructures.

From the Euler-Lagrange equation for a beam representing effectively DNA nanostructures, we could obtain the following free vibration equation.

$$EI \frac{d^4 w}{dx^4} + \mu \omega^2 w = 0 \quad (11)$$

where w describes the lateral deflection of the beam, x represents the axial position,

and μ is the mass per unit length of the beam, respectively. Solving numerically the above equation, we can obtain the natural frequencies of the first bending vibration (ω_B)

$$\omega_B = \frac{4.733^2}{L^2} \sqrt{\frac{EI}{\mu}} \quad (12)$$

where L is the length of the beam. Then, EI of the beam becomes

$$EI = \mu \omega_B^2 \frac{L^4}{4.733^4} = \frac{m}{L} \lambda_B^2 \frac{L^4}{4.733^4} = m \lambda_B^2 \frac{L^3}{4.733^4} \quad (13)$$

where m is the total mass of DNA nanostructures and λ_B is the eigenvalues for the first bending mode. Since the L_p is defined as

$$L_p = \frac{EI}{k_b T} \quad (14)$$

where k_b is the Boltzmann constant and T is absolute temperature, assumed to be 298 K. Then, the L_p of DNA nanostructures becomes

$$L_p = m \lambda_B^2 \frac{L^3}{4.733^4 k_b T} \quad (15)$$

In three-dimensional structure, there are always two first bending modes. Therefore, we defined the first bending mode with a smaller eigenvalue as a major bending mode ($L_{p,1}$) and the other with a larger eigenvalue as a minor bending mode ($L_{p,2}$). Using both bending modes, we defined an effective bending persistence length ($L_{p,e}$), which we compared with experimentally measured L_p ($L_{p,i}^{EXP}$).

$$L_{p,e} = \frac{2}{1/L_{p,1} + 1/L_{p,2}} \quad (16)$$

In our revised model, the crossover and the Holliday junction nick (HJ-nick) elements were modified to be flexible because the rigid crossover model in the original CanDo could not predict the stiffness of multi-helix DNA nanostructures properly. For the HJ-nick element, we determined stiffness factors (SFs) by numerical optimization process to obtain similar persistence length values with

experimental results of 4HB-Ref and 6HB-Ref designs. We solved the following optimization problem using the ‘fmincon’ function in Matlab R2016b (MathWorks Inc.) with numerically calculated gradients

$$\text{Minimize: } f_0 = \sqrt{\frac{1}{2} \sum_{i=1}^2 \left(L_{p,i}^{\text{EXP}} - L_{p,i}^{\text{FE}}(\vec{s}) \right)^2} + \sqrt{\sum_{i=1}^N (A_i - \mu)^2} \quad (17)$$

(where $i = 1$ and 2 represent 4HB and 6HB, respectively)

$$\text{Subject to: } 10^{-6} \leq s_j \leq 10^0$$

$$\vec{s} = [SF_S \quad SF_B \quad SF_C] \quad (18)$$

where s_j is the variable, $L_{p,i}^{\text{EXP}}$ is the experimentally measured L_p , $L_{p,i}^{\text{FE}}$ is the L_p from the FE model, $A_i = |L_{p,i}^{\text{EXP}} - L_{p,i}^{\text{FE}}|$, and $\mu = \frac{1}{2} \sum_{i=1}^2 A_i$, respectively.

After the optimization of HJ-nick element, a nonlinear softening effect of engineered defects with respect to the gap length was modeled with beam elements whose length-dependent rigidity parameters were determined to fit the experimental bending persistence lengths of 4HB and 6HB structures with the maximum gap density (Fig. 3-24 and Table 3-3). Sensitivity analysis on the axial, bending, and torsional rigidity with respect to the bending persistence length of the DNA origami bundle structures were performed (Figs. 3-25 and 3-26), resulting in axial rigidity of the elements were most sensitive. The persistence lengths estimated with this mechanical model agreed quite well with the experimental values (dashed lines in Figs. 3-11 and 3-24) in the whole design range.

As the proposed design strategy and predictive computational model are scalable, they were applied to modulate the mechanical stiffness of DNA nanostructures with other cross-sectional shapes. We analyzed ten cross-sectional shapes (including 4HB and 6HB) consisting of four to sixteen helices that were

newly designed or demonstrated in previous works^{76,81} (Fig. 3-27). The bending stiffness of typical DNA bundles is known to generally follow the N^2 scaling trend (N , number of helices)²⁵. By introducing the defect-engineering process, 57-78% of maximum reduction in bending stiffness was predicted by the FE simulation and the stiffness between its maximum and minimum values could be realized by defect designs with proper selection of gap parameters (Figs. 3-28 to 32). It is important to note that the range of the bending stiffness presented here is corresponding to one of many possible design cases. It can vary with the layout of scaffold and staple routes determining the number and arrangement of gap sites.

To cross-validate our computational model, we additionally constructed ten helix bundle (10HB) structures with five variations in gap density (Fig. 3-33). Mostly, 5-nt long gaps were used throughout the structure. However, 4-nt long gaps were used instead in the regions where the distance between adjacent inter-helix crossovers was 7-nt long. Maximum and minimum bending persistence lengths were measured as 5,430 and 2,180 nm, respectively, in a good agreement with the predicted values, demonstrating the usefulness of the developed computational model in stiffness design. Because of the anisotropy in the cross-sectional layout, we calculated the harmonic mean values from the first two bending modes in FE simulation to compare with the experimental results (Fig. 3-34) utilizing the symmetry of the cross-section.

We also applied the defect-engineering method for stiffness control to design a mechanically flexible hinge, whose included angle was controlled by an external dsDNA adjuster strand (Fig. 3-35a). When the bundle had a shorter adjuster than its contour length with the absence of a flexible region, it tended to aggregate with one another in straight conformations rather than form a bent monomer because forming straight aggregations would be energetically more favorable than folded into

bent monomers for stiff bundles. In the previous report⁴³, it was observed that decreasing the number of dsDNA helices at the hinge, thereby reducing the bending stiffness, could prevent aggregation. Here, we discovered that inserting engineered defects at the hinge without modifying the cross-section could yield a similar softening effect. Significant improvement on the structural folding yield by adopting the defect-engineering method was confirmed by both gel electrophoresis and AFM measurement (Fig. 3-35b to 3-35d). This result demonstrates that the proposed method can be easily applied to structural shape design as well where the local and modular stiffness modulation is highly utilized⁴³.

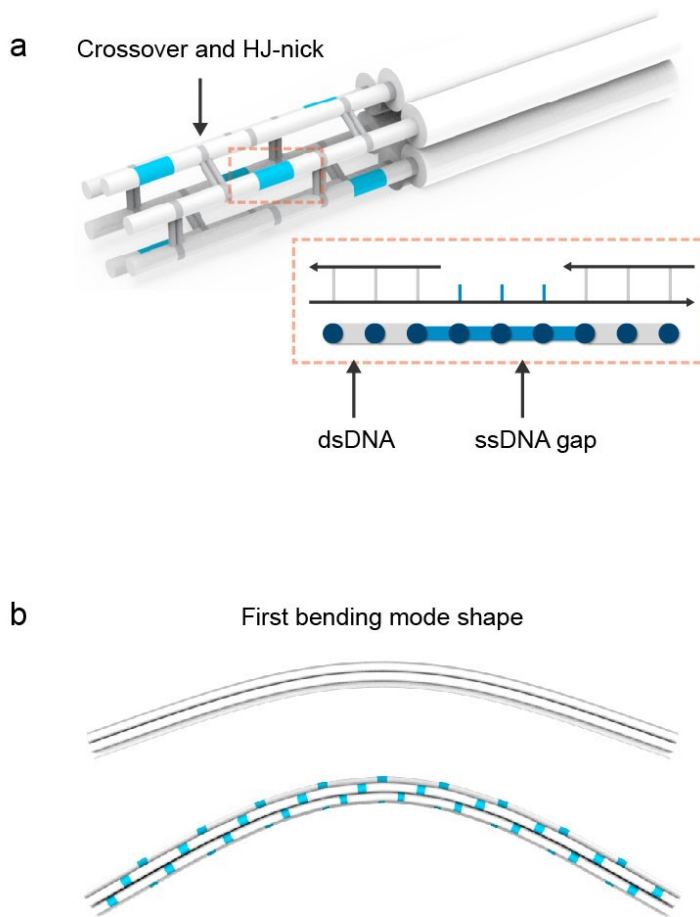


Figure 3-23. Schematic illustration of the FE model. (a) Inter-helix crossovers and HJ-nick elements are shown in grey while the ssDNA gaps are denoted using blue cylinders. Normal dsDNA and ssDNA gaps are modeled with beam elements having different mechanical stiffness values as illustrated in the orange box. **(b)** Schematic illustration of the first bending mode obtained from NMA. The length of bundles was shortened to a scale of 1/3 for clear visualization.

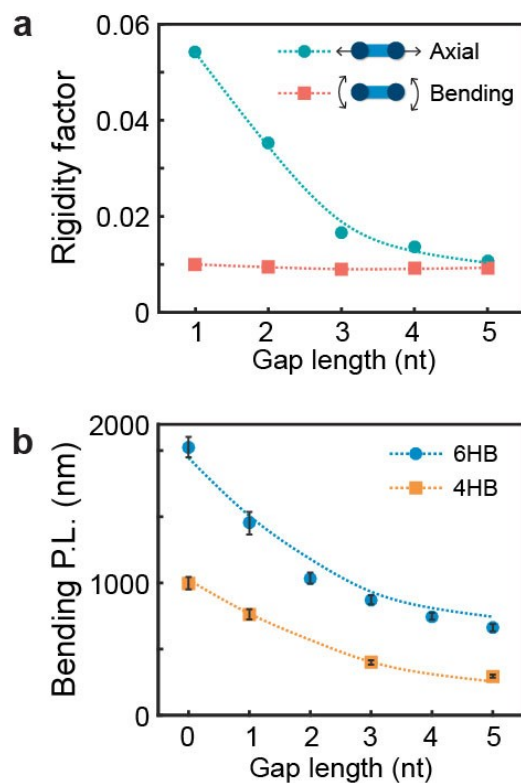


Figure 3-24. FE modeling of defect-engineered structures. (a) Relative rigidity factors of the gap element with respect to the normal dsDNA element, determined by performing FE parameter optimization to fit the experimental values of 1-nt, 3-nt, and 5-nt gap designs with full gap density. Rigidities of 2-nt and 4-nt gap elements were derived from the quadratic interpolation of adjacent values. Note that the bending persistence length of bundles were largely affected by the axial rigidity of the gap element. Refer to Fig. 3-26 for the detailed parameter test. **(b)** Comparison with experimentally measured and numerically predicted bending persistence lengths. Dotted lines indicate the spline-fitted curves of computationally calculated values. Error bars denote the standard deviation of experimental results. (P.L.: Persistence Length).

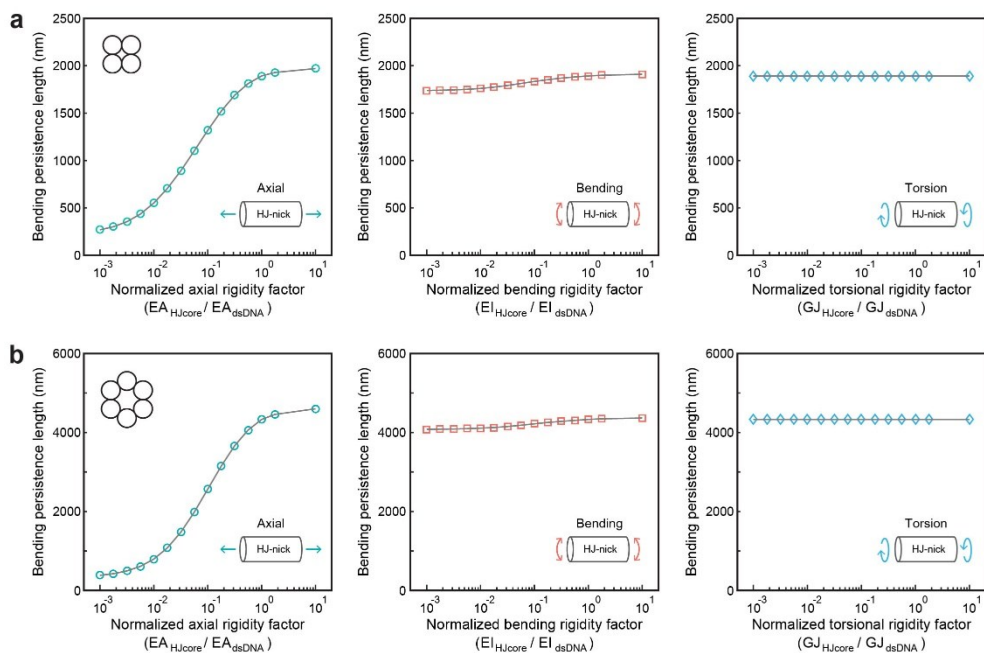


Figure 3-25. Sensitivity analysis for the HJ-nick element. Calculated bending persistence length of the bundle in **(a)** 4HB-Ref and **(b)** 6HB-Ref design was shown. While varying axial, bending, or torsional stiffness of the HJcore element, the other two normalized parameters were fixed as 1.

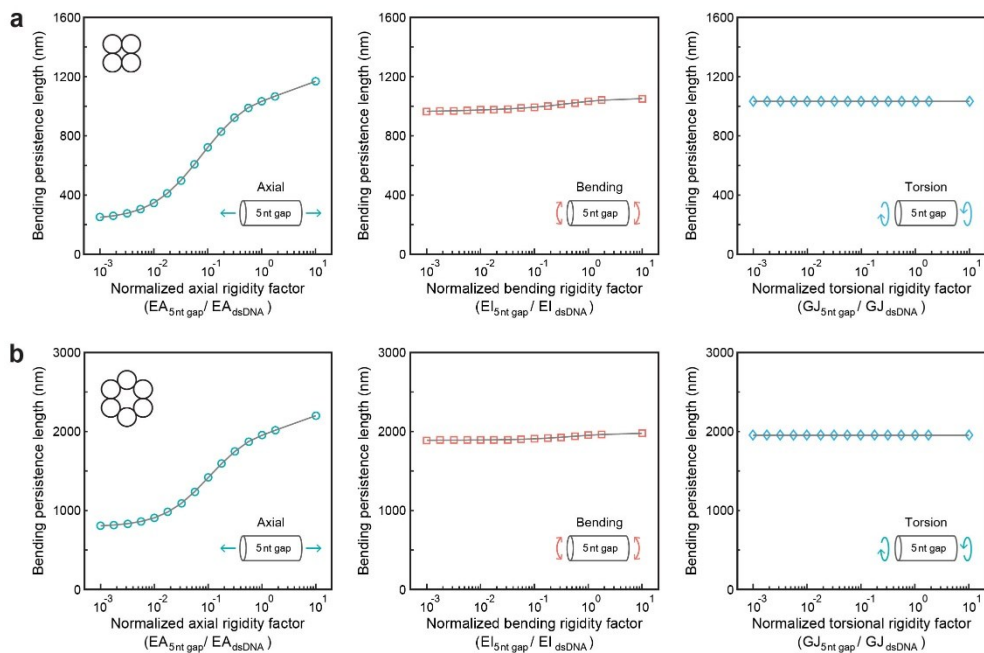


Figure 3-26. Sensitivity analysis for the 5-nt-long ssDNA gap element. Calculated bending persistence length of the bundle in **(a)** 4HB-5nt-100% and **(b)** 6HB-5nt-100% design was shown. Stiffness factor of the HJcore element used here was shown in Table 3-3. While varying axial, bending, or torsional stiffness of the 5-nt-long ssDNA gap element, the other two normalized parameters were fixed as 1.

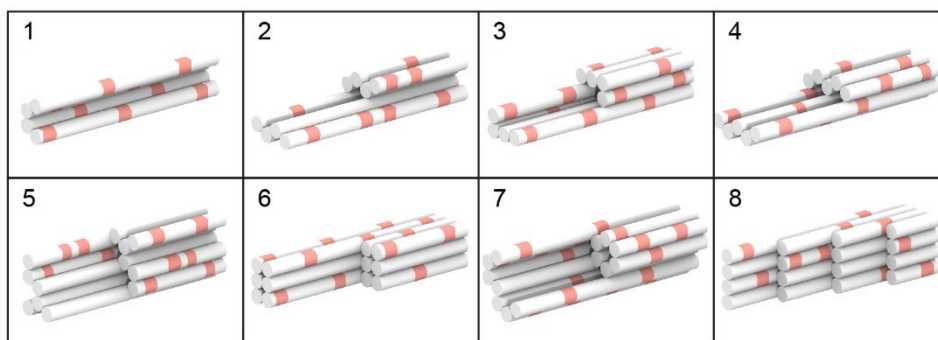


Figure 3-27. Schematic illustration of various cross-section designs with full density of the engineered defects.

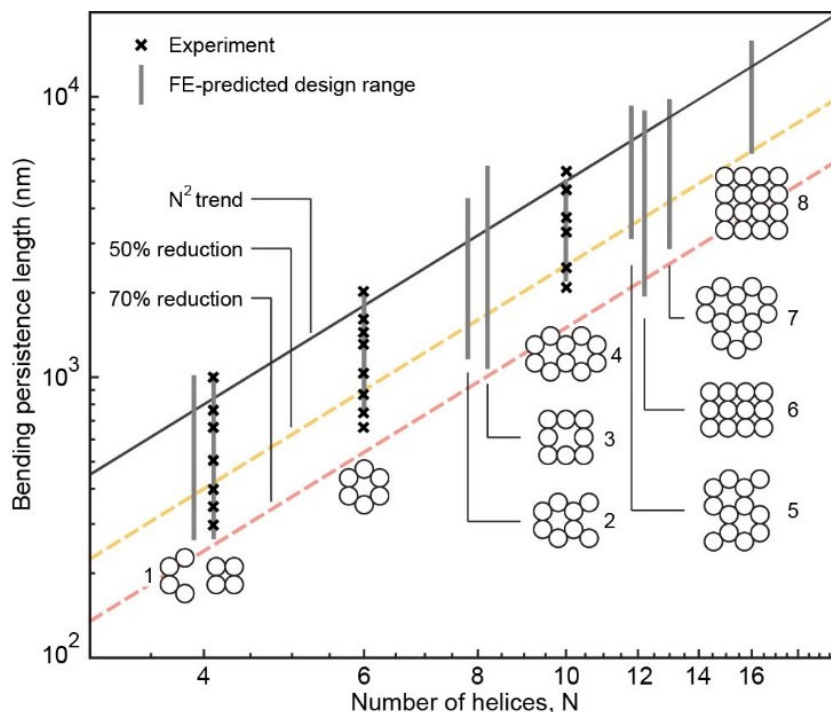


Figure 3-28. Application of the defect-engineering design method for stiffness control of bundles with various cross-sections. Bending persistence lengths of bundles with various cross-sectional shapes designed with engineered defects. Grey bars indicate the range of bending stiffness achievable for each cross-section estimated by the FE simulation. Cross marks on the bars denote the experimentally measured values for different gap designs. The black solid line shows the theoretical N^2 (N , the number of constituting dsDNA helices) scaling trend, known to be valid when all the helices are rigidly coupled with each other. The yellow and red dotted lines correspond to 50% and 70% reductions of theoretical values, respectively. The bending persistence length of a DNA duplex is assumed as 50 nm.

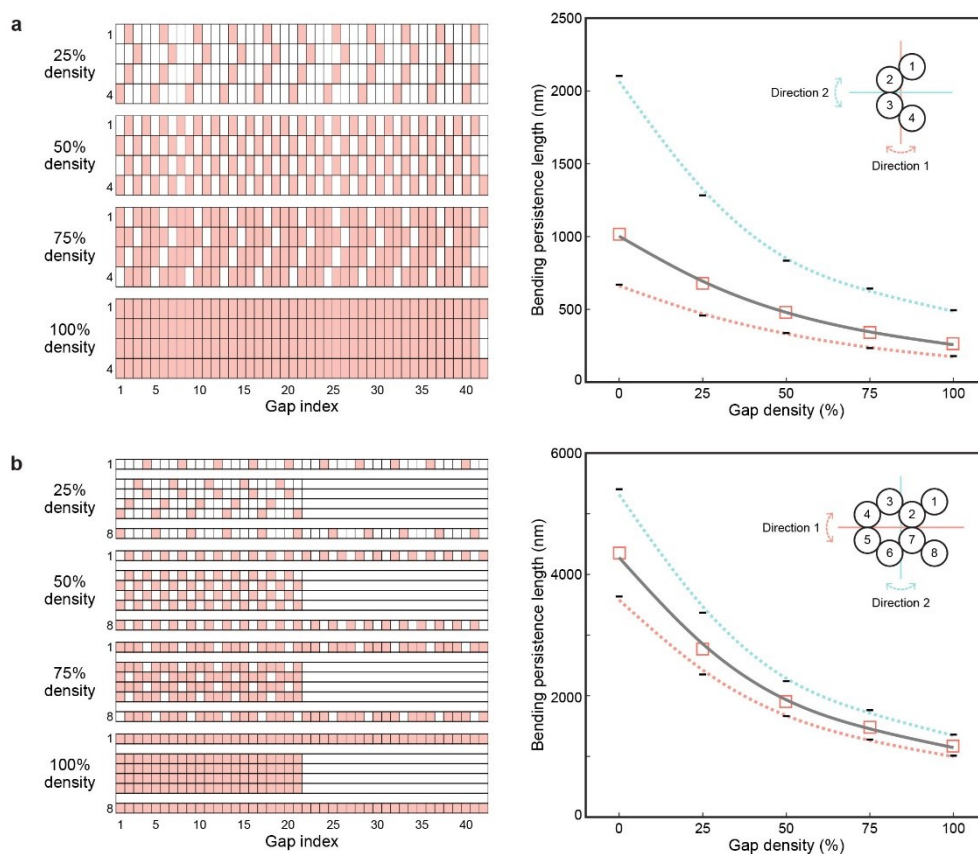


Figure 3-29. Gap layout and estimated bending persistence length of (a) 4HB-hex and (b) 8HB-hex design. Red colored boxes indicate the location of 5-nt-long gaps. Red and teal dotted lines in the graph are spline-fitted curves of the bending persistence length calculated from two different first bending modes in NMA. Red empty boxes are harmonic mean of the two values and grey solid line is the spline-fitted curve of them.

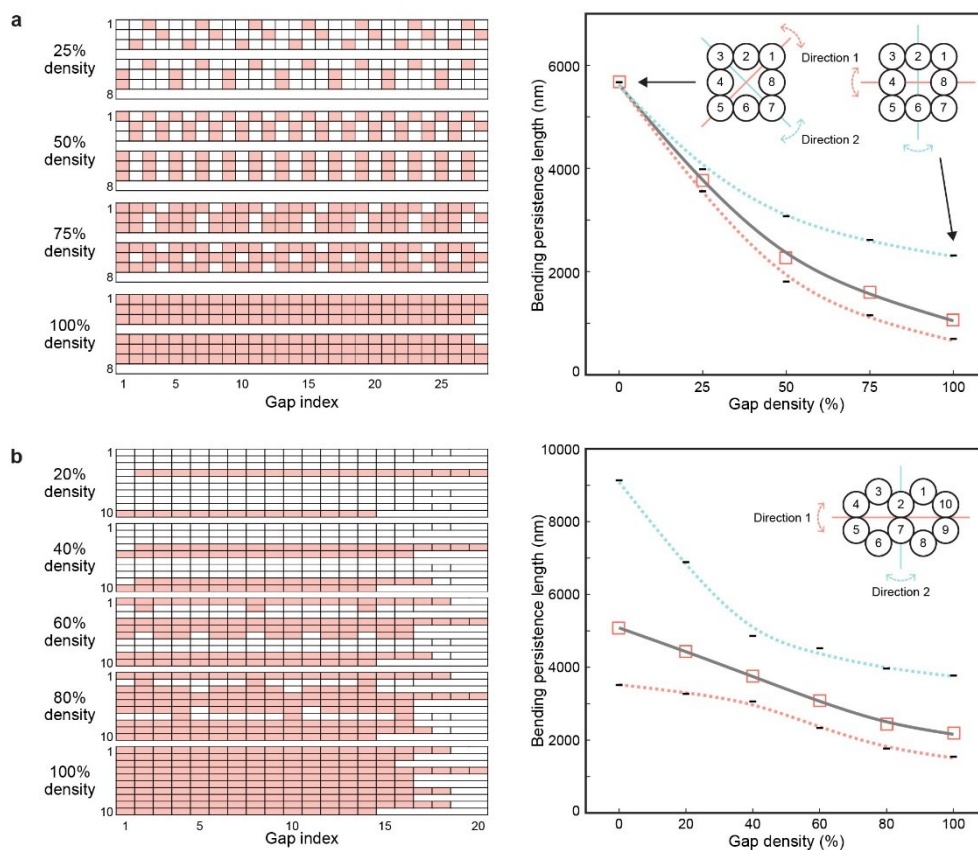


Figure 3-30. Gap layout and estimated bending persistence length of (a) 8HB-sq and (b) 10HB-hex design. Red colored boxes indicate the location of 5-nt-long gaps. Red and teal dotted lines in the graph are spline-fitted curves of the bending persistence length calculated from two different first bending modes in NMA. Red empty boxes are harmonic mean of the two values and grey solid line is the spline-fitted curve of them.

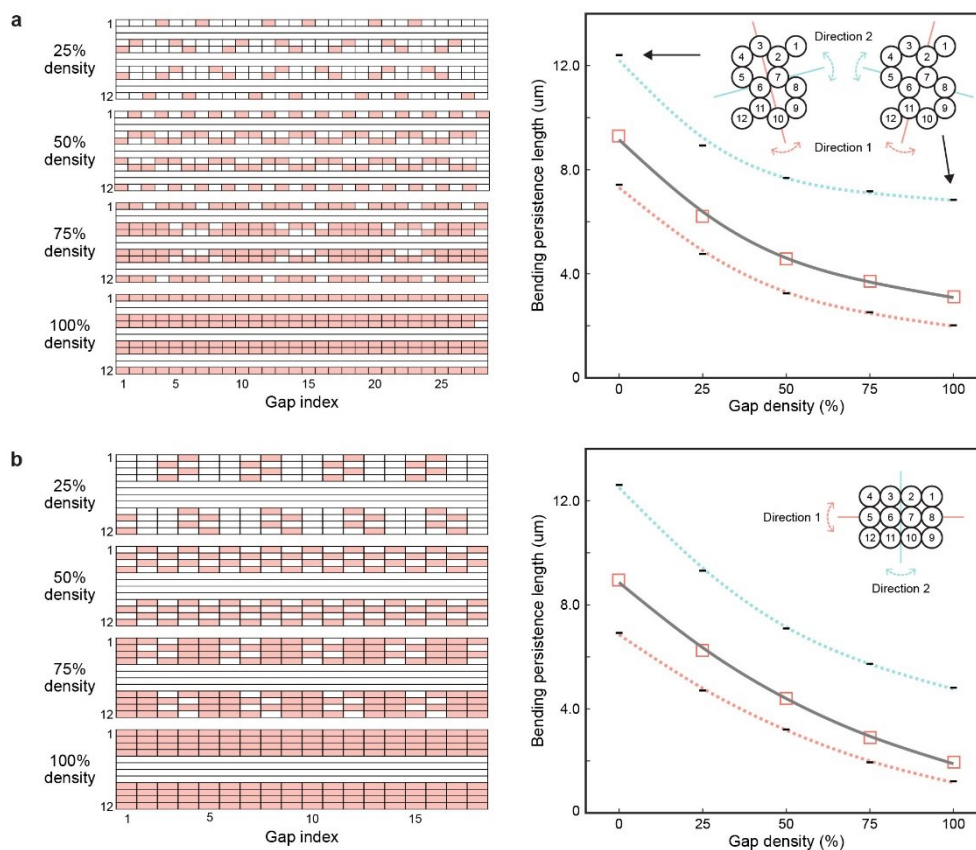


Figure 3-31. Gap layout and estimated bending persistence length of (a) 12HB-hex and (b) 12HB-sq design. Red colored boxes indicate the location of 5-nt-long gaps. Red and teal dotted lines in the graph are spline-fitted curves of the bending persistence length calculated from two different first bending modes in NMA. Red empty boxes are harmonic mean of the two values and grey solid line is the spline-fitted curve of them.

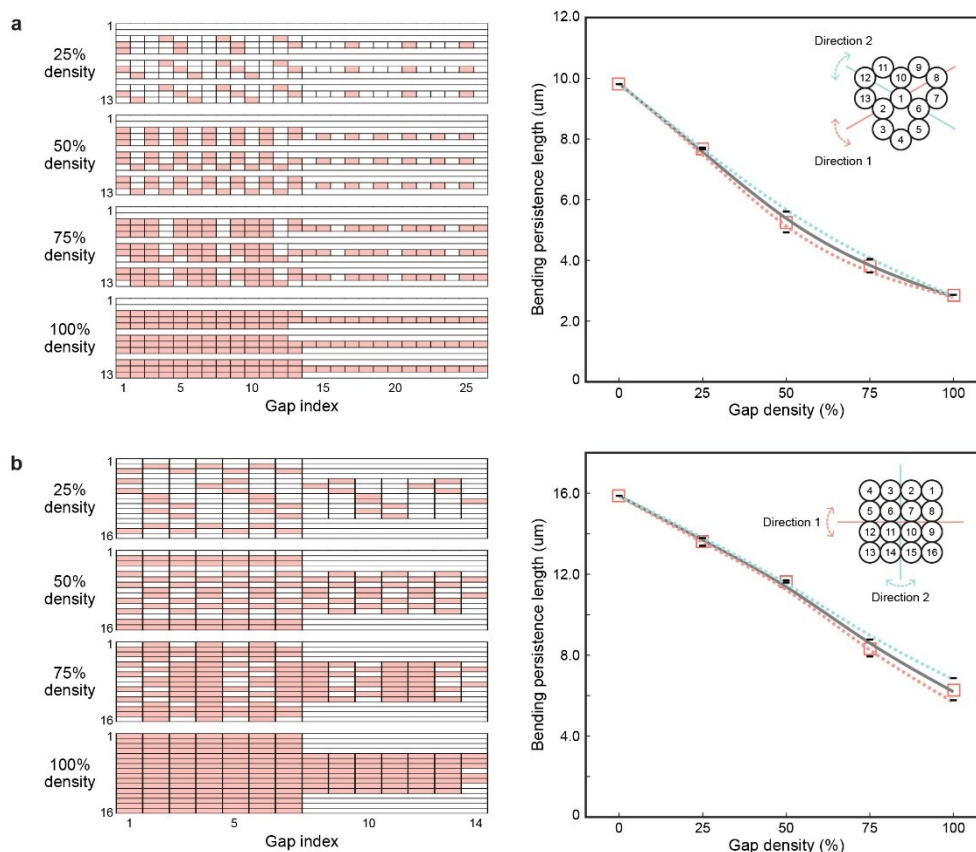


Figure 3-32. Gap layout and estimated bending persistence length of (a) 13HB-hex and (b) 16HB-sq design. Red colored boxes indicate the location of 5-nt-long gaps. Red and teal dotted lines in the graph are spline-fitted curves of the bending persistence length calculated from two different first bending modes in NMA. Red empty boxes are harmonic mean of the two values and grey solid line is the spline-fitted curve of them.

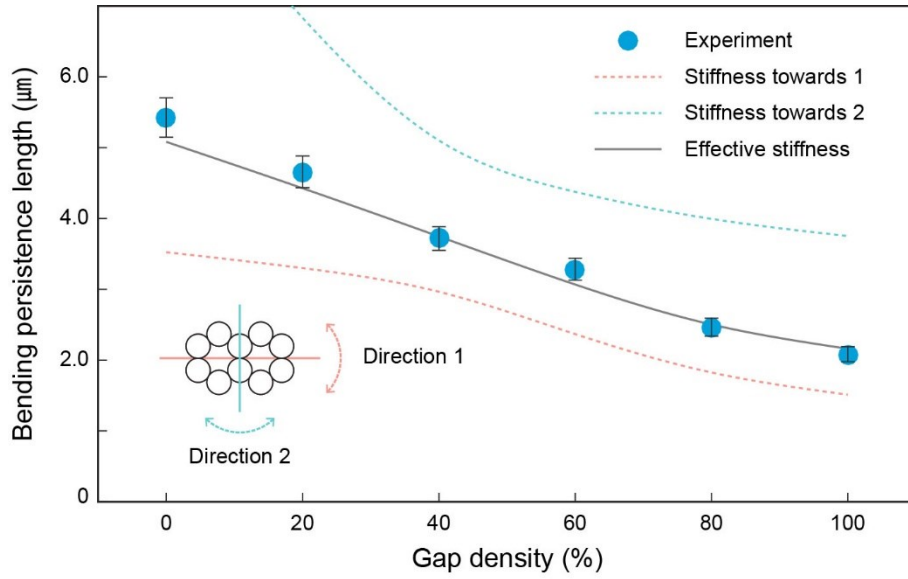


Figure 3-33. Experimental results of 10HB with gap density variations for cross-validation with FE simulation. Error bars indicate the standard deviation of experimental results.

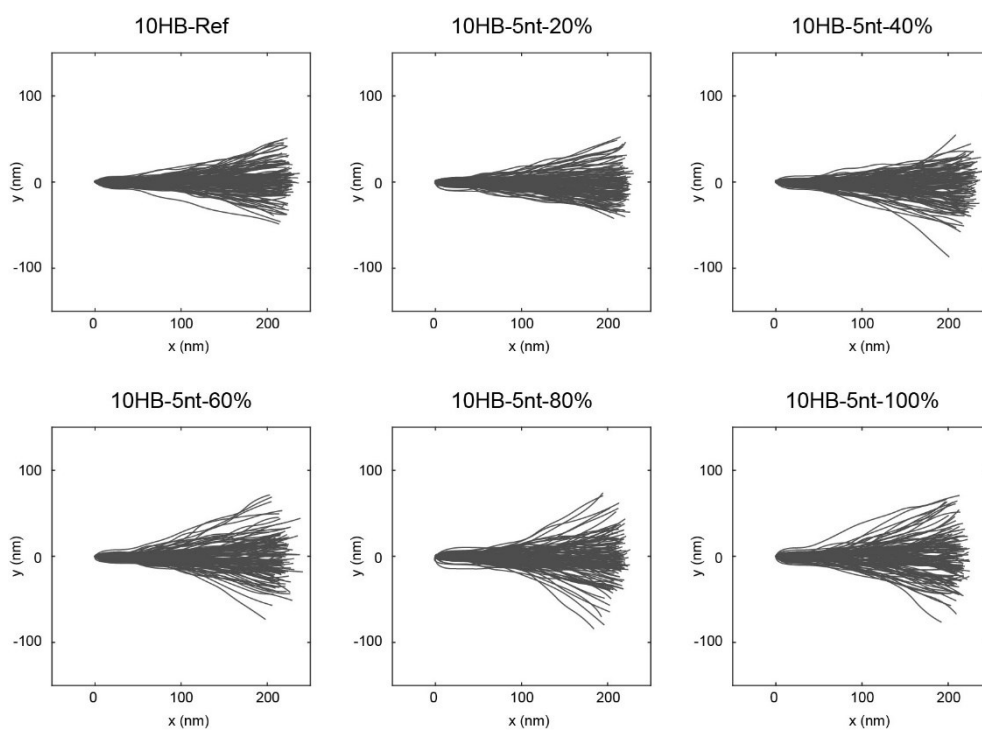


Figure 3-34. Experimental characterization of 10HB with 5-nt gap variations.

Aligned contour distribution of 120 representative monomers measured from AFM.

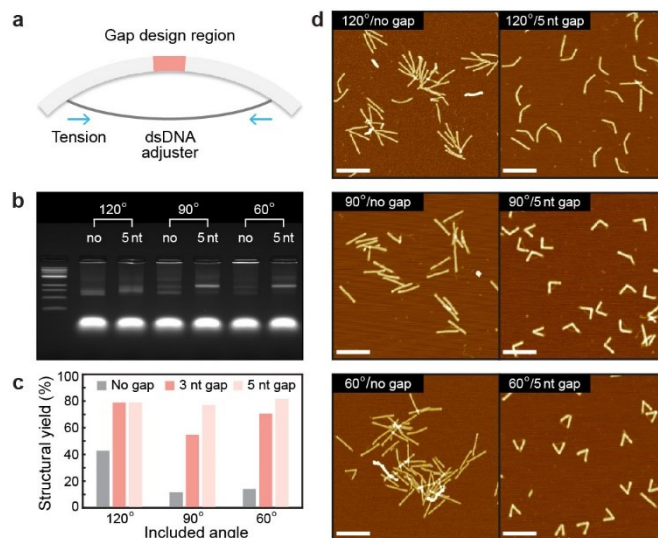


Figure 3-35. Demonstration of the enhancement in structural yield for bent DNA bundles through defect-engineering. (a) Schematic illustration of bent DNA bundle design with adjustable included angle. Red represents the hinge region whose stiffness is modulated using engineered defects. 12HB structures of three different included angles were designed with and without engineering defects. **(b)** Gel electrophoresis results of normal and defect-engineered designs. **(c)** Structural folding yield. Significant enhancement was observed in all the cases. **(d)** Representative AFM images (scale bars: 300 nm).

Interhelix distance (nm)			
Honeycomb lattice	2.25	Square lattice	2.5
Mechanical properties			
	EA (pN)	EI (pN·nm ²)	GJ (pN·nm ²)
dsDNA element	1100	230	460
Normalized rigidity factor (with respect to dsDNA element)			
Crossover element	1.0	0.2	0.1
HJ-nick element	0.069	0.117	1.0
Nick element	1.0	1.0	1.0
1-nt ssDNA gap element	0.054	0.01	0.01
2-nt ssDNA gap element	0.035	0.009	0.01
3-nt ssDNA gap element	0.017	0.009	0.01
4-nt ssDNA gap element	0.014	0.009	0.01
5-nt ssDNA gap element	0.011	0.009	0.01

Table 3-3. Parameters used in FE modeling.

3.5. Molecular dynamics simulation

To further validate the developed computational model for DNA nanostructures with engineered defects and analyze the effect of ssDNA gaps at the individual base level, we performed the MD simulation for 84-nt long 6HB structures whose stiffness was reduced by using 1-nt, 3-nt, and 5-nt long gaps (Fig. 3-36). We extracted the final 200 ns of molecular trajectories for each case after the equilibrium state was reached and compared them with the result for the reference design without gaps (having 12 nicks only).

First, the time-average fluctuation of five cross-sectional planes of each design was calculated (Fig. 3-37a). For the two base pairs of a cross-section, their origins were calculated following the 3DNA definition⁸⁶ to provide a center point by averaging them. The three-dimensional dynamics of six center points was reduced to two-dimensional planar motion, by introducing in a projected hexagonal plane with six vertices (Fig. 3-37b), which minimizes the distance from the plane to six center points. Vertex vectors (n_i) were then obtained representing the position of each vertex, and edge vectors (v_i) were determined using connected two vertices as

$$v_i = n_{i+1} - n_i \quad (19)$$

The interior angle in hexagon (θ_i) was calculated using two successive vertex vectors as

$$\theta_i = \cos^{-1}[(v_i \cdot v_{i+1})/(|v_i||v_{i+1}|)] \quad (20)$$

suggesting that the average of the angles should be 120° and their standard deviation implies the angular fluctuation of a cross-section. A cross-sectional area of a hexagon (A_i) can be derived as

$$A_i = |c_i \times v_i|/2 \quad (21)$$

where the hexagonal center vector (c_i) was defined as a vector from the vertex to the hexagonal center point, resulting in the area of the hexagonal plane as the summation of six sectional areas. The distance between hexagonal planes (d_n) was defined as the distance between hexagonal center points (Fig. 3-37c). This cross-section analysis described above was performed for all snapshots of final 200-ns-long MD trajectories, therefore providing the probability density functions or standard deviations of cross-sectional variables. It was confirmed that the deviation of interior angles remained in similar levels regardless of gap design (Fig. 3-38).

The average areas of planes and the inter-plane distances of defect-engineered structures differed only by 1.7~14.1% and less than 0.2%, respectively, with respect to the reference design (Fig. 3-39). We also calculated the bending persistence length from MD trajectories by performing the principal component analysis (PCA). Relative bending persistence length ratios between the reference and the gapped structures demonstrated a good agreement with the FE analysis results as well as the experimental data (Fig. 3-40), which supported the validity of FE mechanical model developed in this study.

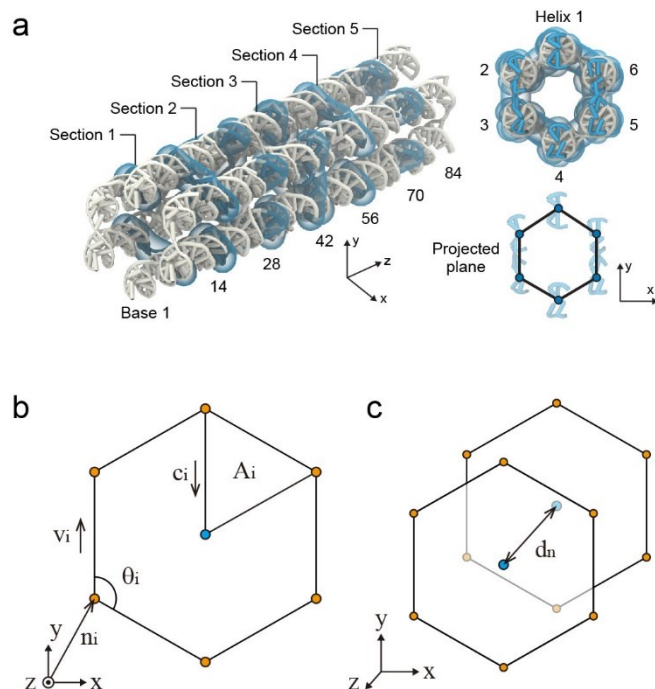


Figure 3-37. Schematic illustration of 6HB used in the MD simulation. (a) Trajectories of base pairs in blue-colored sections were analyzed by projecting their positions onto a representative 2D plane. Calculation of the **(b)** area and **(c)** inter-plane distance of projected 2D surfaces is shown.

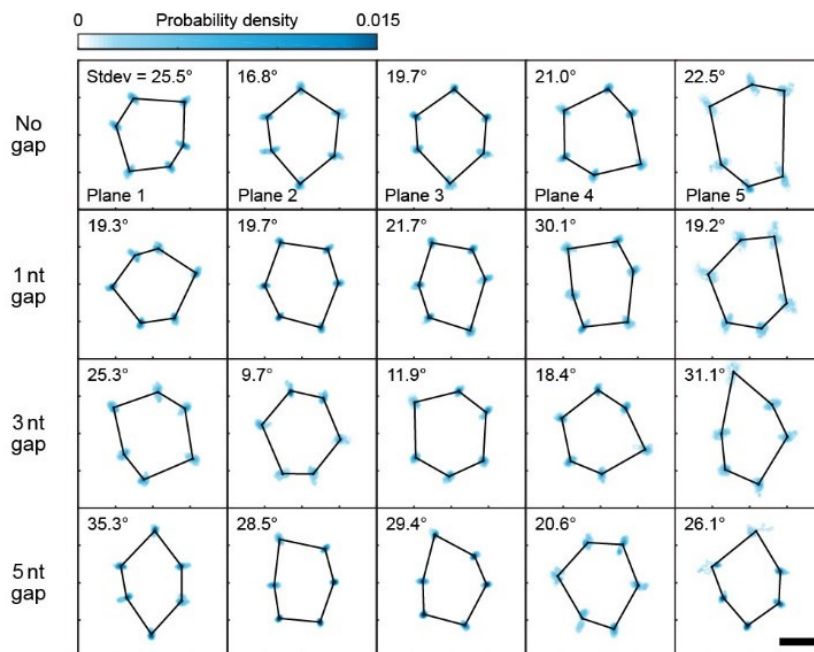


Figure 3-38. The time-average cross-sectional shape of five representative planes of 6HB structures with and without gaps. The blue regions indicate the base pair coordinates at each vertex and the angles indicate the time-average standard deviation of six interior angles (ticks and scale bar: 20 Å).

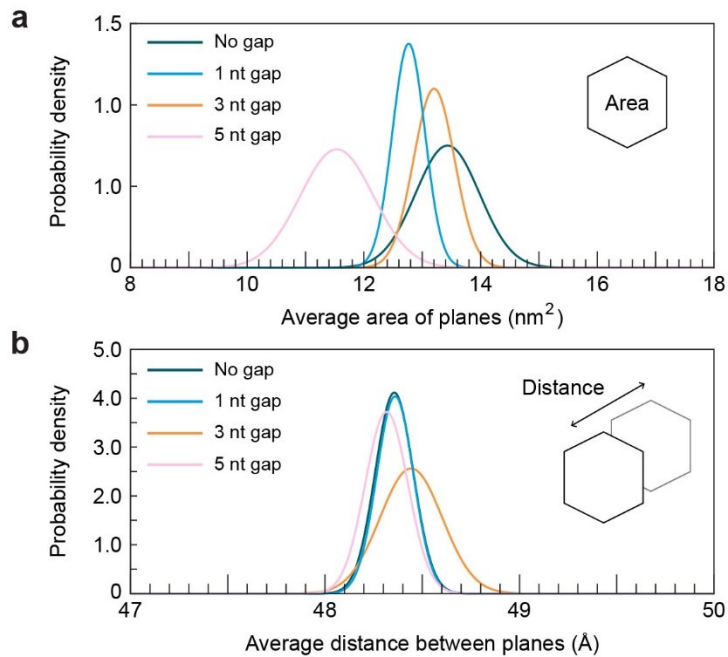


Figure 3-39. Geometrical characteristics of cross-sections. (a) The average area of five hexagonal planes for each design. **(b)** The average inter-plane distance for each design.

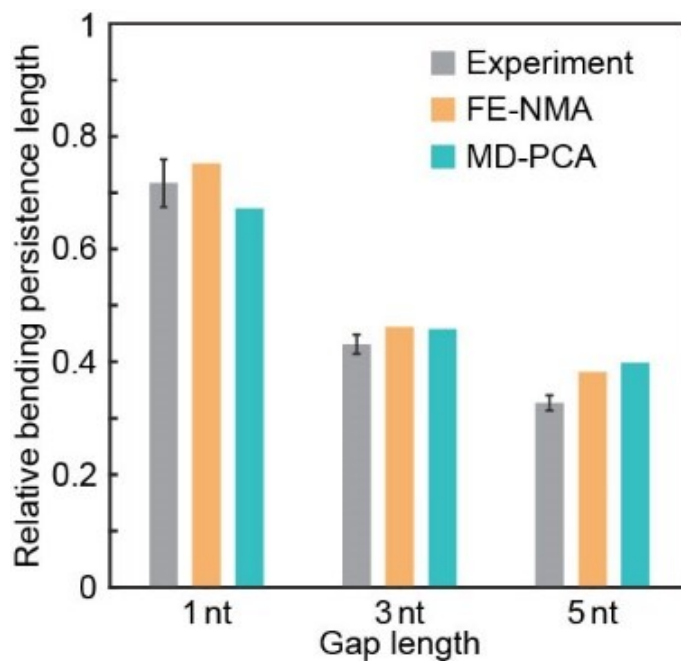


Figure 3-40. Comparison of bending stiffness results. Relative bending persistence lengths of the defect-engineered 6HB with the reference one determined from experiments, NMA of FE simulation, and PCA of MD trajectories.

3.6. Conclusion

In summary, our stiffness design method based on engineered defects offers a simple and versatile way of controlling the bending stiffness of DNA nanostructures without altering geometric features. We expect that the proposed design method, in combination with a proper validation tool such as an optical or a magnetic tweezer, can potentially be expanded to tailor other (axial or torsional) stiffness properties of DNA constructs as well. Also, it might be possible to actively control engineered defects by incorporating stimuli-responsive molecules into gap sites, thereby making the active stiffness modulation possible. In terms of addressability, our design method is expected to enable a wide range of applications that are suitable for kinematic nanodevices, single-molecule sensors, and substrates for nanomaterials with controllable functionality.

Chapter 4. Concluding remark

In this thesis, we presented two types of the design method to efficiently control the mechanical stiffness of DNA origami nanostructures. In the first design method, multiple structural variations were demonstrated by the combination of stiffness-tunable flexible modules and the adjuster strand whose length can be controlled by the adjuster module. The second method used ssDNA gaps with engineered positions and lengths, which reduced the overall bending stiffness of a DNA nanostructure while preserving the structural integrity. Both methods were based on the modular approach, in which the staple sequences of unmodified regions were preserved. We investigated the design parameters and the applicable range of stiffness modification in both design methods by a comprehensive set of experiments. Also, a FEA-based computational shape and mechanical property prediction platform was integrated to the design process. It enabled the more effective design and validation process, resulting in the significant reduction of cost in terms of testing multiple design candidates and finding the estimated performance of them. Since our method is scalable and easily addressable to various DNA origami structures designed by current shape design rules, a number of potential application are expected when the performance of the functional DNA origami structures are related with the mechanical property of them. Examples can include single-molecule sensors, molecular carriers for intracellular delivery, and substrates for supramolecular assembly formation, whose performance can be enhanced by tuning the characteristics between other materials and surroundings.

Acknowledgments

I would first like to thank my dissertation advisor Prof. Do-Nyun Kim, who gave a great opportunity to join the lab and supports during the doctoral course. I really enjoyed the research with him started from scratch, with numerous discussions and invaluable assistance. I also would like to acknowledge the rest of my dissertation committee members: Prof. Maenghyo Cho, Prof. Yoon Young Kim, Prof. Yongdae Shin, and Prof. Seunghwa Yang for their generosity and excellent advice.

Besides, I wish to thank my colleagues in the Simulation-Driven Structure Design Laboratory at Seoul National University for their brilliant contributions. Specifically, I thank Jae Young Lee for the MD simulation and analysis of the result, Young-Joo Kim for the development of an FE model for defect-engineered DNA nanostructures, and Kyung Soo Kim for the calculation of persistence length from the experiments.

I gratefully acknowledge the generous support of the Kwanjeong Educational Foundation during the coursework.

Finally, I would like to express my deepest gratitude to my parents and brother, who gave unconditional and endless support for me.

Bibliography

- 1 Wang, P., Meyer, T. A., Pan, V., Dutta, P. K. & Ke, Y. The Beauty and Utility of DNA Origami. *Chem* **2**, 359-382 (2017).
- 2 Seeman, N. C. Nucleic acid junctions and lattices. *J. Theor. Biol.* **99**, 237-247 (1982).
- 3 Seeman, N. C. Nanomaterials Based on DNA. *Annu. Rev. Biochem.* **79**, 65-87 (2010).
- 4 Rothemund, P. W. K. Folding DNA to create nanoscale shapes and patterns. *Nature* **440**, 297-302 (2006).
- 5 Linko, V. & Dietz, H. The enabled state of DNA nanotechnology. *Curr. Opin. Biotechnol.* **24**, 555-561 (2013).
- 6 Tørring, T., Voigt, N. V., Nangreave, J., Yan, H. & Gothelf, K. V. DNA origami: a quantum leap for self-assembly of complex structures. *Chem. Soc. Rev.* **40**, 5636-5646 (2011).
- 7 Yin, P. *et al.* Programming DNA Tube Circumferences. *Science* **321**, 824-826 (2008).
- 8 Castro, C. E. *et al.* A primer to scaffolded DNA origami. *Nat. Methods* **8**, 221-229 (2011).
- 9 Sobczak, J.-P. J., Martin, T. G., Gerling, T. & Dietz, H. Rapid Folding of DNA into Nanoscale Shapes at Constant Temperature. *Science* **338**, 1458-1461 (2012).
- 10 Douglas, S. M. *et al.* Self-assembly of DNA into nanoscale three-dimensional shapes. *Nature* **459**, 414-418 (2009).

- 11 Douglas, S. M. *et al.* Rapid prototyping of 3D DNA-origami shapes with caDNAno. *Nucleic Acids Res.* **37**, 5001-5006 (2009).
- 12 Veneziano, R. *et al.* Designer nanoscale DNA assemblies programmed from the top down. *Science* **352**, 1534 (2016).
- 13 Jun, H. *et al.* Autonomously designed free-form 2D DNA origami. *Sci. Adv.* **5**, eaav0655 (2019).
- 14 Niekamp, S. *et al.* Folding complex DNA nanostructures from limited sets of reusable sequences. *Nucleic Acids Res.* **44**, e102 (2016).
- 15 Jabbari, H., Aminpour, M. & Montemagno, C. Computational Approaches to Nucleic Acid Origami. *ACS Comb. Sci.* **17**, 535-547 (2015).
- 16 Doye, J. P. K. *et al.* Coarse-graining DNA for simulations of DNA nanotechnology. *Phys. Chem. Chem. Phys.* **15**, 20395-20414 (2013).
- 17 Yoo, J. & Aksimentiev, A. In situ structure and dynamics of DNA origami determined through molecular dynamics simulations. *Proc. Natl. Acad. Sci. U.S.A.* **110**, 20099-20104 (2013).
- 18 Snodin, B. E. K. *et al.* Direct Simulation of the Self-Assembly of a Small DNA Origami. *ACS Nano* **10**, 1724-1737 (2016).
- 19 Huang, C.-M., Kucinic, A., Le, J. V., Castro, C. E. & Su, H.-J. Uncertainty quantification of a DNA origami mechanism using a coarse-grained model and kinematic variance analysis. *Nanoscale* **11**, 1647-1660 (2019).
- 20 Kim, D.-N., Kilchherr, F., Dietz, H. & Bathe, M. Quantitative prediction of 3D solution shape and flexibility of nucleic acid nanostructures. *Nucleic Acids Res.* **40**, 2862-2868 (2012).
- 21 Pinheiro, A. V., Han, D., Shih, W. M. & Yan, H. Challenges and opportunities for structural DNA nanotechnology. *Nat. Nanotechnol.* **6**, 763-

- 772 (2011).
- 22 Shih, W. M. & Lin, C. Knitting complex weaves with DNA origami. *Curr. Opin. Struct. Biol.* **20**, 276-282 (2010).
- 23 Han, D. *et al.* DNA Origami with Complex Curvatures in Three-Dimensional Space. *Science* **332**, 342-346 (2011).
- 24 Benson, E. *et al.* DNA rendering of polyhedral meshes at the nanoscale. *Nature* **523**, 441-444 (2015).
- 25 Castro, C. E., Su, H.-J., Marras, A. E., Zhou, L. & Johnson, J. Mechanical design of DNA nanostructures. *Nanoscale* **7**, 5913-5921 (2015).
- 26 Kuzuya, A., Sakai, Y., Yamazaki, T., Xu, Y. & Komiyama, M. Nanomechanical DNA origami 'single-molecule beacons' directly imaged by atomic force microscopy. *Nat. Commun.* **2**, 449 (2011).
- 27 Ke, Y., Meyer, T., Shih, W. M. & Bellot, G. Regulation at a distance of biomolecular interactions using a DNA origami nanoactuator. *Nat. Commun.* **7**, 10935 (2016).
- 28 Siavashpouri, M. *et al.* Molecular engineering of chiral colloidal liquid crystals using DNA origami. *Nat. Mater.* **16**, 849-856 (2017).
- 29 Douglas, S. M., Bachelet, I. & Church, G. M. A Logic-Gated Nanorobot for Targeted Transport of Molecular Payloads. *Science* **335**, 831-834 (2012).
- 30 Kuzyk, A. *et al.* Reconfigurable 3D plasmonic metamolecules. *Nat. Mater.* **13**, 862-866 (2014).
- 31 Zhan, P. *et al.* Reconfigurable Three-Dimensional Gold Nanorod Plasmonic Nanostructures Organized on DNA Origami Tripod. *ACS Nano* **11**, 1172-1179 (2017).
- 32 Funke, J. J., Ketterer, P., Lieleg, C., Korber, P. & Dietz, H. Exploring

- Nucleosome Unwrapping Using DNA Origami. *Nano Lett.* **16**, 7891-7898 (2016).
- 33 Funke, J. J. *et al.* Uncovering the forces between nucleosomes using DNA origami. *Sci. Adv.* **2**, e1600974 (2016).
- 34 Kilchherr, F. *et al.* Single-molecule dissection of stacking forces in DNA. *Science* **353**, aaf5508 (2016).
- 35 Nickels, P. C. *et al.* Molecular force spectroscopy with a DNA origami–based nanoscopic force clamp. *Science* **354**, 305-307 (2016).
- 36 Le, J. V. *et al.* Probing Nucleosome Stability with a DNA Origami Nanocaliper. *ACS Nano* **10**, 7073-7084 (2016).
- 37 Wang, T., Schiffels, D., Martinez Cuesta, S., Kuchnir Fygenson, D. & Seeman, N. C. Design and Characterization of 1D Nanotubes and 2D Periodic Arrays Self-Assembled from DNA Multi-Helix Bundles. *J. Am. Chem. Soc.* **134**, 1606-1616 (2012).
- 38 Pfeifer, W., Lill, P., Gatsogiannis, C. & Saccà, B. Hierarchical Assembly of DNA Filaments with Designer Elastic Properties. *ACS Nano* **12**, 44-55 (2018).
- 39 Marras, A. E., Zhou, L., Su, H.-J. & Castro, C. E. Programmable motion of DNA origami mechanisms. *Proc. Natl. Acad. Sci. U.S.A.* **112**, 713-718 (2015).
- 40 Zhou, L., Marras, A. E., Su, H.-J. & Castro, C. E. DNA Origami Compliant Nanostructures with Tunable Mechanical Properties. *ACS Nano* **8**, 27-34 (2014).
- 41 Benson, E. *et al.* Effects of Design Choices on the Stiffness of Wireframe DNA Origami Structures. *ACS Nano* **12**, 9291-9299 (2018).

- 42 Jun, H. *et al.* Automated Sequence Design of 3D Polyhedral Wireframe DNA Origami with Honeycomb Edges. *ACS Nano* **13**, 2083-2093 (2019).
- 43 Lee, C., Lee, J. Y. & Kim, D.-N. Polymorphic design of DNA origami structures through mechanical control of modular components. *Nat. Commun.* **8**, 2067 (2017).
- 44 Andersen, E. S. *et al.* DNA Origami Design of Dolphin-Shaped Structures with Flexible Tails. *ACS Nano* **2**, 1213-1218 (2008).
- 45 Dietz, H., Douglas, S. M. & Shih, W. M. Folding DNA into Twisted and Curved Nanoscale Shapes. *Science* **325**, 725-730 (2009).
- 46 Maier, A. M. *et al.* Self-Assembled DNA Tubes Forming Helices of Controlled Diameter and Chirality. *ACS Nano* **11**, 1301-1306 (2017).
- 47 Inuma, R. *et al.* Polyhedra Self-Assembled from DNA Tripods and Characterized with 3D DNA-PAINT. *Science* **344**, 65-69 (2014).
- 48 Tian, Y. *et al.* Lattice engineering through nanoparticle-DNA frameworks. *Nat. Mater.* **15**, 654-661 (2016).
- 49 Funke, J. J. & Dietz, H. Placing molecules with Bohr radius resolution using DNA origami. *Nat. Nanotechnol.* **11**, 47-52 (2016).
- 50 Saccà, B. *et al.* Reversible Reconfiguration of DNA Origami Nanochambers Monitored by Single-Molecule FRET. *Angew. Chem. Int. Ed.* **54**, 3592-3597 (2015).
- 51 Gerling, T., Wagenbauer, K. F., Neuner, A. M. & Dietz, H. Dynamic DNA devices and assemblies formed by shape-complementary, non-base pairing 3D components. *Science* **347**, 1446-1452 (2015).
- 52 Kuzyk, A. *et al.* A light-driven three-dimensional plasmonic nanosystem that translates molecular motion into reversible chiroptical function. *Nat.*

- Commun.* **7**, 10591 (2016).
- 53 Ke, Y., Ong, L. L., Shih, W. M. & Yin, P. Three-Dimensional Structures Self-Assembled from DNA Bricks. *Science* **338**, 1177-1183 (2012).
- 54 Wei, B., Dai, M. & Yin, P. Complex shapes self-assembled from single-stranded DNA tiles. *Nature* **485**, 623-626 (2012).
- 55 Cui, Y. *et al.* Versatile DNA Origami Nanostructures in Simplified and Modular Designing Framework. *ACS Nano* **11**, 8199-8206 (2017).
- 56 Shih, W. M., Quispe, J. D. & Joyce, G. F. A 1.7-kilobase single-stranded DNA that folds into a nanoscale octahedron. *Nature* **427**, 618-621 (2004).
- 57 Liedl, T., Hogberg, B., Tytell, J., Ingber, D. E. & Shih, W. M. Self-assembly of three-dimensional prestressed tensegrity structures from DNA. *Nat. Nanotechnol.* **5**, 520-524 (2010).
- 58 Marko, J. F. & Siggia, E. D. Stretching DNA. *Macromolecules* **28**, 8759-8770 (1995).
- 59 Rubinstein, M. & Colby, R. H. *Polymer Physics*. (Oxford University Press, 2003).
- 60 Jorgensen, W. L., Chandrasekhar, J., Madura, J. D., Impey, R. W. & Klein, M. L. Comparison of simple potential functions for simulating liquid water. *J. Chem. Phys.* **79**, 926-935 (1983).
- 61 Phillips, J. C. *et al.* Scalable molecular dynamics with NAMD. *J. Comput. Chem.* **26**, 1781-1802 (2005).
- 62 Hart, K. *et al.* Optimization of the CHARMM Additive Force Field for DNA: Improved Treatment of the BI/BII Conformational Equilibrium. *J. Chem. Theory Comput.* **8**, 348-362 (2012).
- 63 Essmann, U. *et al.* A smooth particle mesh Ewald method. *J. Chem. Phys.*

- 103**, 8577-8593 (1995).
- 64 Feller, S. E., Zhang, Y., Pastor, R. W. & Brooks, B. R. Constant pressure molecular dynamics simulation: The Langevin piston method. *J. Chem. Phys.* **103**, 4613-4621 (1995).
- 65 Brooks, B. R., Janežič, D. & Karplus, M. Harmonic analysis of large systems. I. Methodology. *J. Comput. Chem.* **16**, 1522-1542 (1995).
- 66 Thomson, W. *Theory of vibration with applications*. (CRC Press, 1996).
- 67 Zhou, L., Marras, A. E., Su, H.-J. & Castro, C. E. Direct Design of an Energy Landscape with Bistable DNA Origami Mechanisms. *Nano Lett.* **15**, 1815-1821 (2015).
- 68 Ke, Y. *et al.* Multilayer DNA Origami Packed on a Square Lattice. *J. Am. Chem. Soc.* **131**, 15903-15908 (2009).
- 69 Dunn, K. E. *et al.* Guiding the folding pathway of DNA origami. *Nature* **525**, 82-86 (2015).
- 70 Lauback, S. *et al.* Real-time magnetic actuation of DNA nanodevices via modular integration with stiff micro-levers. *Nat. Commun.* **9**, 1446 (2018).
- 71 Sun, W. *et al.* Casting inorganic structures with DNA molds. *Science* **346**, 1258361 (2014).
- 72 Agarwal, N. P., Matthies, M., Joffroy, B. & Schmidt, T. L. Structural Transformation of Wireframe DNA Origami via DNA Polymerase Assisted Gap-Filling. *ACS Nano* **12**, 2546-2553 (2018).
- 73 Gerling, T., Kube, M., Kick, B. & Dietz, H. Sequence-programmable covalent bonding of designed DNA assemblies. *Sci. Adv.* **4**, eaau1157 (2018).
- 74 Lee, J. Y. *et al.* Investigating the sequence-dependent mechanical properties of DNA nicks for applications in twisted DNA nanostructure design. *Nucleic*

- Acids Res.* **47**, 93-102 (2019).
- 75 Murphy, M. C., Rasnik, I., Cheng, W., Lohman, T. M. & Ha, T. Probing Single-Stranded DNA Conformational Flexibility Using Fluorescence Spectroscopy. *Biophys. J.* **86**, 2530-2537 (2004).
- 76 Pfitzner, E. *et al.* Rigid DNA Beams for High-Resolution Single-Molecule Mechanics. *Angew. Chem. Int. Ed.* **52**, 7766-7771 (2013).
- 77 Kauert, D. J., Kurth, T., Liedl, T. & Seidel, R. Direct Mechanical Measurements Reveal the Material Properties of Three-Dimensional DNA Origami. *Nano Lett.* **11**, 5558-5563 (2011).
- 78 Schiffels, D., Liedl, T. & Fygenson, D. K. Nanoscale Structure and Microscale Stiffness of DNA Nanotubes. *ACS Nano* **7**, 6700-6710 (2013).
- 79 Lamour, G., Kirkegaard, J. B., Li, H., Knowles, T. P. & Gsponer, J. Easyworm: an open-source software tool to determine the mechanical properties of worm-like chains. *Source Code Biol. Med.* **9**, 16 (2014).
- 80 Rivetti, C., Guthold, M. & Bustamante, C. Scanning Force Microscopy of DNA Deposited onto Mica: Equilibration versus Kinetic Trapping Studied by Statistical Polymer Chain Analysis. *J. Mol. Biol.* **264**, 919-932 (1996).
- 81 Martin, T. G. & Dietz, H. Magnesium-free self-assembly of multi-layer DNA objects. *Nat. Commun.* **3**, 1103 (2012).
- 82 Turek, V. A. *et al.* Thermo-Responsive Actuation of a DNA Origami Flexor. *Adv. Funct. Mater.* **28**, 1706410 (2018).
- 83 Wagenbauer, K. F., Wachauf, C. H. & Dietz, H. Quantifying quality in DNA self-assembly. *Nat. Commun.* **5**, 3691 (2014).
- 84 Sedeh, R. S., Bathe, M. & Bathe, K.-J. The subspace iteration method in protein normal mode analysis. *J. Comput. Chem.* **31**, 66-74 (2010).

- 85 Bathe, K.-J. & Ramaswamy, S. An accelerated subspace iteration method.
Comput. Meth. Appl. Mech. Eng. **23**, 313-331 (1980).
- 86 Lu, X. J. & Olson, W. K. 3DNA: a software package for the analysis,
rebuilding and visualization of three-dimensional nucleic acid structures.
Nucleic Acids Res. **31**, 5108-5121 (2003).

국 문 초 록

본 논문은 상향식 자가조립 기법 중 하나인 DNA 오리가미 기술을 통해 만들어진 나노구조체의 기계적 강성을 효율적으로 설계하는 방법을 연구한 것이다. DNA 오리가미 기술은 기존의 나노재료 및 제작기술로는 만들기 어려운 복잡하고 정밀한 3차원 형상을 가진 나노구조체를 제작할 수 있어 높은 관심을 받고 있다. 또한 DNA 염기서열들간의 수많은 조합을 통해 매우 다양한 구조를 설계할 수 있다는 특징이 있어, 이를 통한 다양한 형상설계 기법 및 설계 자동화 기술이 활발히 발전해 왔다. 그러나 높은 합성비용 및 설계 복잡도를 가진 DNA 오리가미 기술은 염기서열 변동을 최소화하는 효율적인 설계기법 및 신뢰도 높은 예측모델의 부재로 인해, 구조체의 형상이나 특정 부위의 물리적 강성을 효율적으로 조절하기 어려운 문제점이 존재한다. 이에 본 연구에서는 DNA 오리가미 구조체의 기계적 강성을 인접하는 영역과 독립된 상태에서 손쉽게 제어할 수 있는 모듈 기반의 강성설계기법을 도입하였다. 이를 통해, 기존의 방법으로는 구현하기 어려운 효율적인 형상설계 및 구조체의 형상을 그대로 유지하면서 기계적 강성만을 정밀하게 조절하는 설계기법을 개발하였다. 본 연구에서 제안된 설계기법은 스캐폴드를 사용하는 DNA 오리가미 구조에 범용적으로 적용될 수 있어, 향후 DNA 오리가미 구조체를 이용한 다양한 응용연구에 사용될 수 있는 기반기술을 확립하였다.

주요어 : DNA 오리가미, DNA 나노구조체, 모듈기반 설계, 강성 제어, 국소결손구조, 유한요소해석, 분자동역학 시뮬레이션

학 번 : 2014-30342